

NASA/CR-2002-211670



Small Engine Technology (SET)
Task 33 – Final Report
Airframe, Integration, and Community
Noise Study

Lys S. Lieber and Daniel Elkins

Honeywell Engines, Systems, and Services, Phoenix, Arizona

October 2002

The NASA STI Program Office . . . in Profile

Since its founding, NASA has been dedicated to the advancement of aeronautics and space science. The NASA Scientific and Technical Information (STI) Program Office plays a key part in helping NASA maintain this important role.

The NASA STI Program Office is operated by Langley Research Center, the lead center for NASA's scientific and technical information. The NASA STI Program Office provides access to the NASA STI Database, the largest collection of aeronautical and space science STI in the world. The Program Office is also NASA's institutional mechanism for disseminating the results of its research and development activities. These results are published by NASA in the NASA STI Report Series, which includes the following report types:

- **TECHNICAL PUBLICATION.** Reports of completed research or a major significant phase of research that present the results of NASA programs and include extensive data or theoretical analysis. Includes compilations of significant scientific and technical data and information deemed to be of continuing reference value. NASA counterpart of peer-reviewed formal professional papers, but having less stringent limitations on manuscript length and extent of graphic presentations.
- **TECHNICAL MEMORANDUM.** Scientific and technical findings that are preliminary or of specialized interest, e.g., quick release reports, working papers, and bibliographies that contain minimal annotation. Does not contain extensive analysis.
- **CONTRACTOR REPORT.** Scientific and technical findings by NASA-sponsored contractors and grantees.

- **CONFERENCE PUBLICATION.** Collected papers from scientific and technical conferences, symposia, seminars, or other meetings sponsored or co-sponsored by NASA.
- **SPECIAL PUBLICATION.** Scientific, technical, or historical information from NASA programs, projects, and missions, often concerned with subjects having substantial public interest.
- **TECHNICAL TRANSLATION.** English-language translations of foreign scientific and technical material pertinent to NASA's mission.

Specialized services that complement the STI Program Office's diverse offerings include creating custom thesauri, building customized databases, organizing and publishing research results ... even providing videos.

For more information about the NASA STI Program Office, see the following:

- Access the NASA STI Program Home Page at <http://www.sti.nasa.gov>
- E-mail your question via the Internet to help@sti.nasa.gov
- Fax your question to the NASA STI Help Desk at (301) 621-0134
- Phone the NASA STI Help Desk at (301) 621-0390
- Write to:
NASA STI Help Desk
NASA Center for AeroSpace Information
7121 Standard Drive
Hanover, MD 21076-1320

NASA/CR-2002-211670



Small Engine Technology (SET)
Task 33 – Final Report
Airframe, Integration, and Community
Noise Study

*Lys S. Lieber and Daniel Elkins
Honeywell Engines, Systems, and Services, Phoenix, Arizona*

National Aeronautics and
Space Administration

Langley Research Center
Hampton, Virginia 23681-2199

Prepared for Langley Research Center
under Contract NAS3-27483, Task 33

October 2002

Available from:

NASA Center for AeroSpace Information (CASI)
7121 Standard Drive
Hanover, MD 21076-1320
(301) 621-0390

National Technical Information Service (NTIS)
5285 Port Royal Road
Springfield, VA 22161-2171
(703) 605-6000

TABLE OF CONTENTS

	<u>Page</u>
1. INTRODUCTION	1
1.1 Objectives	1
1.2 Description of Work	1
1.2.1 Airframe Noise Reduction Technology Study	1
1.2.2 Jet Shear Layer Refraction and Attenuation Study	2
1.2.3 Engine Source Noise Changes With Altitude Study	2
1.2.4 Lateral Attenuation Experiments	2
2. AIRFRAME NOISE REDUCTION TECHNOLOGY STUDY	2
2.1 Airframe Noise Reduction Technology Evaluation	2
2.1.1 Boeing Airframe Noise Program Activity	2
2.1.2 Airframe Noise Evaluations	3
2.1.3 Special Considerations for Business Jets	3
2.1.4 Current Status of Airframe Noise – Airframe Noise for the 1992 Baseline Technology Business Jet	4
2.1.5 Evaluation of Effectiveness of AST Noise Reduction Technologies for Airframe Noise, Using Boeing Code	12
2.1.6 Comparison With Goals	14
2.1.7 1/3-Octave SPL Time Histories of Airframe Noise	15
2.2 Array Processing of Distributed Source Noise	15
2.2.1 Introduction	15
2.2.2 Summary of the Array Processing Methodology	19
2.2.3 Summary of Results	21
2.2.4 List of Symbols	35
3. JET SHEAR LAYER REFRACTION AND ATTENUATION STUDY	36
3.1 Introduction and Review of Correction Procedures	36
3.1.1 Static-to-Flight Correction Procedures	36
3.1.2 Flyover Noise Prediction Process	37
3.1.3 Traditional Static-to-Flight Corrections	39
3.1.4 Shear Layer Corrections	40
3.2 Static-to-Flight Jet Shear Layer Correction Procedure for Internally Generated Engine Exhaust Noise	41
3.2.1 Overview	41
3.2.2 Problem Geometry	42
3.2.3 Static-to-Flight Angle Correction	43
3.2.4 Static-to-Flight Amplitude Correction	45
3.2.5 Angle Relationships	46
3.2.6 Implementation of the Corrections	49
3.2.7 Summary of the Static-to-Flight Correction Process	53
3.2.8 Computer Program	54

TABLE OF CONTENTS (Cont)

	<u>Page</u>
3.2.9 Sample Application of the Procedure	55
3.2.10 Limitations of the Method	55
3.3 Implementation in the NASA Aircraft Noise Prediction Program (ANOPP)	56
3.4 List of Symbols	56
4. ENGINE SOURCE NOISE CHANGES WITH ALTITUDE STUDY	57
4.1 Modeling Approach	57
4.2 Differences Between INM Versions 5.2a and 6.0.	58
4.3 Analysis Results	58
5. LATERAL ATTENUATION EXPERIMENTS	62
5.1 Introduction	62
5.2 Honeywell Participation	64
5.3 Data Analysis	66
6. REFERENCES	73

APPENDIXES

I	1/3-Octave Band SPL Time Histories of Estimated Airframe Noise (3 pages)
II	ANOPP Theoretical Manual Chapter for the Shear Layer Correction Module (14 pages)
III	ANOPP User Manual Chapter for the Shear Layer Correction Module (3 pages)
IV	INM Case Summary of 1992 Baseline Results (4 pages)
V	INM Case Summary for New Noise/Altitude Results (4 pages)

LIST OF FIGURES

	<u>Page</u>
Figure 1. Comparison of Airframe Noise Sources for 1992 Baseline Technology Business Jet.	5
Figure 2. Wing and Landing Gear Contributions to Total Airframe Noise for Baseline Business Jet and Boeing 737 at Approach.	6
Figure 3. Flap and Slat Contributions to Wing Noise for Baseline Business Jet and Boeing 737 at Approach.	7
Figure 4. Main and Nose Landing Gear Contributions to the Total Landing Gear Noise for the Baseline Business Jet at Approach.	8
Figure 5. Landing Gear Component Contributions to the Total Landing Gear Noise for the Baseline Business Jet at Approach.	9
Figure 6. Landing Gear Component Contributions to the Total Landing Gear Noise for the Baseline Business Jet and Boeing 737 at Approach.	11
Figure 7. Spectra Plot of Landing Gear Noise Sources at 90 Degrees for the Baseline Business Jet and the Boeing 737 at Approach.	12
Figure 8. Impact of Noise Reduction Technologies for Baseline Business Jet at Approach.	14
Figure 9. Schematic of a Leading Edge Slat and Wing Main Element Leading Edge.	16
Figure 10. Pressure Side (Flyover) View of Distributed Slat Noise With Local Discontinuities at the Side Plates.	19
Figure 11. Pressure-Squared Values as a Function of Spanwise Position.	20
Figure 12. Breakdown of Slat Noise Contributions for $M=0.17$, $\delta_s = 20^\circ$, $\delta_w = 26^\circ$, $\Psi = 0^\circ$, and $\Phi = 107^\circ$.	22
Figure 13. Schematic Diagram of the Slat/Wing Model and Elevation Angle Position (Side View).	22
Figure 14. Effect of the Main Element Angle-of-Attack on the Leading Edge Slat Noise.	27
Figure 15. Effect of Slat Element Angle-of-Attack for a Main Element Angle-of-Attack of 26 Degrees.	27
Figure 16. Effect of Slat Element Angle-of-Attack for a Main Element Angle-of-Attack of 32 Degrees.	28
Figure 17. Effect of Slat Gap/Overlap on the Sound Pressure Level of the Leading Edge Slat Noise.	28
Figure 18. Effect of the Teardrop Insert in the Slat Gap on the Sound Pressure Level of the Leading Edge Slat Noise.	29
Figure 19. Effect of Mach Number on the Teardrop Insert Leading Edge Slat Noise.	29
Figure 20. Effect of Directivity Angle on the Sound Pressure Level of the Baseline Leading Edge Slat Configuration.	30
Figure 21. Normalized Directivity (Using Adjusted Angles) of the Baseline Leading Edge Slat Configuration.	30
Figure 22. Directivity Characteristics of the Sound Pressure Level for the 6-Notch Gap/Overlap Conditions.	31
Figure 23. Normalized Directivity (Using Adjusted Angles) of the 6-Notch Gap/Overlap Conditions.	31
Figure 24. Effect of Trailing Edge Thickness on the Leading Edge Slat Noise.	32

LIST OF FIGURES (Cont)

	<u>Page</u>
Figure 25. Directivity Characteristics of the Sound Pressure Level for the Trailing Edge Thickness of 0.155”.	32
Figure 26. Normalized Directivity (Using Adjusted Angles) for the Trailing Edge Thickness of 0.155”.	33
Figure 27. Directivity Characteristics of the Sound Pressure Level for the Trailing Edge Thickness of 0.07”.	33
Figure 28. Normalized Directivity (Using Adjusted Angles) for the Trailing Edge Thickness of 0.07”.	34
Figure 29. Summary of the Noise Benefit for the Two Slat Noise Reduction Concepts.	34
Figure 30. A Description of The In-Flight Sound Pressure Levels Requires a Clear Distinction of the Coordinates System Used.	38
Figure 31. The Static-to-Flight Correction Procedure is Based Upon Cylindrical Model Geometry.	43
Figure 32. The Refraction Angle Correction is Derived by Considering Plane Wave Interaction With a Vortex Sheet.	44
Figure 33. A Relationship Between the Measurement Angle θ_m and Wave Normal Angle ϕ_{as} Can Be Derived From Geometrical Considerations.	47
Figure 34. The Ray Path Angle θ_c and the Wavenormal Angle ϕ Are Geometrically Related.	48
Figure 35. The Relationship Between θ_c and ϕ is Derived From Triangle Relationships.	48
Figure 36. Sample Refraction Results From the Simplified Model for $M_j = 0.5$, $M_a = 0.2$, and $c_j = c_a$.	51
Figure 37. Collapsing the Shear Layer Intersection Points Onto the Origin Allows for Simplifications to the Correction Procedure.	52
Figure 38. The Approximation Improves as the Sideline Distance From the Shear Layer Increases.	53
Figure 39. Small Changes Are Evident Flyover Noise Time History for the Cutback Takeoff Conditions.	55
Figure 40. EPNL Contour of Baseline 1992 Results With New Flight Profile.	59
Figure 41. EPNL Contour of New Noise/Altitude Results.	59
Figure 42. Approach Flight Segment.	60
Figure 43. Departure Flight Segment.	60
Figure 44. Noise Power Distance Curves From 1992 Baseline.	61
Figure 45. Noise Power Distance Curves for Noise/Altitude Study.	62
Figure 46. Diagram of Microphone Layout for the Lateral Attenuation Experiments at Wallops Island, VA.	63
Figure 47. The Honeywell Falcon 900EX, Waiting for the Winds to Calm and the Ceiling to Rise.	64
Figure 48. The Honeywell Falcon 2000 Arrived to an Almost Perfect Sky and No Winds on the Next Day.	65
Figure 49. The Falcon 2000 Flying Through the Microphone Cranes at Wallops Island.	65

LIST OF FIGURES (Cont)

	<u>Page</u>
Figure 50. The Measured and Projected Tone-Corrected Perceived Noise Level Time Histories Agree Well for the Falcon 2000 at the Takeoff Power Condition (82% N1) at Overhead.	66
Figure 51. The Comparison of the Measured and Projected Spectra Before Overhead (x=-252.0 ft) Agree Well for the Low Frequency Jet Noise and the Blade Passage Tone at Take-off Power (82% N1).	67
Figure 52. The Comparison of the Measured and Projected Spectra Near Overhead (x=-92.6 ft) Agree Well for the Low Frequency Jet Noise and the Blade Passage Tone at Take-off Power (82% N1).	67
Figure 53. The Comparison of the Measured and Projected Spectra Past Overhead (x=226.1 ft) Agree Well for the Low Frequency Jet Noise and the Blade Passage Tone at Take-off Power (82% N1).	68
Figure 54. The Measured and Projected Tone-Corrected Perceived Noise Level Time Histories Agree Well for the Falcon 2000 at the High Power Approach Condition (60% N1).	68
Figure 55. The Comparison of the Measured and Projected Spectra Before Overhead (x=-189.2 ft) Agree Well at High-Power Approach (60% N1).	69
Figure 56. The Comparison of the Measured and Projected Spectra Near Overhead (x=-21.1 ft) Agree Well at High-Power Approach (60% N1).	69
Figure 57. The Comparison of the Measured and Projected Spectra Past Overhead (x=315.0 ft) Agree Well at High-Power Approach (60% N1).	70
Figure 58. The Measured and Projected Tone-Corrected Perceived Noise Level Time Histories Agree Well for the Falcon 2000 at the Low Power Approach Condition (48% N1).	70
Figure 59. The Comparison of the Measured and Projected Spectra Before Overhead (x=-108.8 ft) at the Low-Power Approach (48% N1).	71
Figure 60. The Comparison of the Measured and Projected Spectra Near Overhead (x=+51.9 ft) at the Low-Power Approach (48% N1).	71
Figure 61. The Comparison of the Measured and Projected Spectra Past Overhead (x=+212.6 ft) at the Low-Power Approach (48% N1).	72

LIST OF TABLES

	<u>Page</u>
Table 1. Noise Reductions Required to Meet Pillar Goals for Business Jet at Approach.	15
Table 2. Processed Baseline Configurations.	23
Table 3. Processed Trailing Edge Thickness Configurations.	24
Table 4. Processed Teardrop Insert Configurations.	25
Table 5. The Following Inputs Are Supplied to Subroutine REFRACT.	54
Table 6. The Following Outputs Are Returned by Subroutine REFRACT.	54
Table 7. Differences in Effective Perceived Noise Levels Between Predictions Made With and Without Shear Layer Corrections Are Relatively Modest.	55
Table 8. Summary of Altitude Effects on EPNL Contours.	58

**SMALL ENGINE TECHNOLOGY (SET) – TASK 33
AIRFRAME, INTEGRATION, AND COMMUNITY NOISE STUDIES
FINAL REPORT**

1.INTRODUCTION

1.1 Objectives

Task Order 33 had four primary objectives as follows:

- (1) Identify and prioritize the airframe noise reduction technologies needed to accomplish the NASA Pillar goals for business and regional aircraft.
- (2) Develop a model to estimate the effect of jet shear layer refraction and attenuation of internally generated source noise of a turbofan engine on the aircraft system noise.
- (3) Determine the effect on community noise of source noise changes of a generic turbofan engine operating from sea level to 15,000 feet.
- (4) Support lateral attenuation experiments conducted by NASA Langley at Wallops Island, VA, by coordinating opportunities for Contractor Aircraft to participate as a noise source during the noise measurements.

1.2 Description of Work

1.2.1 Airframe Noise Reduction Technology Study

1.2.1.1 Airframe Noise Reduction Technology Evaluation

Noise data and noise prediction tools, including airframe noise codes, from the NASA Advanced Subsonic Technology (AST) program were applied to assess the current status of noise reduction technologies relative to the NASA pillar goals for regional and small business jet aircraft. In addition, the noise prediction tools were applied to evaluate the effectiveness of airframe-related noise reduction concepts developed in the AST program on reducing the aircraft system noise. The AST noise data and acoustic prediction tools used in this study were furnished by NASA.

1.2.1.2 Array Processing of Distributed Source Noise

Airframe noise mechanisms associated with a wing-slat model tested in the NASA Langley Quiet Flow Facility under the Advanced Subsonic Technology Program were assessed and documented. Documentation addressed aeroacoustic scaling, directivity, noise reduction, and array-processing techniques associated with this specific wing-slat model. NASA Langley researchers provided the data to be assessed in this study.

1.2.2 Jet Shear Layer Refraction and Attenuation Study

A jet shear layer refraction and attenuation model was identified that will calculate source noise changes due to propagation of sound through a shear layer produced by the jet/aircraft flow field interaction. An algorithm based on the approved model was developed and verified. This algorithm was designed for compatibility with NASA's Aircraft Noise Prediction Program (ANOPP). Once the algorithm was implemented in Fortran code, it was used to quantify the effect of the jet shear layer on the far field noise levels for a typical regional aircraft installation.

1.2.3 Engine Source Noise Changes With Altitude Study

Engine performance parameters required for prediction of the engine noise from sea level to 15,000 feet altitude were obtained for the 1992-technology baseline business jet. Using this information, altitude-related changes in engine source noise were predicted for a typical takeoff and landing profile, using the methods in ANOPP. The resulting new source noise characteristics with altitude were input into the Federal Aviation Administration (FAA) Integrated Noise Model (INM) program. INM was used to compute changes in the Sound Exposure Level contours due to the new source noise characteristics.

1.2.4 Lateral Attenuation Experiments

Two Contractor aircraft were provided to support the flight experiment conducted by NASA Langley at Wallops Island, VA. The aircraft have aft-mounted engines with a takeoff bypass ratio of at least 4.0. In addition, the Contractor supported test data evaluation and correlation with the primary engine parameters. This support included providing on-board engine performance data, and post-test comparison with static engine data for at least 3 key operating points.

2. AIRFRAME NOISE REDUCTION TECHNOLOGY STUDY

2.1 Airframe Noise Reduction Technology Evaluation

2.1.1 Boeing Airframe Noise Program Activity

Boeing provided the airframe noise prediction program to Honeywell per NASA's request. The software was successfully compiled and executed for the supplied test case. However, examination of the software revealed that the directivity module was not included. The complete program was then requested from Boeing. A modified version of the airframe noise program, AFMTOT2, was received from NASA Langley on 30 November 2000. The complete program from Boeing was received on 6 December 2000. It was this latter version of the program that was used for the study effort in this task.

Validation of the complete version of the Boeing airframe noise prediction program was completed. However, a number of inconsistencies between versions of the program were identified and corrected. In addition, the capability to compute noise spectra at a user-specified constant radius, including atmospheric effects, has been included in the program, in addition to the capability to run at any fly-over distance, or flight angle. The ability to independently include or exclude specific flap and slat components was added to the program, in order to accommodate smaller business jet aircraft, which typically do not have two sets of flaps or slats.

To represent the effects of the AST noise reduction technologies on the overall airframe noise, the Boeing airframe noise prediction program was modified to allow the adjustment of the various airframe-component noise sources. These adjustments were included as “delta” values added to the component SPL values at 90 degrees. The user specifies the delta values in the appropriate input file NAMELIST.

2.1.2 Airframe Noise Evaluations

For the purposes of this study, it was assumed that the airframe noise characteristics of business and regional aircraft were similar, due to similarities in size. Therefore, all studies were performed using the 1992 Baseline Technology Business Jet. Actual airframe dimensions were obtained from aircraft representative of the 1992 Baseline Business Jet in airframe size and configuration.

2.1.3 Special Considerations for Business Jets

Because the Boeing airframe noise prediction program was developed using component noise models based on larger aircraft, these models were not completely representative of the components on smaller aircraft, such as business jets. For this reason, special considerations and assumptions were made when performing the airframe noise predictions for the business jet. Accuracy of the predictions cannot be established until appropriate calibrations are performed for smaller aircraft.

The business jet wing configuration differed from that modeled in the Boeing noise prediction program. The Boeing wing model assumed a configuration consisting of four noise sources: Inboard Flaps, Outboard Flaps, Ailerons, and Slats. This was appropriate for the larger aircraft in the Baseline study (small twin, medium twin, and large quad).

However, the typical business jet has only one set of flaps, because of its smaller size relative to the other study aircraft. In addition, the aileron noise model was found to be inappropriate for the smaller aircraft. Further, the representative business jet does not have a slat cove or gap, when the slat is deployed, which is inconsistent with the slat noise model.

In the Boeing airframe noise prediction program, the “Aileron” model refers to a High-Speed Aileron (HSA) between the inboard and outboard flaps. Noise from the HSA represents combined effects of the adjacent inboard and outboard flap edge noise sources. The “Outboard Flap” model represents the noise generated by the outboard edge of the outboard flap. (The HSA model accounts for the inboard edge of the outboard flap.)

Boeing recommended that, for the Business Jet configuration, the “Aileron” model not be used, because the Business Jet does not have the Inboard Flap/HSA/Outboard Flap configuration. Instead, he recommended using the “Outboard Flap” model only. The outboard flap model would be more representative of the actual wing loading for the business jet, with a single flap set.

For business jets representative of the 1992 Baseline, slat configurations are simplified, compared to the larger airframes. Separated slat designs normally are not used. Therefore, the noise generated by the gap and cove of a separated flap is not present. The slat noise for such a configuration would be expected to be much lower than the slat model in the Boeing code would predict.

2.1.4 Current Status of Airframe Noise – Airframe Noise for the 1992 Baseline Technology Business Jet

To establish the current status of airframe noise, a prediction was performed for the airframe noise for the 1992 Baseline Technology Business Jet. The results were obtained by executing the Boeing airframe noise prediction program for a constant radius of 100 feet. The resulting airframe SPL values were then supplied to the Honeywell flyover noise prediction program, GASP. GASP was run at Approach, to obtain the EPNL predictions for airframe noise. Only the Approach condition was studied, because airframe noise is not a significant contributor to overall noise at the Cutback and Sideline takeoff conditions.

The following assumptions were made for the Baseline analysis:

- (a) No aileron (HSA) contribution.
- (b) Slat noise was reduced from the Boeing slat model noise level by -2.9 dB, due to the lack of a cove and gap (representative of $1/2$ of the predicted reduction due to elimination of the cove and gap in Boeing's studies).
- (c) No inboard flaps.
- (d) Business jet flap noise was represented by the Outboard Flap model.
- (e) Flap circulation and cross-flow velocity were based on an existing Honeywell FLUENT analysis of the business jet wing, with undeployed flaps. (The resulting influence on noise predictions was not great, and a full panel analysis with the deployed flap configuration was beyond the scope of the task.).
- (f) The Landing Gear Dirtiness Factor, for the High-Frequency gear component was set to $XI = 2.97$ for all analyses, as recommended by Boeing.
- (g) Some of the input for the business aircraft was obtained by scaling values from the Boeing 737 test case provided with the program, for those aerodynamic parameters which were not readily available (lift coefficients for the slats and flaps).

The Boeing airframe noise prediction program is currently unable to process both main and nose landing gear in the same case. Therefore, to include the effect of the nose gear, a second case was considered, in which only the nose gear was analyzed. This nose gear result was then summed logarithmically with the rest of the noise sources to obtain the total airframe noise.

The total airframe noise at Approach for the 1992 Baseline Technology Business Jet was predicted by the Boeing program, with GASP fly-over analysis, to be 86.5 dB EPNL (including the nose gear). Coincidentally, this level matches the level used in the original 1992 Baseline Technology study. The original airframe noise value came from an ANOPP prediction, using the Fink airframe noise model.

To obtain the individual component contributions to the overall EPNL predicted by GASP, the Boeing program was run multiple times, shutting off all but one component in each analysis. This permitted airframe SPL values to be generated for each airframe component. Running GASP with each set of SPLs produced EPNL values for each individual airframe component. As seen in Figure 1, the flaps have a significantly higher contribution than the other sources. The main gear is second, followed by the slats, and then the nose gear.

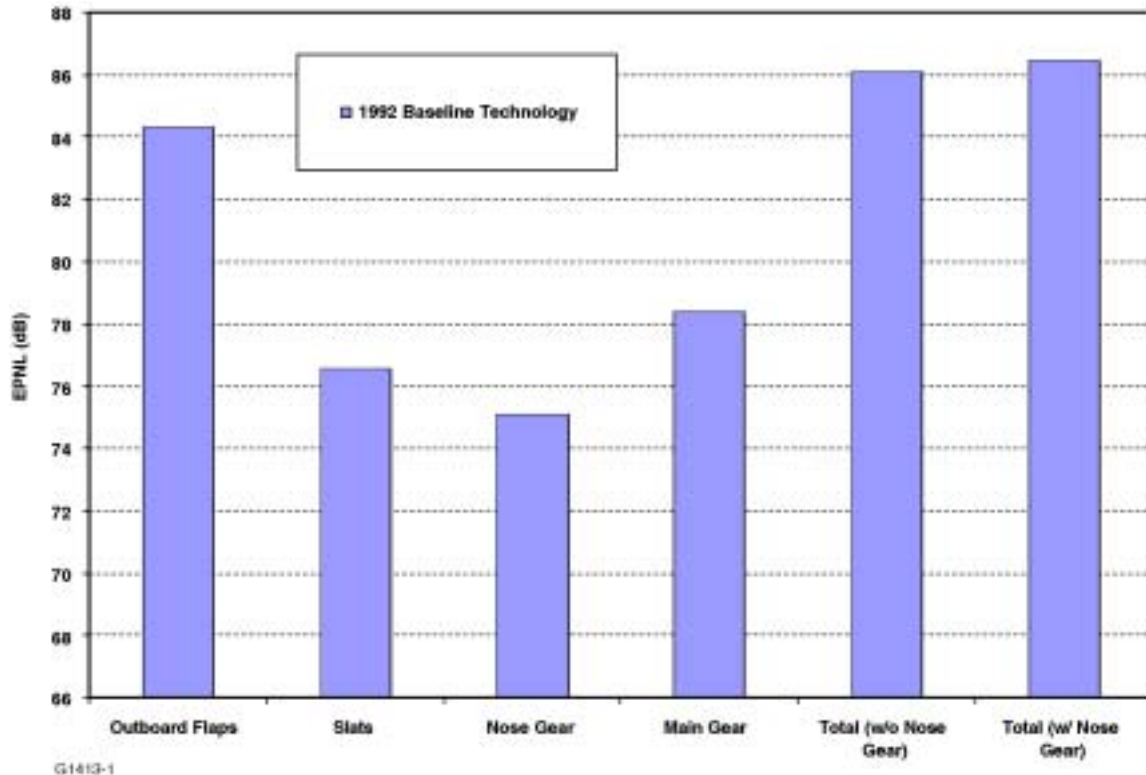


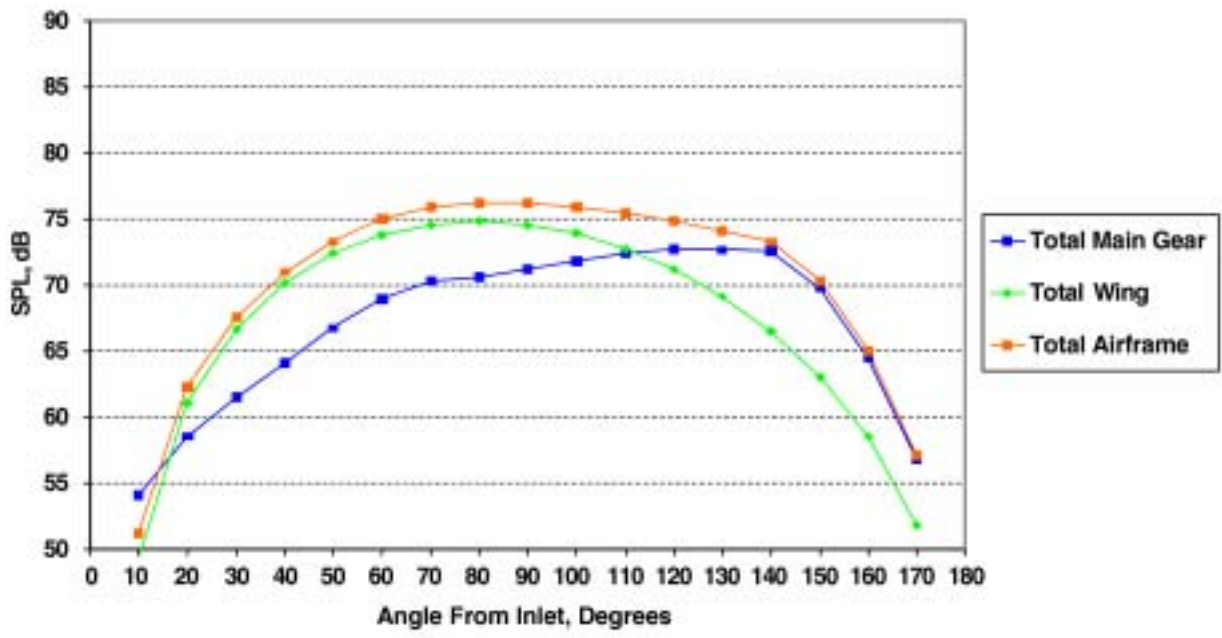
Figure 1. Comparison of Airframe Noise Sources for 1992 Baseline Technology Business Jet.

To better understand the character of the noise sources for the business jet relative to the larger airframes, each component was examined in more detail and compared to the Boeing 737 (B737) characteristics. Source directivity plots of SPL were generated for all components of airframe noise by executing the Boeing program at the Approach condition (394 feet altitude over the microphone, 3-degree glide slope).

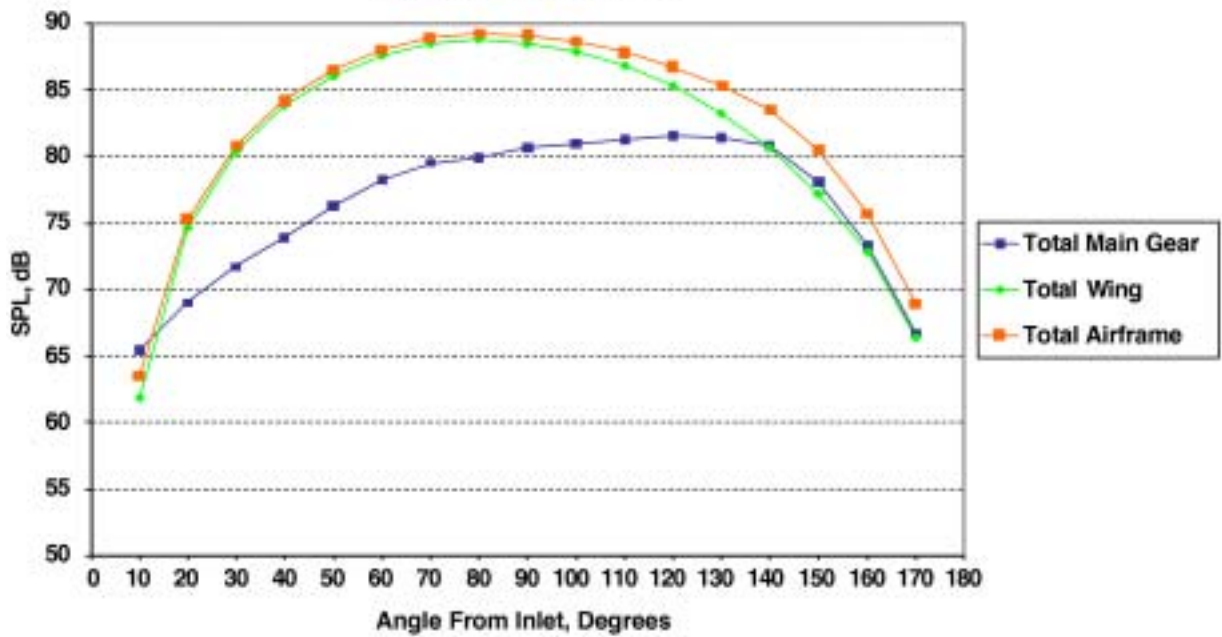
The summary plot of wing and landing gear components (Figure 2) shows that the main landing gear is a more significant contributor to overall airframe noise for the Business Jet than for the B737, particularly at the aft angles. This tends to sustain a higher overall noise level at the aft angles for the Business Jet.

In the wing noise plot (Figure 3), the flap noise is considerably higher than the slat noise for the business jet. However, for the B737, the flap and slat noise are more similar in level. To represent the “cleaner” business jet slat, the slat noise was reduced by 1/2 of the benefit projected by Boeing for the near-term cove fill and gap reduction.

The landing gear plot in Figure 4 shows that the nose gear contribution is only about 3 dB below the main gear for the Business Jet. In contrast, the nose gear noise levels for the larger aircraft are approximately 7-12 dB below those of the main gear. The difference becomes greater as the aircraft size increases, indicating the relative increase in main gear size/complexity relative to the nose gear. Therefore, for a smaller aircraft, the contribution of the nose gear is more significant. The nose gear was modeled assuming the strut diameter, hydraulic line diameter, etc. remained the same as the main gear. Tire diameter was reduced to reflect the smaller size of the nose gear tires.

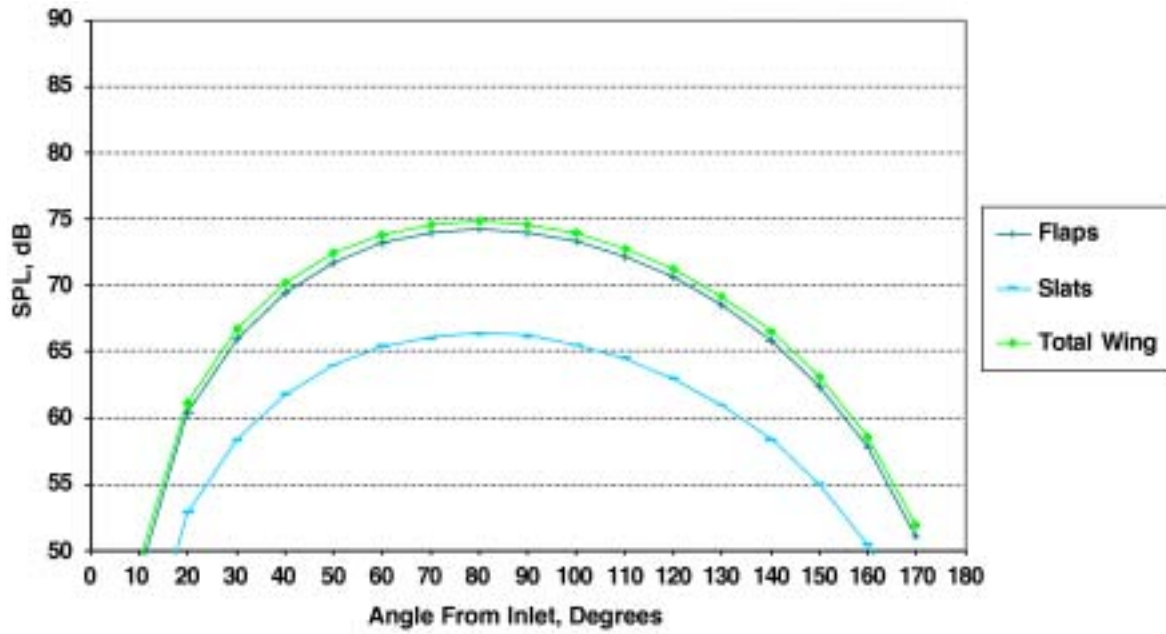


(a) Baseline Business Jet

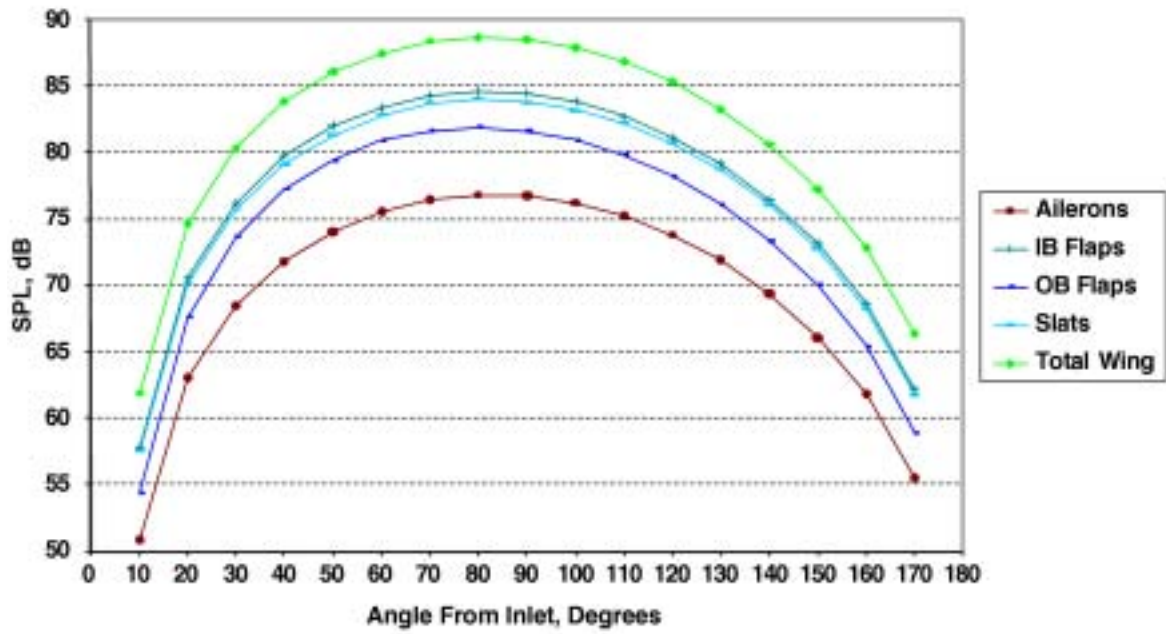


(b) Boeing 737

Figure 2. Wing and Landing Gear Contributions to Total Airframe Noise for Baseline Business Jet and Boeing 737 at Approach.



(a) Baseline Business Jet



(b) Boeing 737

G1413-3

Figure 3. Flap and Slat Contributions to Wing Noise for Baseline Business Jet and Boeing 737 at Approach.

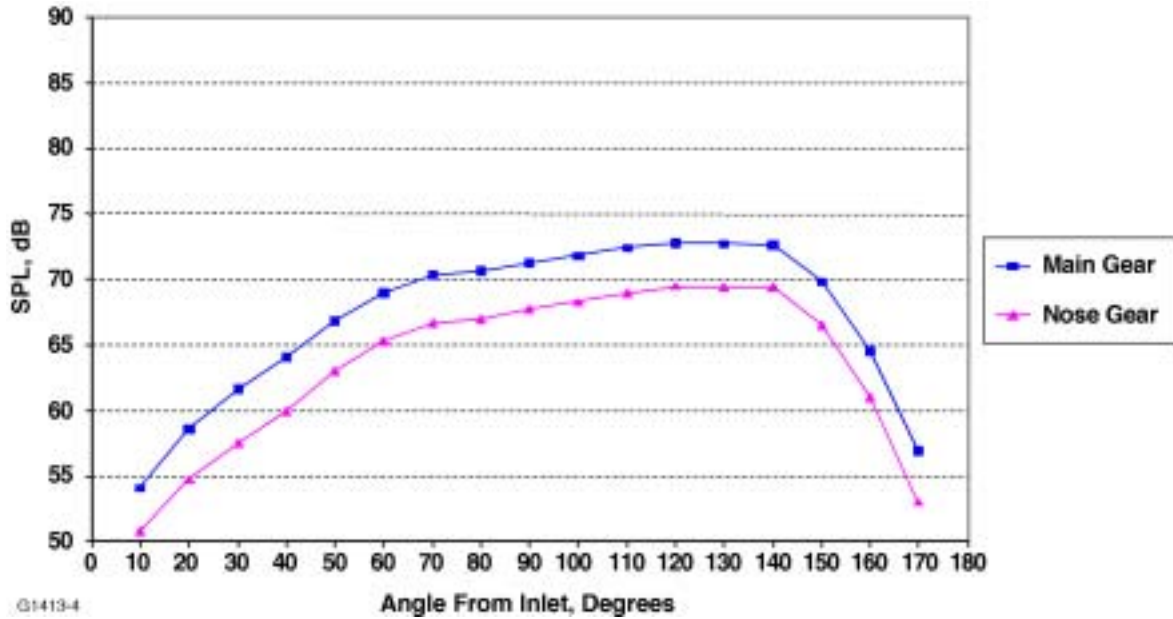
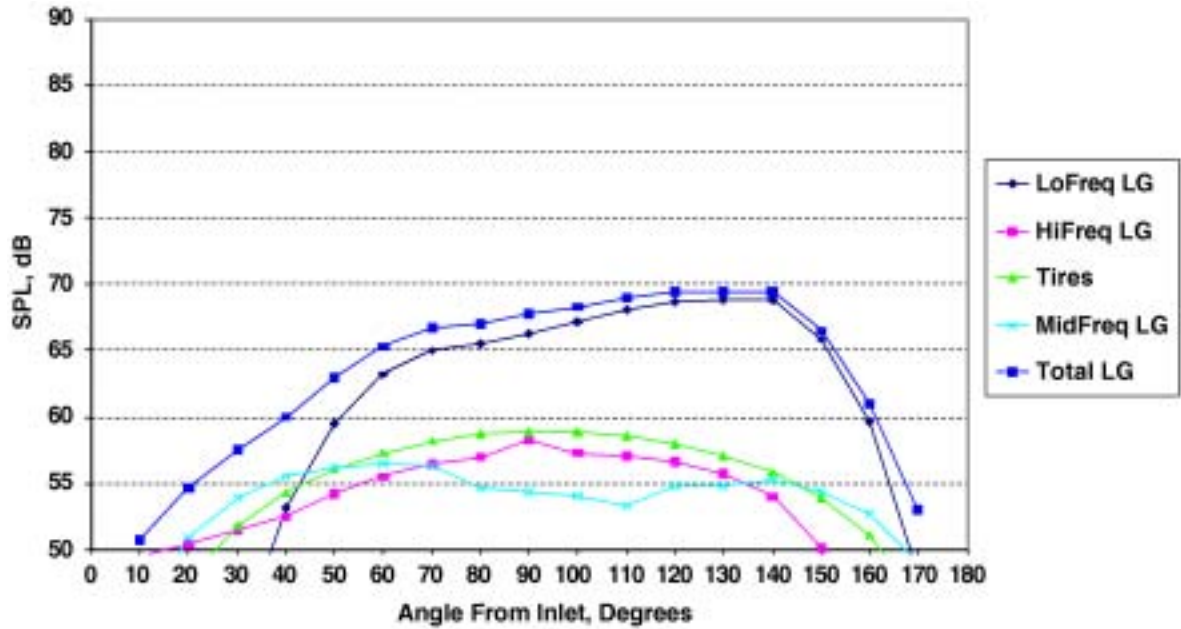
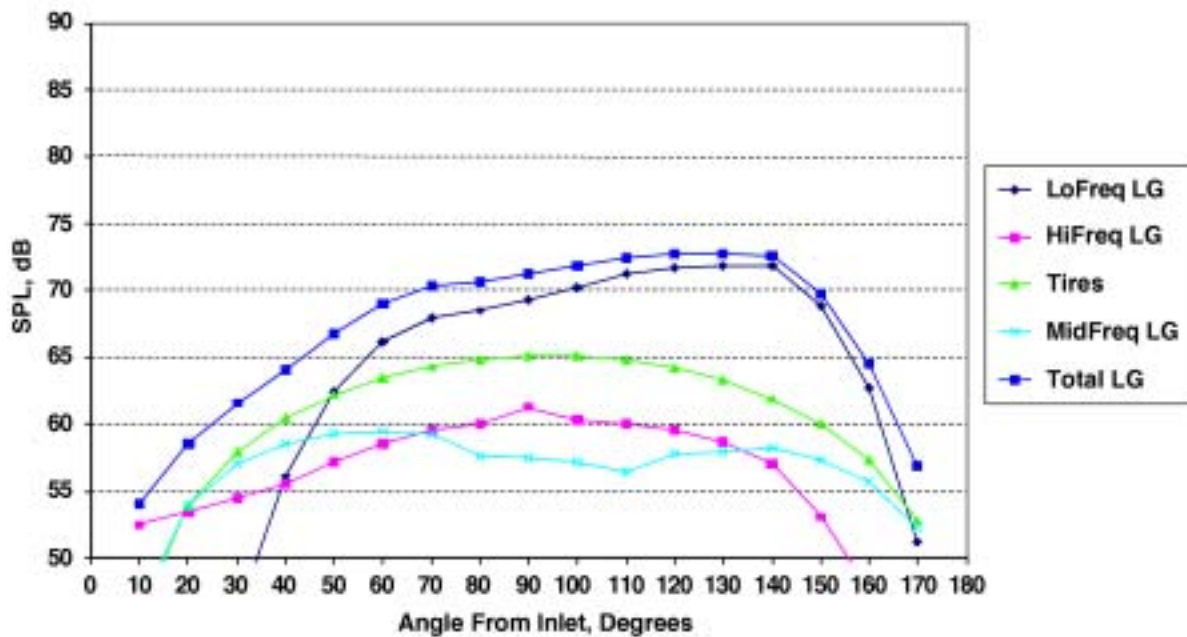


Figure 4. Main and Nose Landing Gear Contributions to the Total Landing Gear Noise for the Baseline Business Jet at Approach.

As shown in Figure 5, for both the nose and main gear of the business jet, the low-frequency noise is the primary contributor, with the mid- and high-frequency noise having minimal effect. However, tire noise is a much larger contributor, relative to the mid- and high-frequency sources, for the main gear than for the nose gear. This may be explained by the larger tire diameter for the main gear.



(a) Nose Gear



(b) Main Gear

Figure 5. Landing Gear Component Contributions to the Total Landing Gear Noise for the Baseline Business Jet at Approach.

As shown in Figure 6, for the main gear, the character of the low-frequency noise is similar for the bizjet and the B737. Also, the character and level of tire noise, relative to the low-frequency noise, is similar for the bizjet and B737. However, the mid- and high frequency sources are somewhat more significant contributors to overall landing gear noise for the B737.

High-frequency noise for the B737 is almost on a par with the tire noise, but is about 5 dB below the tire noise for the bizjet. Differences in the relative diameter of hydraulic lines versus landing gear struts for the two aircraft types contribute to this behavior. The high frequency noise sources are affected by the smaller diameter components, such as hydraulic lines. For the B737, the hydraulic line diameters relative to the landing gear strut diameters are approximately 0.17; in contrast, the ratio for the bizjet is 0.12. This would account for the approximately 3 dB larger difference between the low- and high-frequency SPLs for the bizjet than for the B737.

To further understand the character of the various landing gear sources, a spectra plot at 90 degrees was produced for all landing gear noise sources, for both the business jet and B737 (refer to Figure 7). As seen from the plots, the peak frequencies of the sources are shifted higher for the bizjet, compared to the B737. This shift is most significant for the mid- and high frequency sources. The shift is explained by the smaller diameter of the noise-generating components (strut and hydraulic line diameters) for the bizjet, compared to the B737.

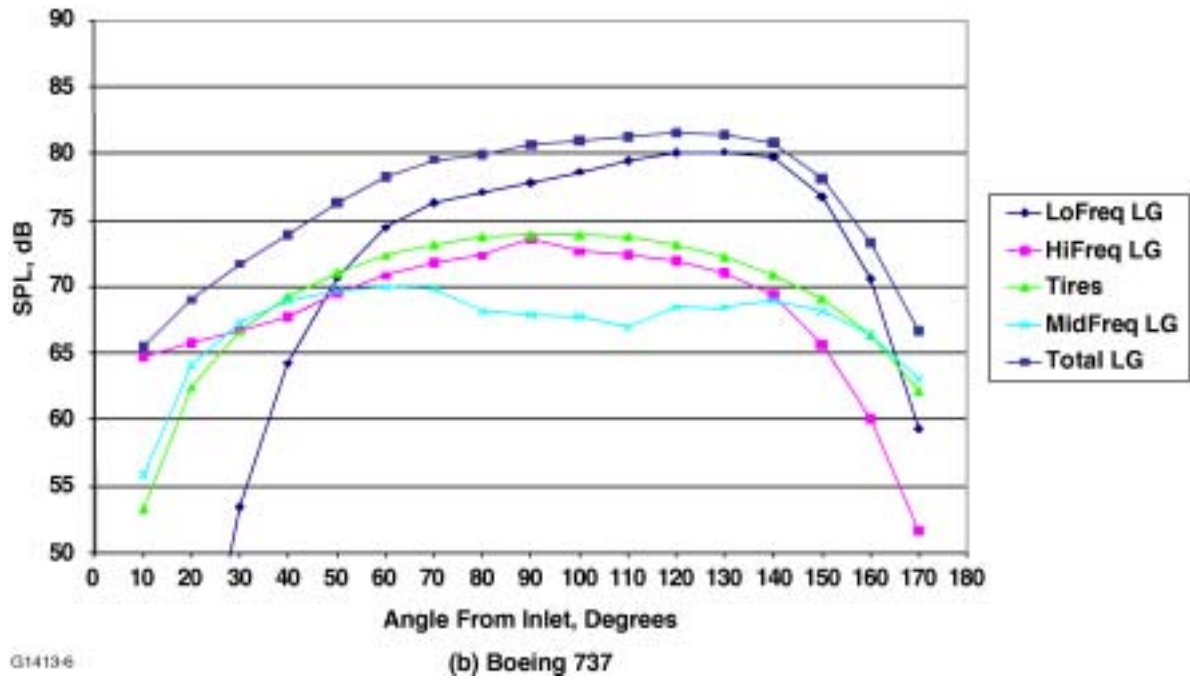
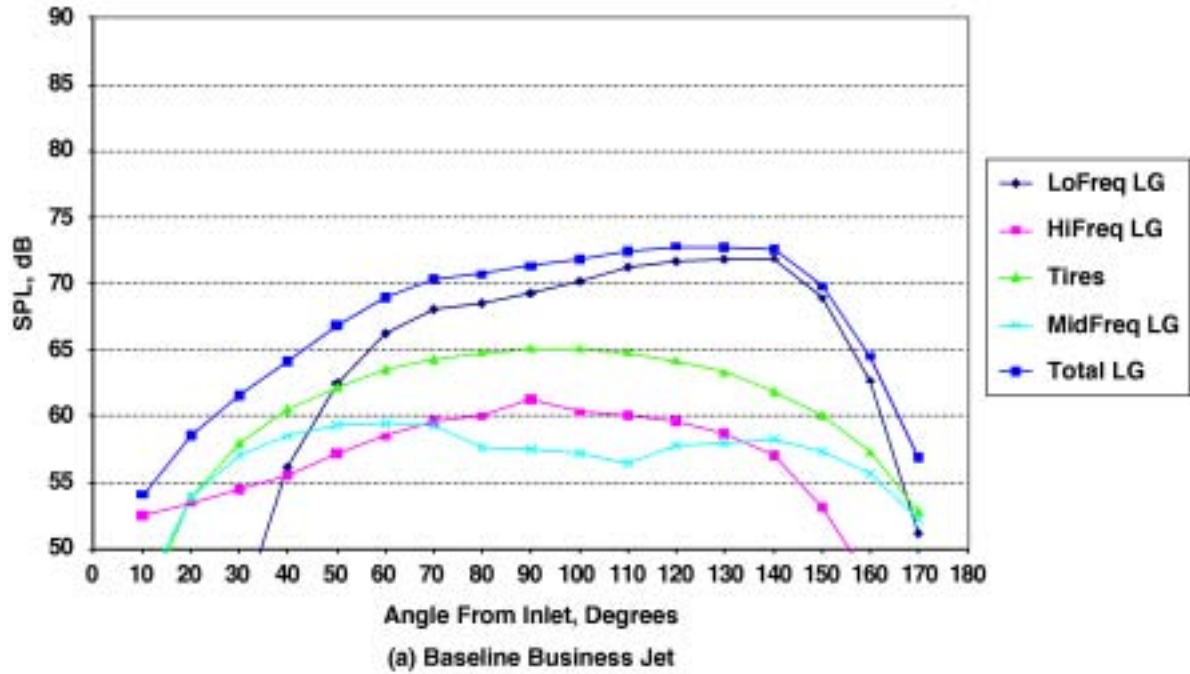


Figure 6. Landing Gear Component Contributions to the Total Landing Gear Noise for the Baseline Business Jet and Boeing 737 at Approach.

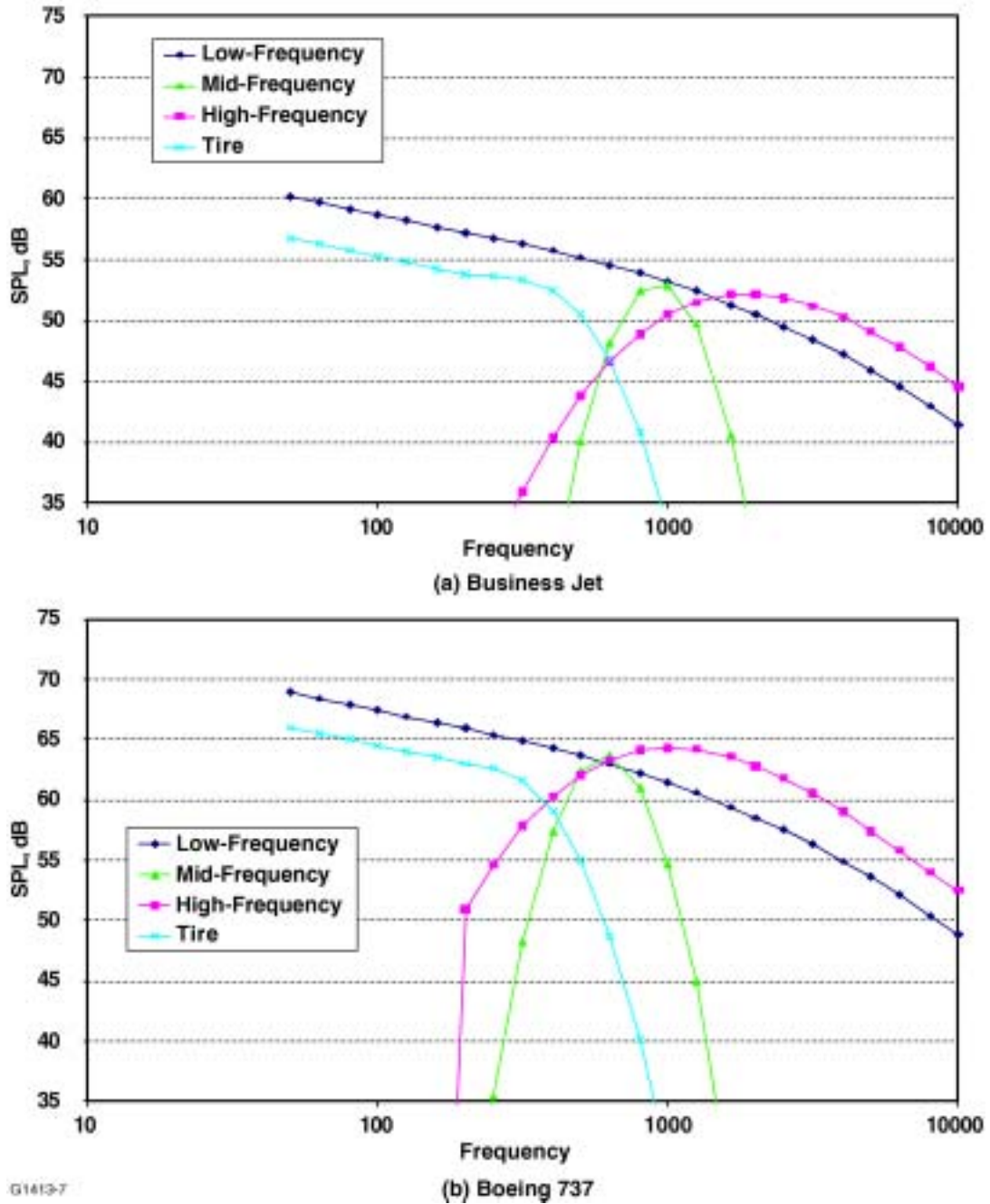


Figure 7. Spectra Plot of Landing Gear Noise Sources at 90 Degrees for the Baseline Business Jet and the Boeing 737 at Approach.

2.1.5 Evaluation of Effectiveness of AST Noise Reduction Technologies for Airframe Noise, Using Boeing Code

Noise reduction concepts were proposed during the AST Program to address the flap, slat, and landing gear sources. Boeing studied the effectiveness of a subset of the concepts. The resulting noise reduction data from the Boeing study were applied to the 1992 Baseline Technology Business Jet, at Approach conditions.

Slat Concepts – The only slat noise reduction technology considered by Boeing consisted of a cove fill and gap reduction. This was projected to yield an 11.4 dB reduction in slat noise over the long-term, with a 5.8 dB reduction near-term. However, the business jet slat configuration did not have a cove gap. Therefore, the baseline slat noise level was reduced to reflect the absence of a slat gap. In addition, further reductions in slat noise were not expected to be as substantial.

Because the noise reduction technology techniques used for the near-term reductions were already employed in the simplified flap of the Baseline Business Jet, it was assumed that the slat noise was already reduced by 1/2 of the Boeing Near-Term reduction, due to the absence of the cove and gap. Further, it was assumed that no additional reduction would be achieved in the near-term, because the primary noise generators were not present. It was assumed that the long-term benefit would be 1/2 of the Boeing long-term benefit. Therefore, the AST noise reduction technologies for the business jet slat noise were modeled as:

- (a) Near-Term -2.9 dB (Same as Baseline)
- (b) Long-Term -5.7 dB

Landing Gear Concepts – Only high-and mid-frequency noise reductions were considered in the Boeing study. Such reductions could possibly be achieved by placing fairings over small components and moving lines and brackets out of the flowpath. However, the high- and mid-frequency noise sources do not contribute as much to overall gear noise for the business jet as they do for the B737. Therefore, not as much overall benefit would be expected. Applying the same levels of component reduction predicted by Boeing, the AST noise reduction technologies for the business jet landing gear were modeled as:

- (a) Near-Term -1.4 dB (High-Frequency)
- (b) Long-Term -3.0 dB (High- and Mid-Frequency)

The same levels of reduction were applied for the nose and main gear.

Flap Concepts – Fences of various thicknesses, microtabs, and porous flap tips were all examined in the Boeing study for near-term noise reduction. However, at most, these concepts yielded a 1.4 dB reduction in outboard flap noise (for fences with 2x flap thickness). Similar benefits were assumed for the bizjet. In addition, for the long-term case, no flap noise was assumed.

Based on the Boeing AST Noise Reduction Technology numbers, the following reductions were applied for the business jet, using the outboard flaps:

- (a) Near-Term -1.4 dB
- (b) Long-Term -20.0 dB (To model the “No Flap Effects” condition)

The flap models in the Boeing program were not considered accurate for the 0-degree deflection case (“No Flap Effects”). The flap models were based on configurations of 20, 30 and 40 degrees deflection, and would tend to underpredict the actual trailing edge noise for an undeflected flap. Therefore, this condition was modeled by reducing the flap noise level (-20 dB) to the point at which it was insignificant.

Combined Concepts – To determine the maximum overall benefit for the business jet, all noise reduction technologies were combined, for Near-Term and Long-Term evaluations. The effect of the noise reduction technologies is shown in the bar chart in Figure 8.

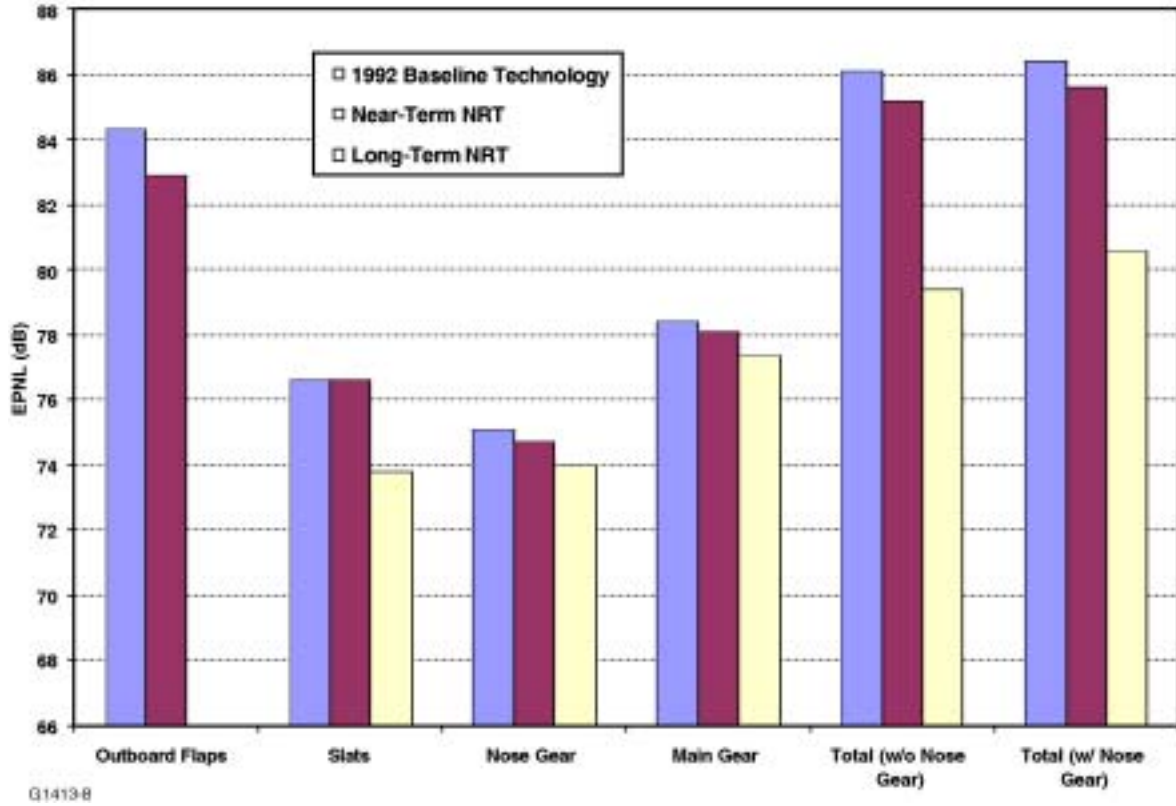


Figure 8. Impact of Noise Reduction Technologies for Baseline Business Jet at Approach.

As shown in Figure 8, in the near-term, the flaps were still the major contributor, and only slight reductions were seen in gear noise. Therefore, the overall airframe noise reduction was only 0.9 dB. In the long-term, the flaps did not contribute at all. The primary source was the main gear, with the slats and nose gear approximately equal. The overall airframe noise reduction was 5.9 dB.

Gear noise was not reduced substantially with noise reduction technologies, because the reductions were applied to the mid- and high-frequency sources, but the low-frequency sources clearly dominated. Therefore, not much benefit was seen.

2.1.6 Comparison With Goals

The Pillar Goals for airframe noise reduction may be represented as follows:

- (a) Near-Term -4 dB (QAT Goal – 1997-2007)
- (b) Long-Term -8 dB (QAT + Follow-on – 2002-2022)

The Near-Term AST noise reduction technology does not satisfy the goal of a 4 dB reduction in airframe noise. Similarly, the long-term noise reduction technology does not satisfy the goal of an 8 dB reduction in airframe noise.

Additional noise reduction technologies would be necessary to reduce airframe noise for business jets, and satisfy the Pillar Goals. As shown in Table 1, in the near-term, flap noise would have to be reduced 7.7 dB below the baseline (an additional 6.3 dB), and low-frequency noise would have to be addressed for the landing gear (-1.8 dB for main gear, -0.4 dB for nose gear, at all frequencies). In the long-term, in addition to eliminating flap noise, landing gear noise would have to be reduced by 5.2 dB (main) and 1.8 dB (nose) at all frequencies. Finally, a further slat noise reduction would be required, totaling 3.3 dB from the baseline.

Table 1. Noise Reductions Required to Meet Pillar Goals for Business Jet at Approach.

EPNL for Airframe Noise (1992 Baseline Business Jet)

(EPNL Computed from GASP, using Airframe Noise Predicted by Boeing Airframe Noise Prediction Program)

Noise Reduction Concept	Outboard Flaps	Slats	Nose Gear	Main Gear	Total	Delta from Baseline
Baseline:						
Baseline Total	84.3	76.6	75.1	78.4	86.2	
Combined NRTs:						
Near-Term Delta	-7.7	0.0	-0.4	-1.8		
Near-Term Total	76.6	76.6	74.7	76.6	82.2	-4.0
Long-Term Delta	-20.0	-3.3	-1.8	-5.2		
Long-Term Total	64.3	73.3	73.3	73.2	78.2	-8.0

2.1.7 1/3-Octave SPL Time Histories of Airframe Noise

A 1/3-Octave SPL Time History of estimated airframe noise for the 1992 Baseline Technology Business Jet was generated for delivery to NASA. The data were generated by first running the Boeing airframe noise prediction program at 100 foot radius for two cases:

- (a) Outboard flaps, slats, main gear
- (b) Nose gear

The GASP program was then run at Approach conditions, for each of the above cases, to generate 1/2-second interval flyover spectra files. The airframe noise spectra files from the above two cases were then combined, using a logarithmic sum technique, to include the nose gear noise in the final spectra file. The resulting spectra are tabulated in Appendix I.

2.2 Array Processing of Distributed Source Noise

2.2.1 Introduction

The leading edge slat of a multi-element wing is used to delay the onset of main element separation by alleviating the suction side pressure peak of the main element leading edge. Thus,

the leading edge slat serves the purpose of potentially improving the lift capability (CL_{max}) of the aircraft. A more detailed description of complex flow field between the slat and main element would involve the viscous interactions of the slat wake and the main element boundary layer. As with most aeroacoustic occurrences, acoustic improvements often correlate highly with aerodynamic performance degradation. It has been reported (Reed [1]) that slat noise reduction can be attained by reducing the gap distance between the slat trailing edge and the main element leading edge; however, less than optimal lift performance can be the consequence of a relatively small gap size (Thomas et al. [2]). Figure 9 illustrates the slat and main element and some key terminology pertaining to the geometrical configuration of these wing elements.

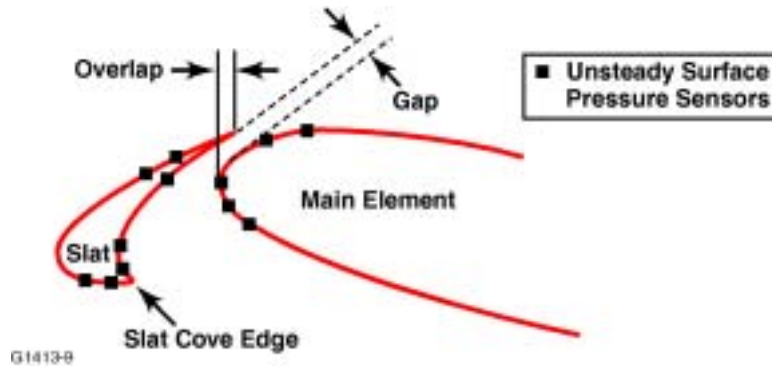


Figure 9. Schematic of a Leading Edge Slat and Wing Main Element Leading Edge.

It was observed in early airframe noise investigations that the addition of a loaded leading edge slat not only resulted in increased noise levels in the vicinity of the wing leading edge but also influenced the noise associated with the airframe flaps (Hayes et al. [3]). A significant increase in the outboard flap noise levels of a 4.7% scale DC-10 model was observed by Hayes et al. while the inboard flap levels were only nominally influenced by the presence of the loaded leading edge slat. This effect was postulated to be the result of the leading edge slats influence on the wing aerodynamic loading primarily on the outboard side although no clarification was provided. Through the use of flap-tip fences, Hayes et al. also demonstrated that the reduction of flap source noise accentuated the contributions of the leading edge slats to the overall noise of this aircraft model. This demonstration emphasized the fact that in order to achieve significant airframe noise reduction equal attention must be given to leading edge slat. In a series of NASA reports also utilizing a 4.7% scale DC-10 model, Guo et al. [4][5][6] further demonstrated the importance of the leading edge slat on airframe noise noting the dominant role of leading edge slat sources at the moderate to low flap deflection angles. This finding is germane to the newer airframes such as the 777 due to the usually lower flap settings relative to the DC-10. Utilization of a phased array of microphones, strategically located surface mounted pressure transducers, and free field noise measurements resulted in a number of significant findings by Guo et al. pertaining to slat noise. Most notably are the significant slat noise levels observed at the lower flap deflection settings and the distributed nature of the leading edge slat source.

Detailed experimental work on specific component behavior has proceeded almost in parallel to the more global aforementioned airframe noise studies. Dobrzynski et al. [7] of the DLR used a 1/10th scaled Airbus-type high lift wing to quantify wing noise sources. Their findings did confirm the initial assumptions of Guo that under certain slat configurations vortex

shedding from the slat edge cove can result in excessive noise in the vicinity of the slat. This vortex shedding or unsteady flow separation at the slat cove and the ensuing unsteady mass fluctuations flowing through the slat trailing edge and main element leading edge formed the basis of Gou's initial formulation for slat noise prediction. However the tones present in the experiment were the result of laminar shedding off the slat cove. These tones were reduced by boundary layer tripping just upstream of the cove leading edge. Corresponding tonal behavior was observed in the surface measurements on the pressure side of the slat with broadband and tonal amplification observed in the sensors approaching the slat trailing edge. They conjectured that the noise produced from this laminar vortex shedding led to mean flow oscillations in the gap between the slat trailing edge and main element leading edge. Trailing edge noise was also identified as a slat source mechanism that influenced the low to intermediate frequencies of their study. Although it was observed that the flap side was the more dominate source in terms of noise per area (more localized) the noise emanating from the slat dominated the low to intermediate frequency ranges. It should be noted that the noise levels in the vicinity of the slat tracks or supports were typically ~ 8 dB higher than the levels in other slat regions in the 20 kHz range. It was suggested that his vortex shedding mechanism could be significantly reduced with the design of streamlined tracks and aligned in the flow direction.

Storms et al. [8] focused their aeroacoustic measurements on the leading edge slat using a high lift model consisting of several slat brackets, a main element, and a partial span outboard flap. Their phased array noise maps contained highly localized noise sources across the span of the slat that appeared to move outboard with frequency, a consequence of the model configuration. Static pressure measurements indicated that higher slat deflections resulted in higher suction at the slat trailing edge, lower slat loading, and a higher suction peak on the main element leading edge. Slat gap velocities were higher than the freestream velocity a result also observed in the PIV data of Moriarty et. al. [9] where gap velocities near 2x the freestream were measured. The integrated noise data did suggest that the noise levels were reduced as a function of decreasing slat deflection or decreasing slat gap velocity (for a fixed Mach number); however, using an M^5 amplitude correction the noise data did not collapse favorably with these gap velocities. Varying the main-element angle of attack indicated a non-linear relation between slat noise and slat gap velocity with main element deflection. They theorized that this behavior might be due to the state of the upper boundary layer of the slat. The higher slat deflections may have been laminar over the upper surface resulting in flow conditions inherently more sensitive to disturbances. Their computational analysis coupled with measurements suggest a feedback mechanism between vortex shedding at the slat trailing edge and Kelvin-Helmholtz instabilities from the slat cove region. Moriarty et. al. verified the mean flow behavior of Storms et. al. with PIV measurements but also observed that Turbulent Kinetic Energy (TKE) levels were highest in the slat gap region where the separating shear layer reattaches to the backside of the slat. They suggested that this region is likely to be the most energetic if feedback from the slat trailing edge amplifies disturbances in this region.

A number of computational studies have attempted to model slat noise generation and far field radiation (Guo [4], Khorrami, et. al. [10], Singer et. al. [11], and Khorrami et. al. [12]). Guo attempted to model the unsteady flow field around the cusp and through the slat gap using unsteady panel methods to solve the near field and the method of asymptotic expansion to derive the far field sound. Aside from presenting a simplified computational method, Guo's computations indicated that the slat radiates sound dominantly in the aft direction (fly-over).

More computationally intensive methods have since been utilized to address specific slat characteristics responsible for noise production. Khorrami et. al. utilized time accurate RANS methods to capture the vortex shedding off a blunt slat trailing edge. High frequency shedding was a problem observed in slat model test data from the Low Turbulence Pressure Tunnel (LTPT) at NASA LaRC for a 30-degree slat deflection. Their instantaneous fluctuating pressure results indicated the presence of low frequency oscillations in the slat cusp region. Singer et. al. confirmed the computational trailing edge vortex shedding results of Khorrami et. al. by using a permeable-surface FW-H model for the acoustic analysis. This approach accentuated the influence of the integration surface for noise computations. Their computations ultimately showed qualitative agreement in directivity with LTPT array data. The more recent work of Khorrami et. al. focused on modeling the shear layer from the slat cusp in an attempt to explain the low frequency slat noise levels. Computations supported the conjecture that the free shear layer originating from the slat cusp supports low frequency oscillations. Amplification was achieved via the Kelvin-Helmholtz instability mechanism and the disturbances resided in the low frequency range under investigation. However, far-field noise calculations were much lower than the measured low frequency slat noise.

Extensive aeroacoustic evaluations of high-lift devices have been conducted in the Quiet Flow Facility (QFF) of the NASA Langley Research Center in support of the airframe noise effort under the NASA initiated Advanced Subsonic Technology (AST) Program. Under the AST program effort, which includes participation from industry and academia as well as NASA, the unsteady flow in the leading edge slat region and the flap side edge have been identified as major sources of airframe noise for high lift conditions. Detailed flow and acoustic measurements have been made in the QFF to understand, predict, and reduce the noise from critical sources in the vicinity of a flap and slat under numerous operating conditions (Meadows et al. [13], Brooks et al. [14][15], etc.). Directional arrays and beamforming algorithms have been developed and utilized extensively throughout this program for noise source location, beamformed acoustic spectrum, and source directivity (Marcolini and Brooks [16], Brooks et al. [17]).

This study will discuss the results of 2-dimensional wing/slat model tests conducted in the QFF for various wing/slat model configurations and flow speeds up to $M = 0.17$, corresponding to a wing Reynolds number up to approximately 1.7 million. Data obtained from a Small Aperture Directional Array (SADA) of microphones positioned in the far field and fluctuating pressure sensors on the slat and main element surfaces are used to characterize key noise producing flow field structures and the ensuing distributed slat noise. In order to better quantify distributed noise sources from the leading-edge slat, our typical beamforming approach was modified to incorporate a routine for removing localized sources from the noise map. This approach allowed us to specifically focus on the distributed noise producing mechanisms such as the amplification of slat cove instabilities via the Kelvin-Helmholtz mechanism and the viscous shedding of the slat trailing edge. The massive collection of leading-edge slat noise data conducted by NASA LaRC specifically the research conducted in the QFF should facilitate validation of computational techniques with benchmark data pertaining to absolute noise levels and slat source directivity. In addition, this data will identify/confirm key sound producing mechanisms and form the physical basis for empirical models to predict the far-field sound levels associated with a leading edge slat.

2.2.2 Summary of the Array Processing Methodology

The flow field over a wing and slat consisting of a pressure side slat cove and a gap between the main element and slat trailing edge both spanning the slat will inherently induce a distributed sound source. In reality, the slat element and the main wing element are coupled via a support structure that in some aircraft configurations can be complex and bulky. Model tests of the wing/slat noise problem have been conducted with and without potentially representative support structures or brackets. These brackets may be local flow discontinuities and arguably significant noise sources. Even without utilizing brackets for model testing, other known local flow discontinuities or erroneous array processing results may be present resulting in or creating the appearance of localized sound sources. It has been observed in QFF model data that the nozzle side plate/slat junction can be a region containing relatively high noise levels, see for example Figure 10. This figure is a typical noise map from measured small aperture directional array (SADA) data illustrating the presence of both a distributed source and localized noise sources at a single frequency. Also indicated in this figure is key terminology to be discussed in paragraphs to follow. The noise emanating from the side plate regions (indicated hot spots below) is not of interest to the present study and in fact can mislead or misguide interpretations of the two-dimensional aeroacoustic phenomenon associated with the slat cove instabilities, viscous shedding of the trailing edge, etc. Furthermore, simply characterizing the slat noise problem by integrating only these local sources, whether due to brackets, facility side plates, or other local flow discontinuities, may potentially disregard a significant noise source contributor.

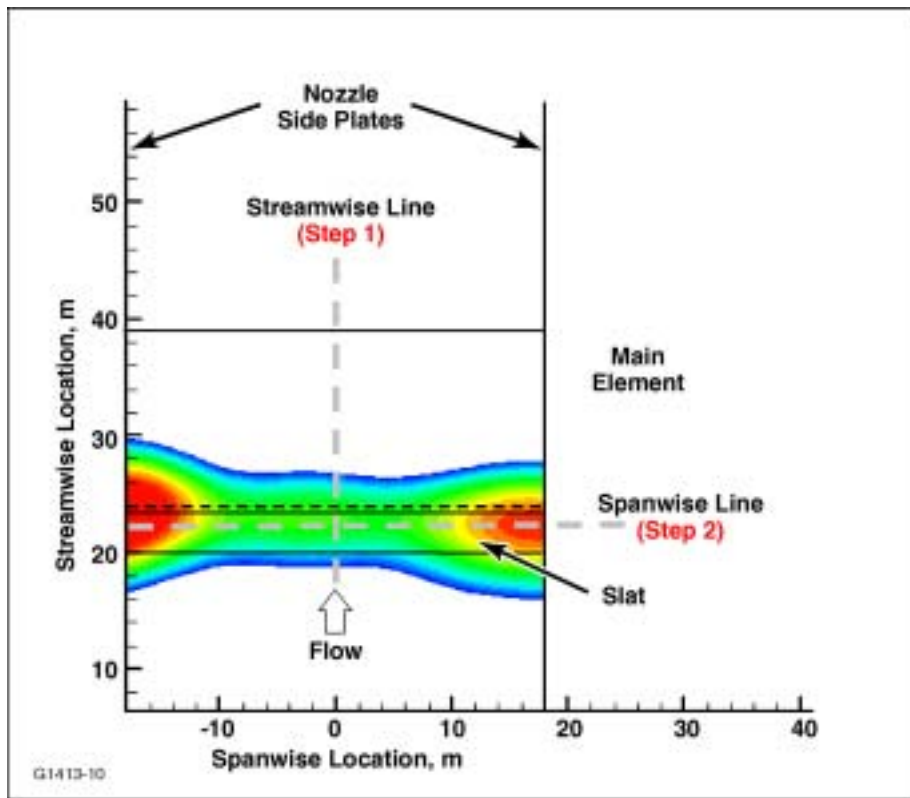


Figure 10. Pressure Side (Flyover) View of Distributed Slat Noise With Local Discontinuities at the Side Plates.

To overcome these potential pitfalls, a method was developed and implemented to decouple the noise due to localized sources from the noise of interest, the distributed noise sources in the wing/slat region. A breakdown into the three aforementioned sound sources is justified here because the noise map illustrated in Figure 10 is indeed typical of the noise maps encountered in our slat noise measurements. The decoupling approach takes into account the frequency dependent beam characteristics of the SADA culminating in distributed source spectra that is presented on a per foot basis (i.e., SPL/ft). The two dimensional spectral representation of the distributed noise spectra is used throughout to facilitate aeroacoustic scaling of the observed slat noise. The developed procedure to go from the measured SADA output to a distributed noise level per foot consists of essentially 6 steps. This process is summarized as follows:

- (1) Generate standard beamformed noise maps at each narrowband frequency for each test configuration. Search a standard noise map for the maximum noise level along the streamwise line located at the center of the slat (see Figure 10).
- (2) With the maximum streamwise location identified from step 1, search along the spanwise line passing through this point for peak levels P_{aT2}^2 and P_{aT3}^2 and a minimum P_{aTmin}^2 near the slat center. Note these levels and corresponding spanwise locations (see Figure 11). It is assumed that the noise sources at y_2 and y_3 are simple sources and that each of the identified P2 terms contains contributions from each of the other sources.

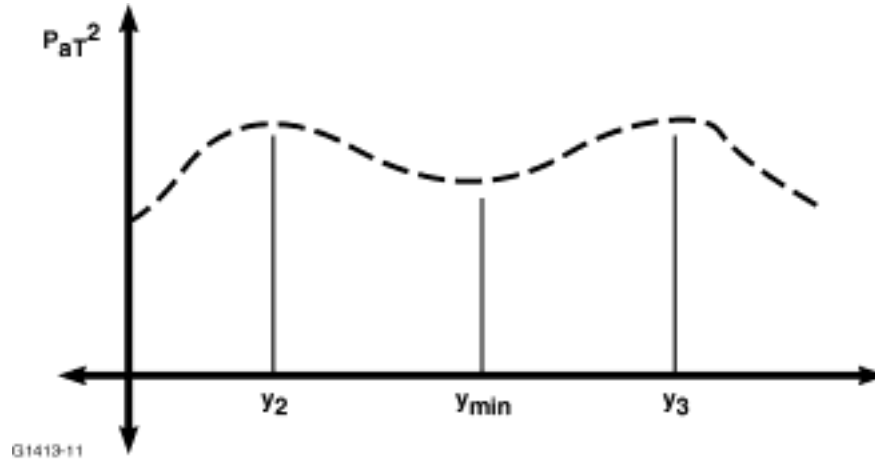


Figure 11. Pressure-Squared Values as a Function of Spanwise Position.

- (3) Compute the theoretical beam pattern characteristics at each narrow band frequency of interest along the spanwise line identified in step 2. The beam patterns are computed from the spatial filter function, W , for a point source located at the center of the scan line based on the following relation:

$$W(k, \bar{x}, \bar{x}_o) = \sum_{m=1}^{m_{tot}} w_m(k) \cdot \frac{r}{r_{m_o}} \cdot \exp \left[ik \left\{ (r_o - r) + \left(r_{m_o} - r_m \right) \right\} \right]$$

Where m_{tot} is the total number of microphones, $w_m(k)$ are known weighting factors associated with the SADA, r_o is the point source location relative to the array center, r is the scan point location relative to the array center, r_{mo} is the microphone to source distance, r_m is the microphone to scan point distance.

- (4) Compute a frequency dependent transfer function (F) based on an assumed step source distribution and the calculated values from step 3. This transfer function will correct the pressure squared distributed source data to pressure squared per foot. Steps 3 and 4 only need to be computed once due to the very small variation in streamwise position of the peak slat noise levels.
- (5) From the peak values of step 2 and the theoretical beam pattern results of step 3 the following linear system of equations is solved for P_{a1}^2 , P_2^2 , and P_3^2 representing the “true” distributed source level and localized source levels, respectively.

$$\begin{aligned} (P_{aT}^2)_{y_2} &= P_{a1}^2 + P_2^2 + P_3^2 \cdot f'(|y_3 - y_2|) \\ (P_{aT}^2)_{y_3} &= P_{a1}^2 + P_2^2 \cdot f'(|y_2 - y_3|) + P_3^2 \\ (P_{aT}^2)_{y_{\min}} &= P_{a1}^2 + P_2^2 \cdot f'(|y_2 - y_{\min}|) + P_3^2 \cdot f'(|y_3 - y_{\min}|) \end{aligned}$$

Where f' is a frequency and position dependent function computed from the theoretical array output of step 3, y_2 , y_3 , and y_{\min} are the localized source positions and the location of the minimum distributed source level (between the localized sources), respectively.

- (6) Multiply the distributed source level, P_{a1}^2 , from step 5 by the correction factor computed in step 4 to obtain the distributed source per foot spectrum [P_{a1}^2 per foot = $P_{a1}^2 * F$].

Figure 12 illustrates the results of this processing by comparing each contribution to the measured array output. Included in this figure is the output from the array scanned to the center of the main element at the leading edge. The total slat and bracket noise is the sum of each of the components computed in step 5. As seen by this figure, for this test configuration the localized sources have a small influence on the total slat noise. This figure accentuates the relative importance of the distributed sound source and the potential errors associated with neglecting this source. Further examples of the application of this process are presented in the next section.

2.2.3 Summary of Results

Extensive aeroacoustic evaluations of high-lift devices have been conducted in the Quiet Flow Facility (QFF) of the NASA Langley Research Center in support of the airframe noise effort under the NASA initiated Advanced Subsonic Technology (AST) Program. Figure 13 shows the overall test set-up and the location of the SADA that was used to acquire the acoustic data used in this study. Three configurations were studied: a baseline (Table 2), trailing edge thickness (Table 3), and teardrop insert (Table 4).

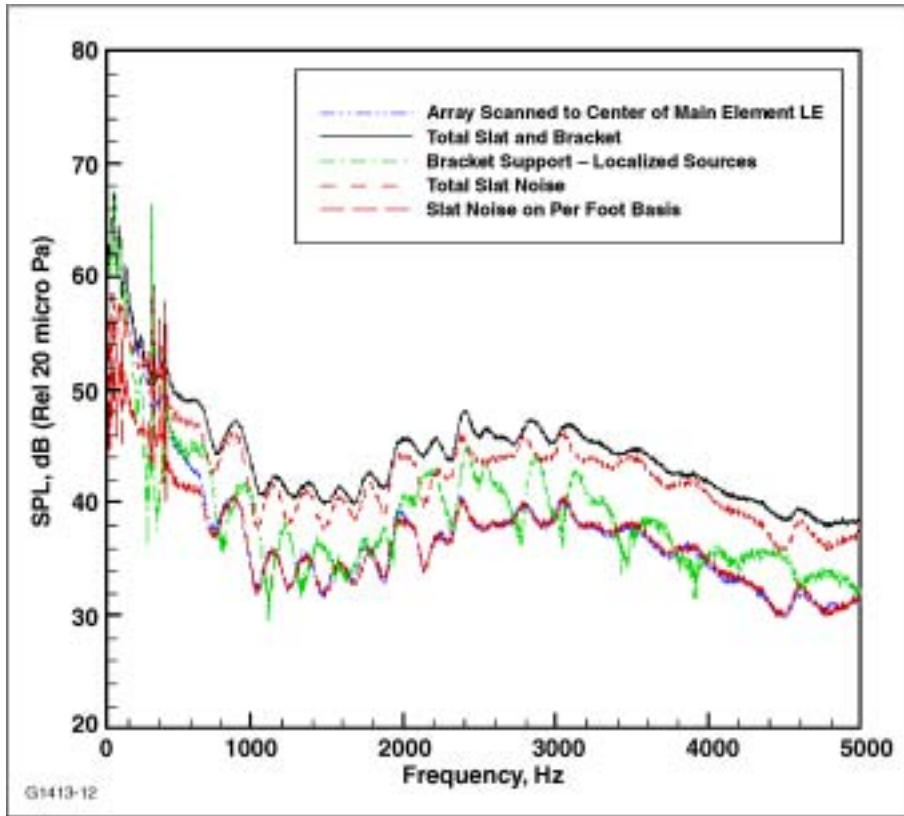


Figure 12. Breakdown of Slat Noise Contributions for $M=0.17$, $\delta_s = 20^\circ$, $\delta_w = 26^\circ$, $\Psi = 0^\circ$, and $\Phi = 107^\circ$.

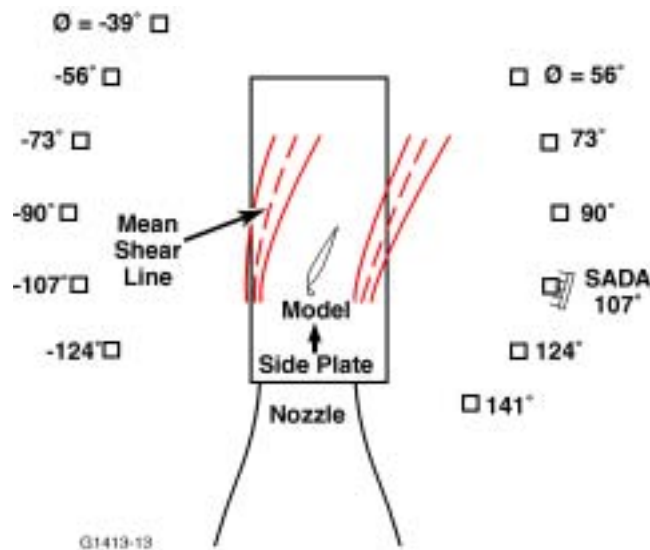


Figure 13. Schematic Diagram of the Slat/Wing Model and Elevation Angle Position (Side View).

Table 2. Processed Baseline Configurations.

Slat Per-Foot Processing														
<i>Processing Status - Baseline Perfot</i>														
Test	Run	Background Run	Group	M#	AoA	Slat	SADA Elev	SADA Azim	Treatment	Tunnel Temp, deg F	Array X Location (Tunnel Coor)	Array Y Location (Tunnel Coor)	Array Z Location (Tunnel Coor)	Source-Observer Distance
1020	12	1	4	0.17	26	20	141	0	Baseline	82.1	-7.1288	0.0000	-43.0092	52.9060
1020	13	1	4	0.17	26	20	124	0	Baseline	82.6	5.9484	0.0000	-54.9923	57.5262
1020	14	1	4	0.17	26	20	107	0	Baseline	82.8	21.9577	0.0000	-62.6282	62.1844
1020	15	1	4	0.17	26	20	90	0	Baseline	82.9	39.5000	0.0000	-65.2500	66.5076
1021	2	1	4	0.17	26	20	73	0	Baseline	80.6	57.0423	0.0000	-62.6282	70.2117
1021	3	1	4	0.17	26	20	56	0	Baseline	80.8	73.0516	0.0000	-54.9923	73.0887
1066	12	1	4	0.17	26	20	141	0	Slat Moved Closer to Main Element	87.0	-7.1288	0.0000	-43.0092	52.9060
1067	2	1	4	0.17	26	20	124	0	Slat Moved Closer to Main Element	80.4	5.9484	0.0000	-54.9923	57.5262
1067	3	1	4	0.17	26	20	107	0	Slat Moved Closer to Main Element	80.2	21.9577	0.0000	-62.6282	62.1844
1067	4	1	4	0.17	26	20	90	0	Slat Moved Closer to Main Element	80.3	39.5000	0.0000	-65.2500	66.5076
1067	5	1	4	0.17	26	20	73	0	Slat Moved Closer to Main Element	80.3	57.0423	0.0000	-62.6282	70.2117
1067	6	1	4	0.17	26	20	56	0	Slat Moved Closer to Main Element	80.5	73.0516	0.0000	-54.9923	73.0887
1166	12	1	4	0.17	26	20	141	0	50% Closed, 6 Notches	56.5	-7.1288	0.0000	-43.0092	52.9060
1166	13	1	4	0.17	26	20	124	0	50% Closed, 6 Notches	56.5	5.9484	0.0000	-54.9923	57.5262
1166	14	1	4	0.17	26	20	107	0	50% Closed, 6 Notches	56.4	21.9577	0.0000	-62.6282	62.1844
1166	15	1	4	0.17	26	20	90	0	50% Closed, 6 Notches	55.9	39.5000	0.0000	-65.2500	66.5076
1166	16	1	4	0.17	26	20	73	0	50% Closed, 6 Notches	55.9	57.0423	0.0000	-62.6282	70.2117
1166	17	1	4	0.17	26	20	56	0	50% Closed, 6 Notches	55.9	73.0516	0.0000	-54.9923	73.0887
Output File Naming Convention:														
Octave Map														
Geometry File														
Line Profiles														
Per-Foot File														
Main Element Leading Edge at (24.354",0.0",-0.490") for AoA=26 deg														

Table 3. Processed Trailing Edge Thickness Configurations.

Slat Per-Foot Processing															
<i>Processing Status - Trailing Edge Thickness Perfoot</i>															
Test	Run	Background Test	Background Run	Group	M#	AoA	Slat	SADA Elev	SADA Azim	Trailing Edge Thickness	Tunnel Temp, deg F	Array X Location (Tunnel Coor)	Array Y Location (Tunnel Coor)	Array Z Location (Tunnel Coor)	Source-Observer Distance
1038	12	1038	1	4	0.17	26	20	141	0	0.005" (Baseline)	83.6	-7.1288	0.0000	-43.0092	52.9060
1038	13	1038	1	4	0.17	26	20	124	0	0.005" (Baseline)	83.8	5.9484	0.0000	-54.9923	57.5262
1038	14	1038	1	4	0.17	26	20	107	0	0.005" (Baseline)	83.8	21.9577	0.0000	-62.6282	62.1844
1038	15	1038	1	4	0.17	26	20	90	0	0.005" (Baseline)	83.9	39.5000	0.0000	-65.2500	66.5076
1038	16	1038	1	4	0.17	26	20	73	0	0.005" (Baseline)	83.9	57.0423	0.0000	-62.6282	70.2117
1038	17	1038	1	4	0.17	26	20	56	0	0.005" (Baseline)	83.9	73.0516	0.0000	-54.9923	73.0887
1041	12	1038	12	4	0.17	26	20	141	0	0.033"	81.2	-7.1288	0.0000	-43.0092	52.9060
1041	13	1038	13	4	0.17	26	20	124	0	0.033"	81.5	5.9484	0.0000	-54.9923	57.5262
1041	14	1038	14	4	0.17	26	20	107	0	0.033"	81.2	21.9577	0.0000	-62.6282	62.1844
1041	15	1038	15	4	0.17	26	20	90	0	0.033"	81.1	39.5000	0.0000	-65.2500	66.5076
1041	16	1038	16	4	0.17	26	20	73	0	0.033"	81.1	57.0423	0.0000	-62.6282	70.2117
1041	17	1038	17	4	0.17	26	20	56	0	0.033"	80.6	73.0516	0.0000	-54.9923	73.0887
1044	12	1038	12	4	0.17	26	20	141	0	0.070"	88.2	-7.1288	0.0000	-43.0092	52.9060
1044	13	1038	13	4	0.17	26	20	124	0	0.070"	88.6	5.9484	0.0000	-54.9923	57.5262
1044	14	1038	14	4	0.17	26	20	107	0	0.070"	88.6	21.9577	0.0000	-62.6282	62.1844
1044	15	1038	15	4	0.17	26	20	90	0	0.070"	89.8	39.5000	0.0000	-65.2500	66.5076
1044	16	1038	16	4	0.17	26	20	73	0	0.070"	90.0	57.0423	0.0000	-62.6282	70.2117
1044	17	1038	17	4	0.17	26	20	56	0	0.070"	90.0	73.0516	0.0000	-54.9923	73.0887
1049	12	1038	12	4	0.17	26	20	141	0	0.155"	84.3	-7.1288	0.0000	-43.0092	52.9060
1049	13	1038	13	4	0.17	26	20	124	0	0.155"	84.4	5.9484	0.0000	-54.9923	57.5262
1049	14	1038	14	4	0.17	26	20	107	0	0.155"	84.6	21.9577	0.0000	-62.6282	62.1844
1049	15	1038	15	4	0.17	26	20	90	0	0.155"	84.5	39.5000	0.0000	-65.2500	66.5076
1049	16	1038	16	4	0.17	26	20	73	0	0.155"	84.3	57.0423	0.0000	-62.6282	70.2117
1049	17	1038	17	4	0.17	26	20	56	0	0.155"	84.3	73.0516	0.0000	-54.9923	73.0887
Output File Naming Convention:															
Octave Map															
Geometry File															
Line Profiles															
Per-Foot File															
Main Element Leading Edge at (24.354",0.0",-0.490") for AoA=26 deg															
Main Element Leading Edge at (24.483",0.0",-0.202") for AoA=32 deg															

Table 4. Processed Teardrop Insert Configurations.

Slat Per-Foot Processing														
<i>Processing Status - Teardrop Perfoot</i>														
Test	Run	Background Run	Group	M#	AoA	Slat	SADA Elev	SADA Azim	Treatment	Tunnel Temp, deg F	Array X Location (Tunnel Coor)	Array Y Location (Tunnel Coor)	Array Z Location (Tunnel Coor)	Source-Observer Distance
1087	9	1	4	0.17	32	20	107	0	Baseline	75.4	21.9577	0.0000	-62.6282	62.4773
1093	2	1	4	0.17	32	10	107	0	Baseline	71.7	21.9577	0.0000	-62.6282	62.4773
1095	10	1	4	0.17	26	10	107	0	Baseline	72.0	21.9577	0.0000	-62.6282	62.1844
1099	2	1	4	0.07	26	30	107	0	Baseline	70.3	21.9577	0.0000	-62.6282	62.1844
1099	3	1	4	0.09	26	30	107	0	Baseline	69.9	21.9577	0.0000	-62.6282	62.1844
1099	6	1	4	0.11	26	30	107	0	Baseline	69.9	21.9577	0.0000	-62.6282	62.1844
1099	10	1	4	0.13	26	30	107	0	Baseline	71.0	21.9577	0.0000	-62.6282	62.1844
1099	11	1	4	0.15	26	30	107	0	Baseline	71.0	21.9577	0.0000	-62.6282	62.1844
1099	14	1	4	0.17	26	30	107	0	Baseline	71.7	21.9577	0.0000	-62.6282	62.1844
1154	14	1	4	0.17	32	30	107	0	Baseline	76.0	21.9577	0.0000	-62.6282	62.4773
1164	2	1	4	0.07	26	20	107	0	Teardrop insert	59.1	21.9577	0.0000	-62.6282	62.1844
1164	3	1	4	0.09	26	20	107	0	Teardrop insert	57.7	21.9577	0.0000	-62.6282	62.1844
1164	6	1	4	0.11	26	20	107	0	Teardrop insert	54.0	21.9577	0.0000	-62.6282	62.1844
1164	10	1	4	0.13	26	20	107	0	Teardrop insert	52.4	21.9577	0.0000	-62.6282	62.1844
1164	11	1	4	0.15	26	20	107	0	Teardrop insert	52.0	21.9577	0.0000	-62.6282	62.1844
1164	14	1	4	0.17	26	20	107	0	Teardrop insert	50.6	21.9577	0.0000	-62.6282	62.1844
1168	14	1	4	0.17	26	20	107	0	TE taped - slat closed - 9 notches	55.3	21.9577	0.0000	-62.6282	62.1844
Output File Naming Convention:														
Octave Map														
Geometry File														
Line Profiles														
Per-Foot File														
Main Element Leading Edge at (24.354",0.0",-0.490") for AoA=26 deg														
Main Element Leading Edge at (24.483",0.0",-0.202") for AoA=32 deg														

Figure 14 shows the comparison of the narrowband sound pressure level for the wing at 26° angle of attack for Test 1020 (Table 2) and 32° angle of attack for Test 1087 (Table 4). The figure shows that the noise levels decrease as the angle of attack decreases. Figure 15 shows the affect of changing slat angle of attack for a wing angle of attack of 26° by comparing the slat angles of 10° for Test 1095 (Table 4), 20° for Test 1020 (Table 2), and 30° for Test 1099 (Table 4). The measured sound levels decrease as the slat angle of attack decreases. Figure 16 shows the same slat angle of attack trends for the wing angle of attack of 32° using Tests 1087, 1093, and 1154 (Table 4).

Figure 17 shows that decreasing the slat gap (or increasing the overlap) also reduces the leading edge slat noise. Tests 1020, 1067, and 1166 (Table 2) and 1168 (Table 4) are plotted to show the trend.

Figure 18 shows the effect of the teardrop insert from Test 1164 (Table 4) as compared to the baseline configuration from Test 1020 (Table 2). It is clearly seen that the teardrop insert lowered the leading edge slat noise in the mid frequency range of 10 kHz to 45kHz. However, the low frequency noise appeared to be amplified by the teardrop insert. Figure 19 shows the effect of increasing Mach number on the teardrop insert configuration. The increasing Mach number consistently results in an increase noise level.

Figure 20 to Figure 23 show the directivity characteristics, in both absolute and normalized form, of the baseline configuration from Test 1020 and 6-notch gap/overlap configuration from Test 1166 (Table 2). It can be seen that once properly normalized, the directivity effect can be removed.

Figure 24 to Figure 28 show the effects of trailing edge thickness using the data from Tests 1038, 1044, and 1049 (Table 3). Figure 24 shows that the baseline trailing edge thickness of 0.005" has the lowest noise levels, and that increasing the thickness produces an additional noise source that has a peak frequency related to the trailing edge thickness. The directivity characteristics of the sound pressure level are also changed by the new apparent source.

Finally, Figure 29 provides a summary of the noise reduction techniques evaluated in this study. Clearly the most effective reduction was obtained by losing the slat gap. However, a moderate reduction was achieved with the use of the teardrop insert.

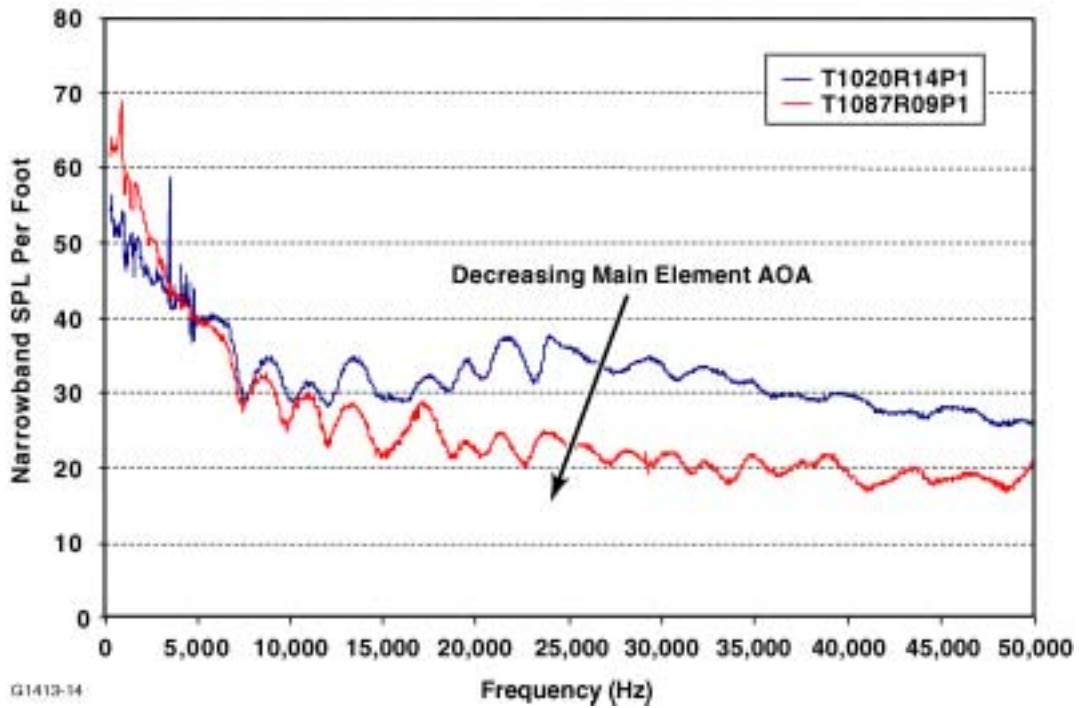


Figure 14. Effect of the Main Element Angle-of-Attack on the Leading Slat Noise.

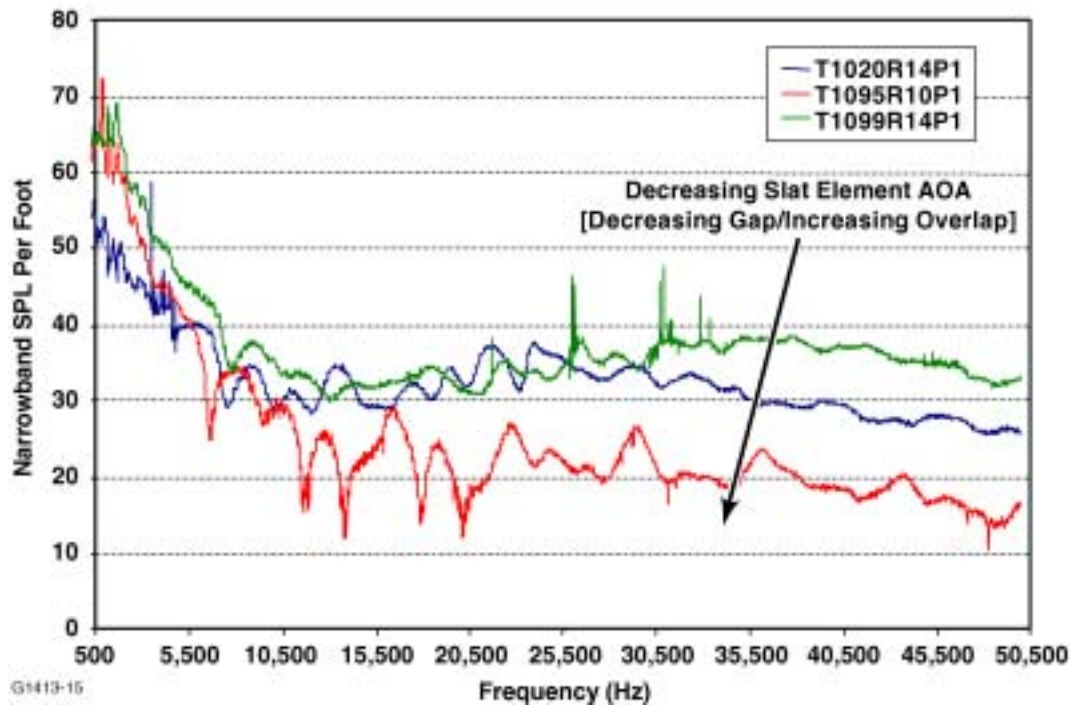


Figure 15. Effect of Slat Element Angle-of-Attack for a Main Element Angle-of-Attack of 26 Degrees.

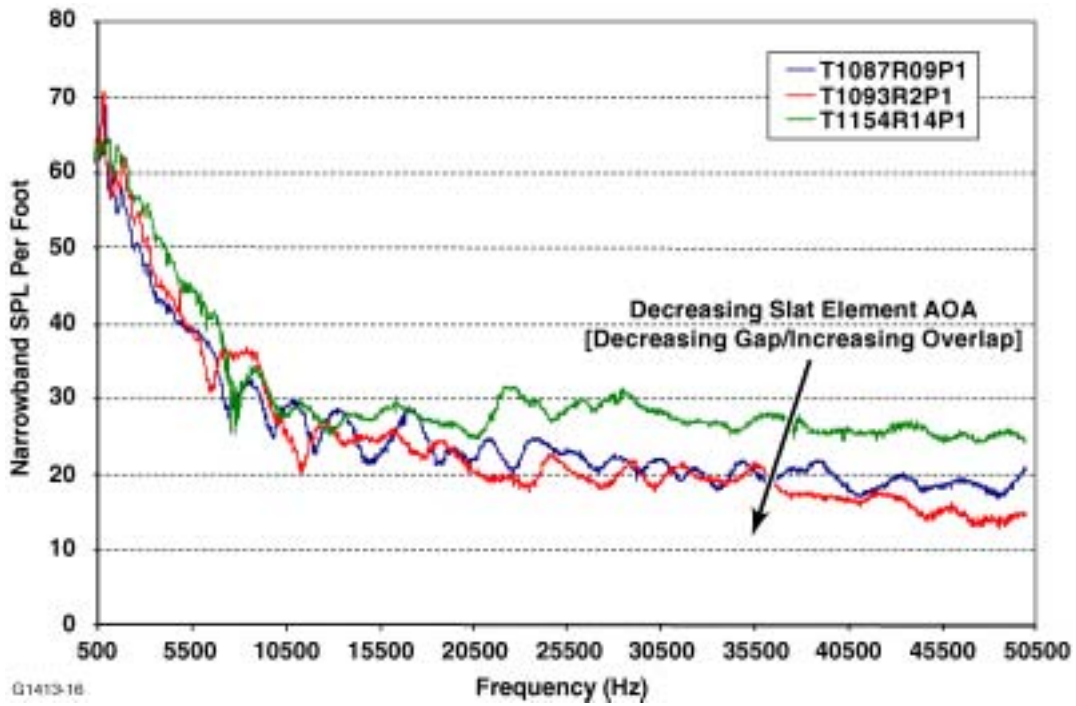


Figure 16. Effect of Slat Element Angle-of-Attack for a Main Element Angle-of-Attack of 32 Degrees.

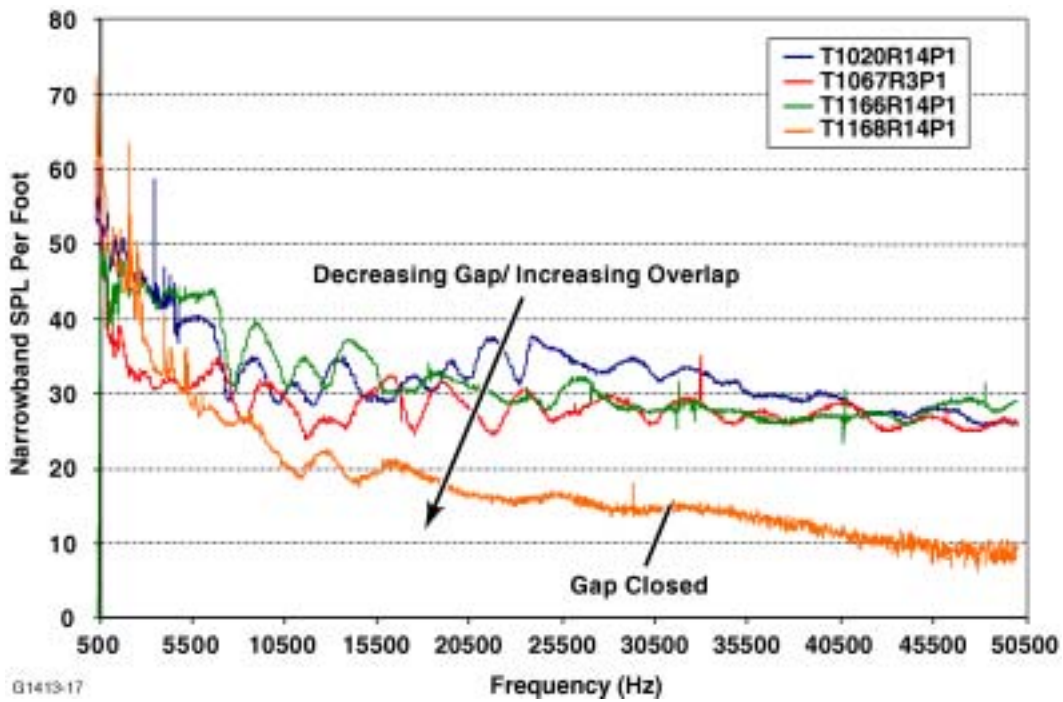


Figure 17. Effect of Slat Gap/Overlap on the Sound Pressure Level of the Leading Edge Slat Noise.

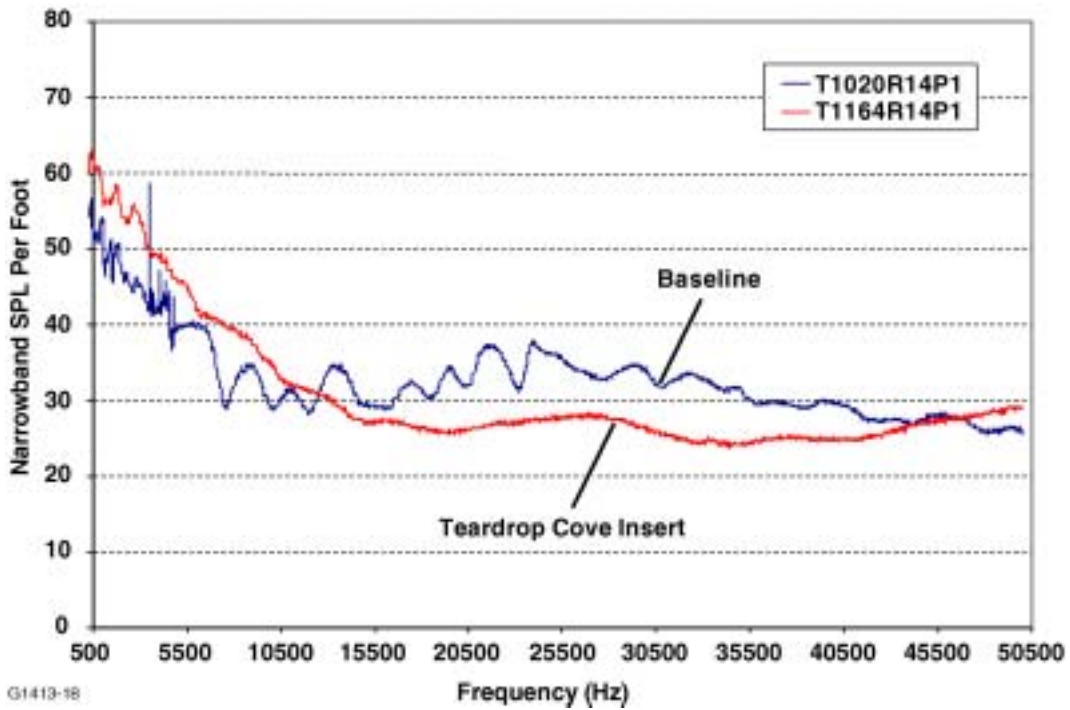


Figure 18. Effect of the Teardrop Insert in the Slat Gap on the Sound Pressure Level of the Leading Edge Slat Noise.

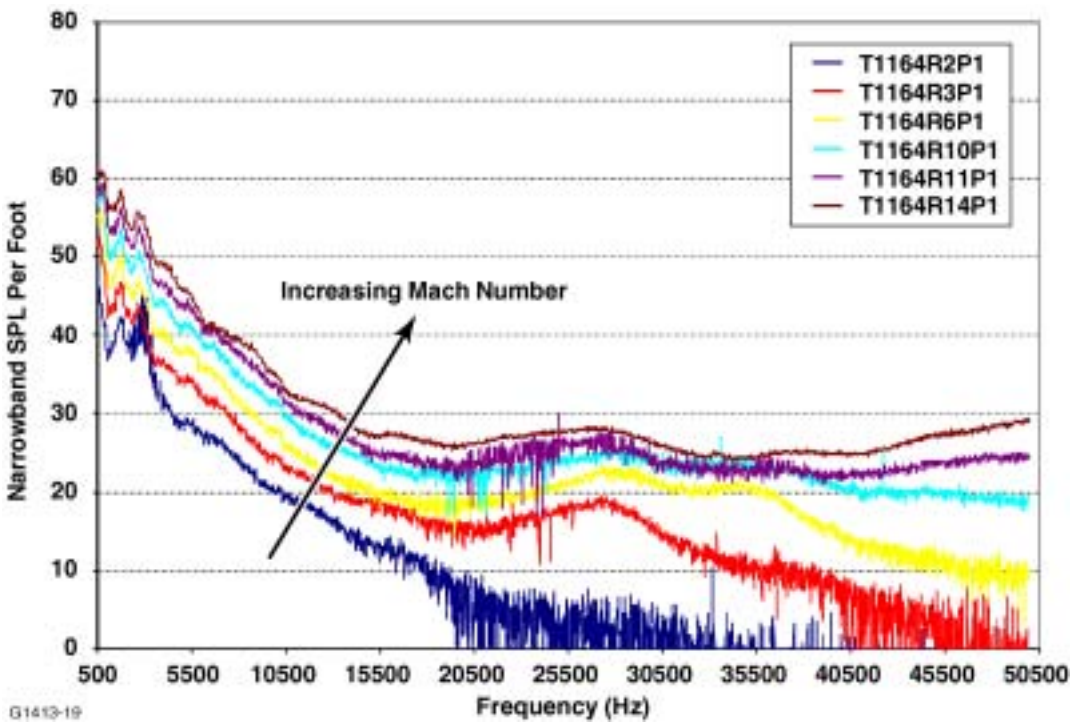


Figure 19. Effect of Mach Number on the Teardrop Insert Leading Edge Slat Noise.

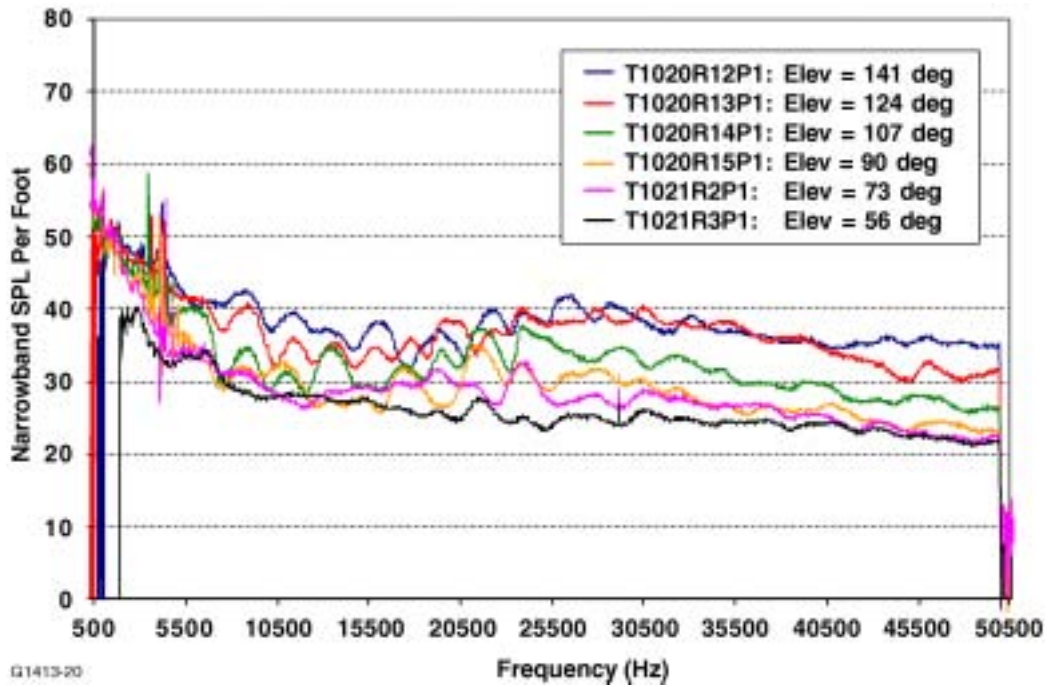


Figure 20. Effect of Directivity Angle on the Sound Pressure Level of the Baseline Leading Edge Slat Configuration.

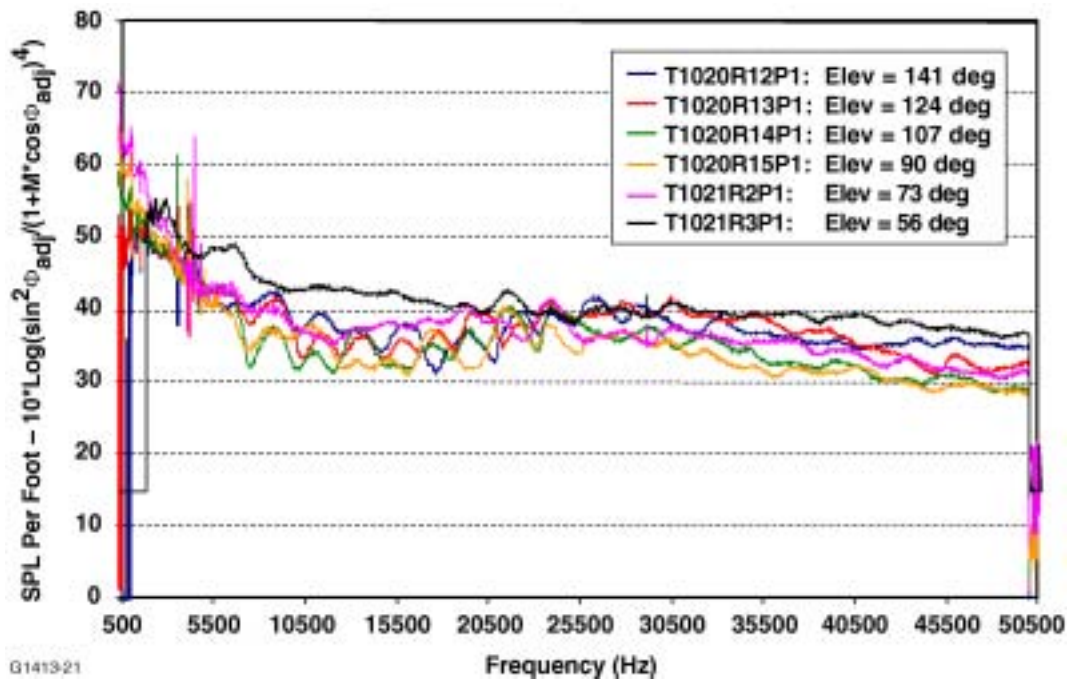


Figure 21. Normalized Directivity (Using Adjusted Angles) of the Baseline Leading Edge Slat Configuration.

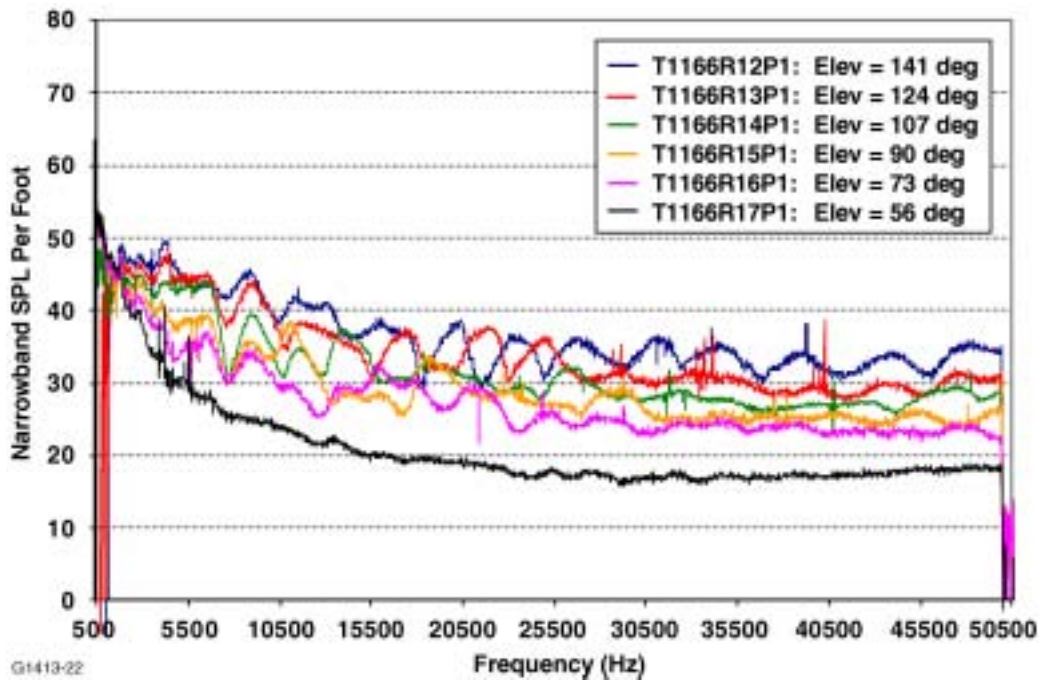


Figure 22. Directivity Characteristics of the Sound Pressure Level for the 6-Notch Gap/Overlap Conditions.

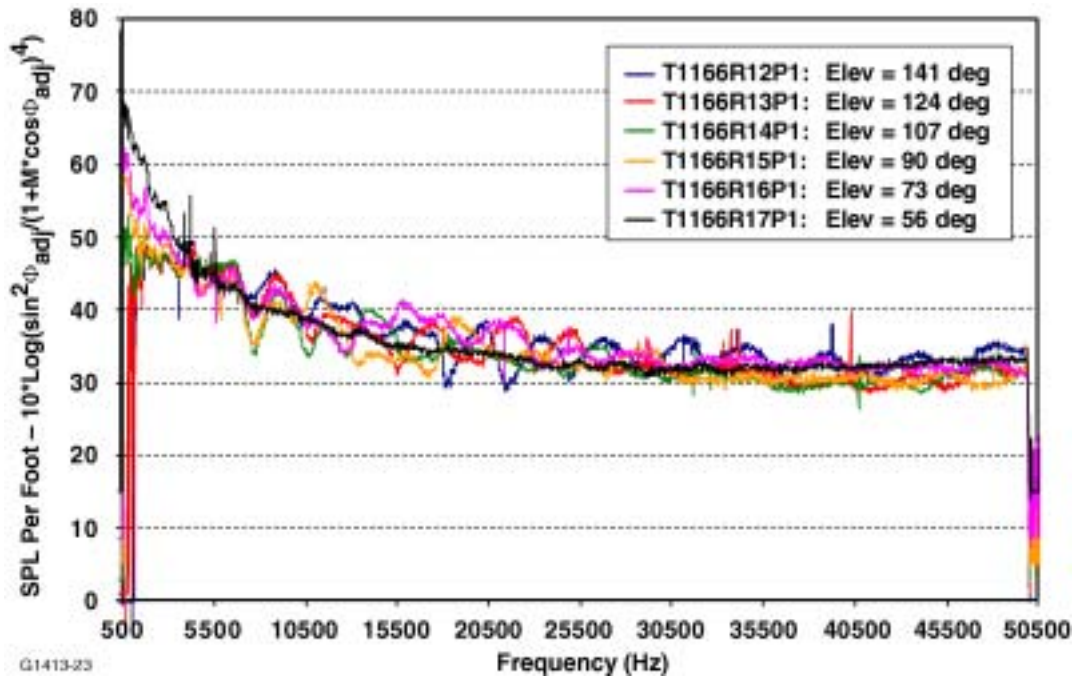
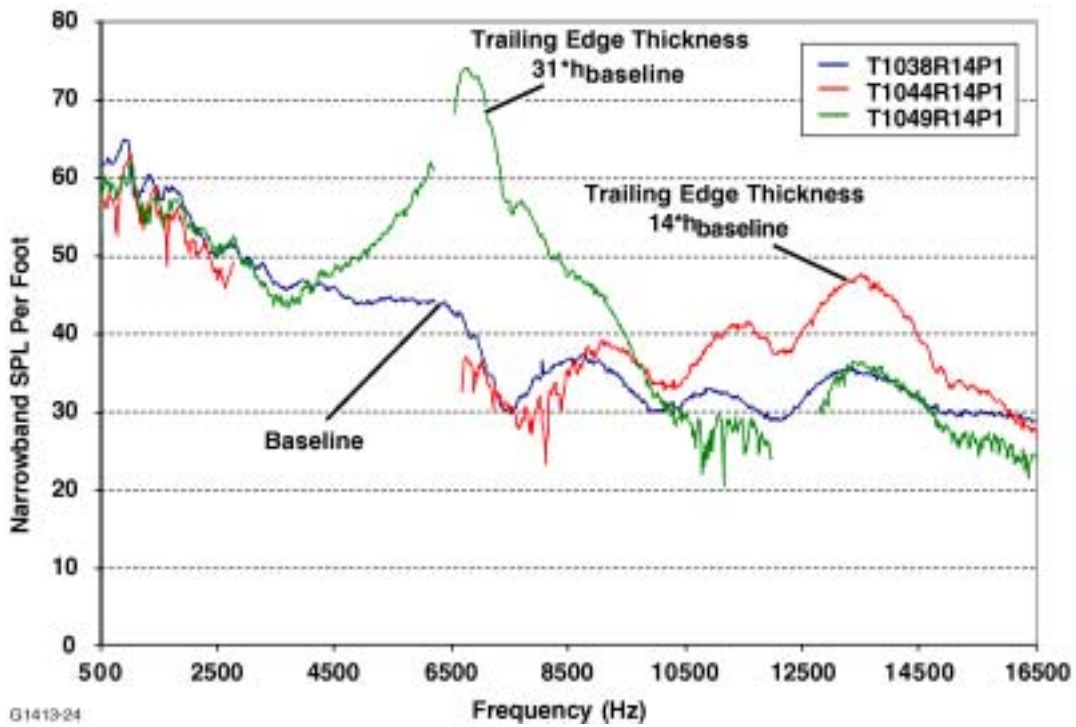
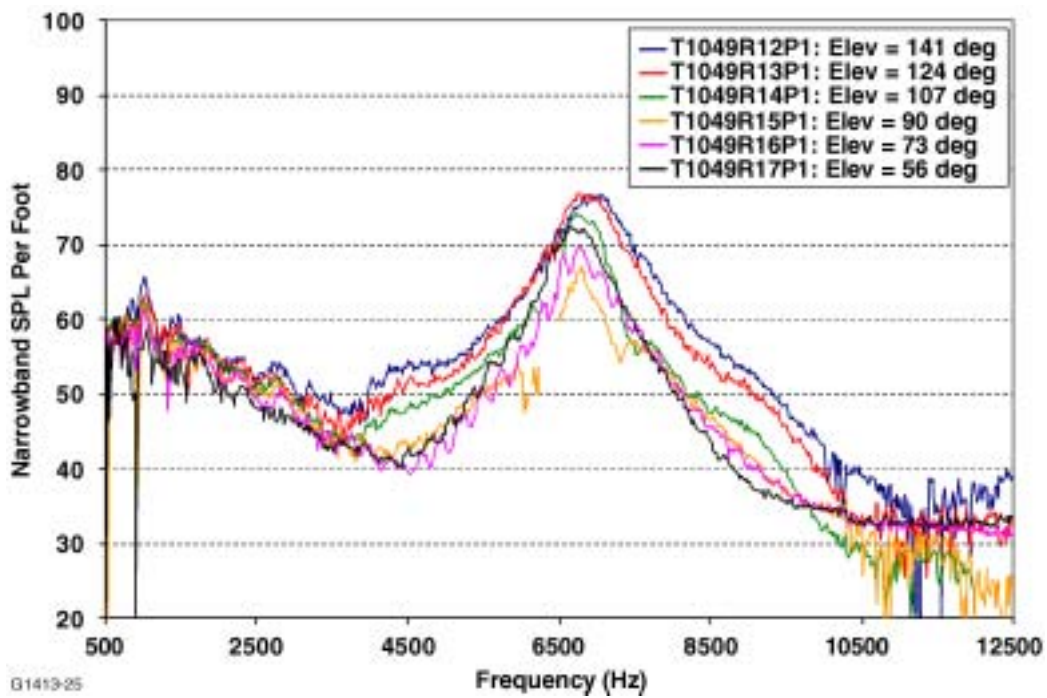


Figure 23. Normalized Directivity (Using Adjusted Angles) of the 6-Notch Gap/Overlap Conditions.



G1413-24

Figure 24. Effect of Trailing Edge Thickness on the Leading Edge Slat Noise.



G1413-25

Figure 25. Directivity Characteristics of the Sound Pressure Level for the Trailing Edge Thickness of 0.155".

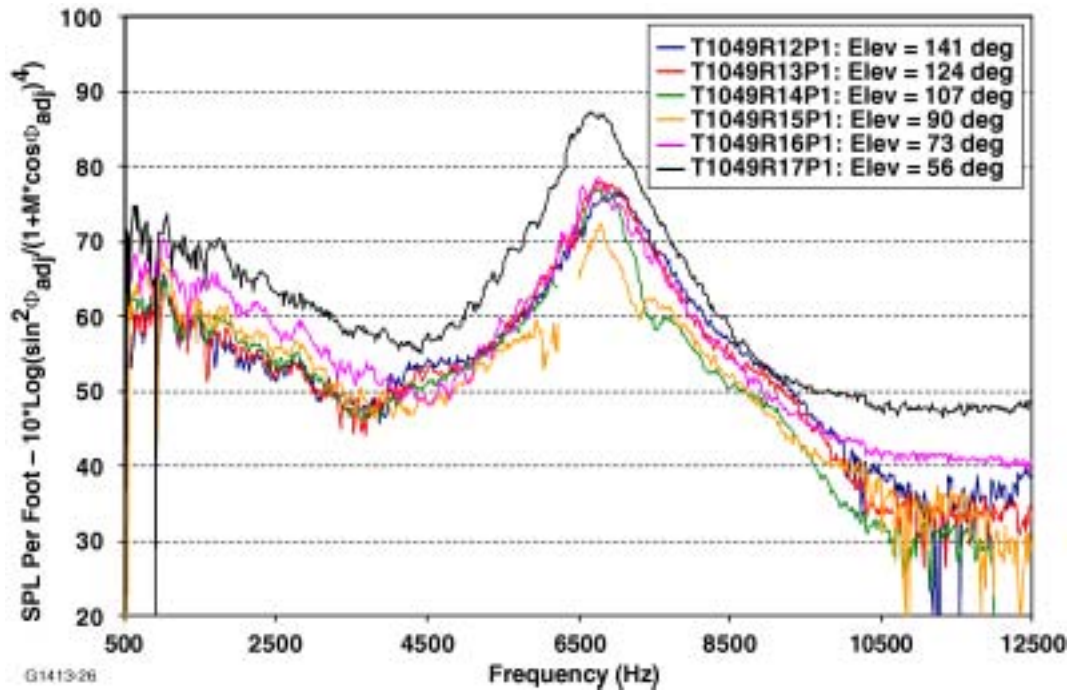


Figure 26. Normalized Directivity (Using Adjusted Angles) for the Trailing Edge Thickness of 0.155".

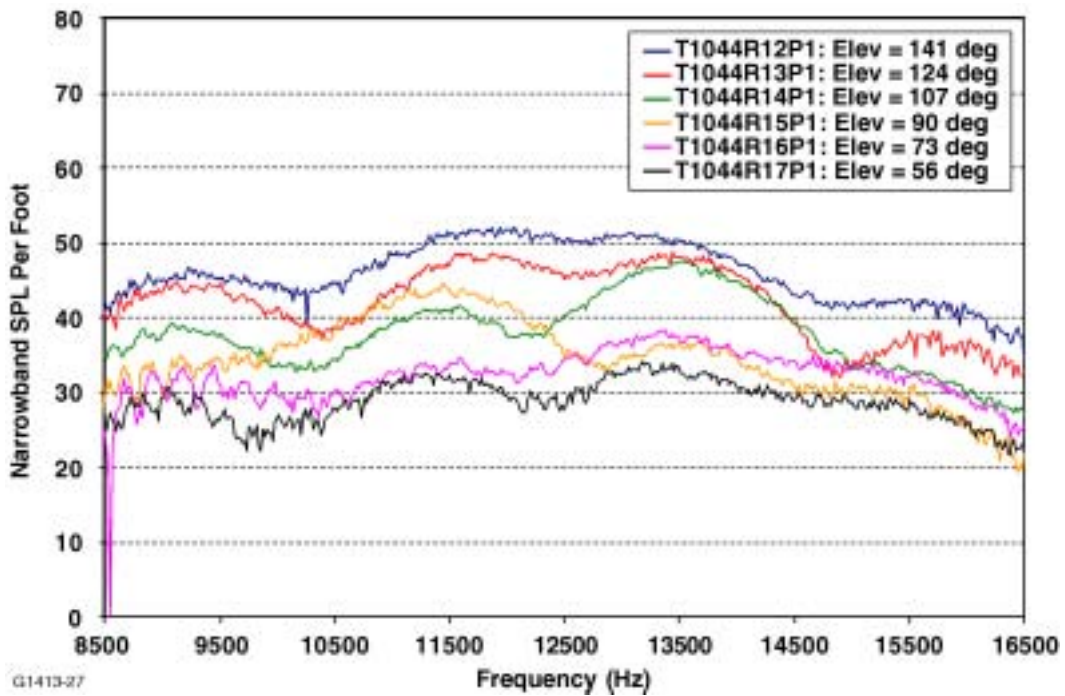


Figure 27. Directivity Characteristics of the Sound Pressure Level for the Trailing Edge Thickness of 0.07".

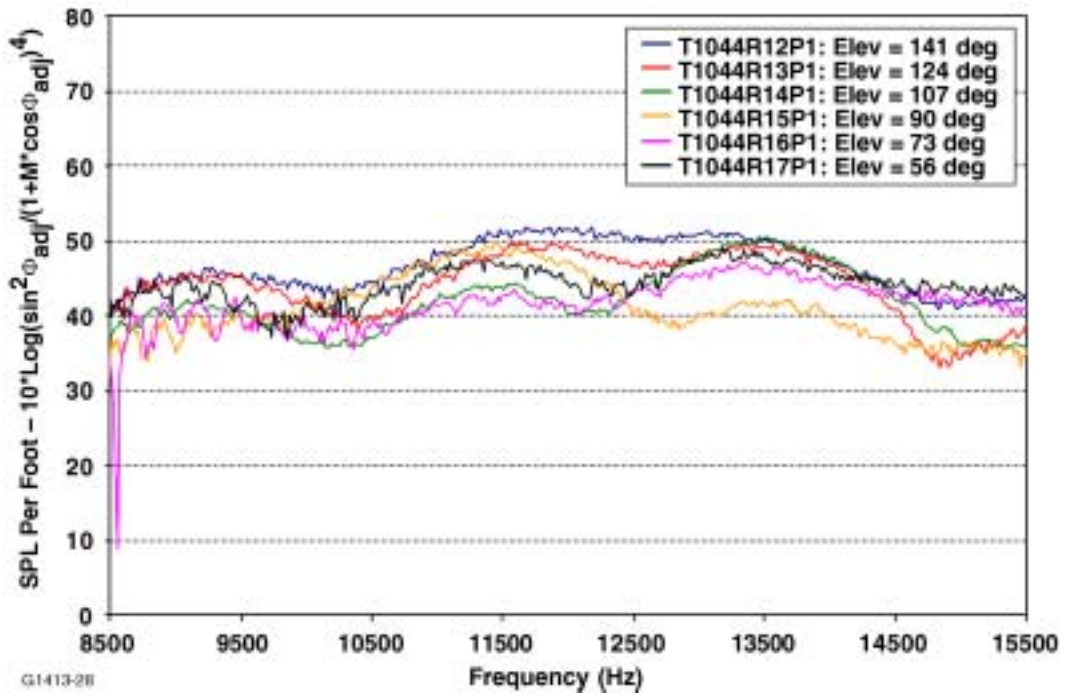


Figure 28. Normalized Directivity (Using Adjusted Angles) for the Trailing Edge Thickness of 0.07".

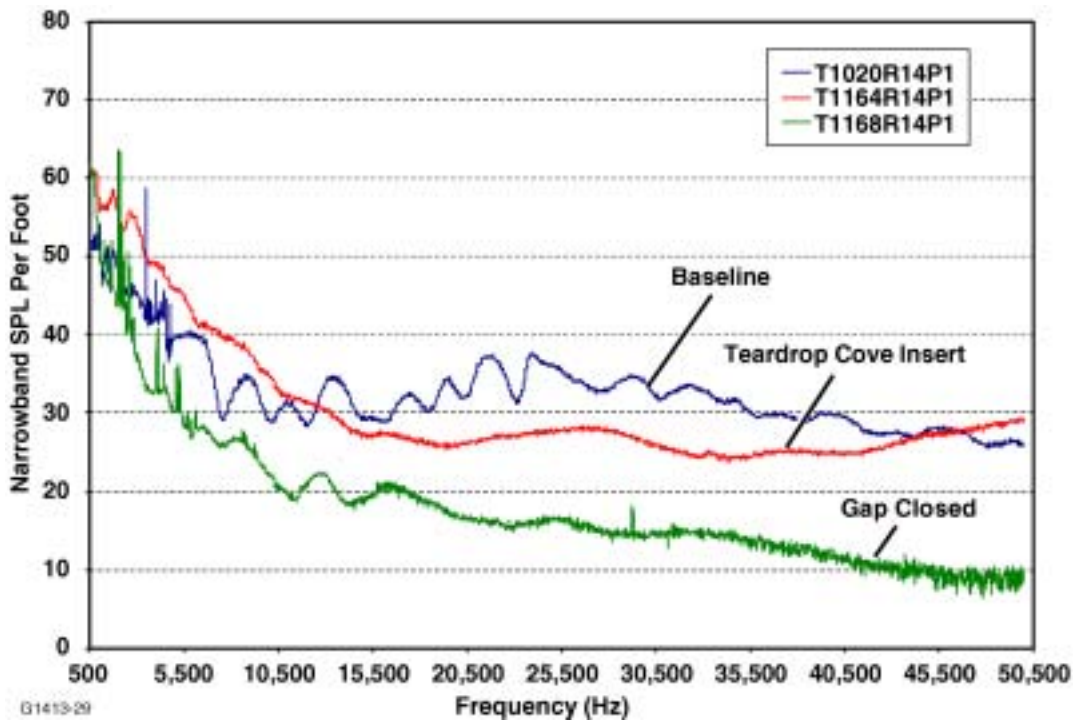


Figure 29. Summary of the Noise Benefit for the Two Slat Noise Reduction Concepts.

2.2.4 List of Symbols

f'	Frequency dependent function based on theoretical array pattern
F	Transfer function for per-foot processing of spectra
m	Microphone number
m_{tot}	Total number of microphones
M	Freestream flow Mach number
P_{a1}^2	True distributed source pressure squared
P_2^2	True localized source pressure squared at y_2
P_3^2	True localized source pressure squared at y_3
$P_{aT\text{min}}^2 = (P_{aT}^2)_{y_{\text{min}}}$	Minimum pressure squared along span line as measured by SADA
$P_{aT2}^2 = (P_{aT}^2)_{y_2}$	Peak pressure squared along span line as measured by SADA
$P_{aT3}^2 = (P_{aT}^2)_{y_3}$	Peak pressure squared along span line as measured by SADA
r	Scan point location relative to array center
r_o	Point source location relative to array center
r_m	Microphone to scan point distance
r_{m0}	Microphone to source distance
y_{min}	Spanwise location of minimum pressure squared
y_2	Spanwise location of peak pressure squared
y_3	Spanwise location of peak pressure squared
W	Spatial filter function
w_m	SADA weighting factors
δ_s	Slat angle of attack
δ_w	Wing angle of attack
Ψ	Array azimuth angle
Φ	Array elevation angle

3. JET SHEAR LAYER REFRACTION AND ATTENUATION STUDY

3.1 Introduction and Review of Correction Procedures

3.1.1 Static-to-Flight Correction Procedures

Aircraft fly-over noise prediction programs such as ANOPP [41] play a central role in community noise assessments. Successful prediction methods require a proper accounting of a number of noise generation and propagation effects [25]. Static engine noise measurements are often used with these programs to provide increased accuracy over direct component noise predictions, but not without difficulty. A fundamental problem is that the noise levels acquired statically, even under controlled conditions using inflow control devices, do not faithfully represent the noise levels that are encountered in flight. The sound spectra and directivity are modified by source motion, and in order to use static engine noise measurements for aircraft noise prediction, several motion-related effects must be accounted for. One familiar effect is the Doppler shift in frequency of the sound received by a stationary observer, and is easily accounted for by applying a Doppler correction factor to the statically measured frequency spectrum. An equally important effect is the modification of the sound amplitude arising from changes to the noise generation or propagation process when the source is in motion. Correction procedures that account for these so-called convective or dynamic amplification effects are more difficult to establish.

Convective amplification is concerned with fundamental differences between noise fields radiated by stationary and moving sources. Differences may arise as a result of changes in the noise generating mechanisms themselves, as in the case of jet noise where the shear layer strength and hence the noise generation process is significantly altered by aircraft motion. Differences may also arise simply from the dynamics of the motion, as in the case of a moving monopole where the noise generating mechanism (an oscillating point mass flux) remains unchanged but the radiated sound field is modified by motion. Differences may also arise as a result of changes in the surrounding flowfield that alter the propagation of the sound. The corrections that are used to account for convective amplification effects then depend upon the physical mechanisms involved.

Corrections that account for changes in the noise generating mechanisms require a understanding of the major parameters that govern the noise generation, one example being the jet-noise correction procedure described in reference [39]. Correction procedures that account for changes in the sound field of moving sources whose characteristic generating mechanisms are left essentially unchanged require a thorough understanding of how the noise radiation is modified by motion. Simple corrections based on analytical for idealized point sources are available, and are often used as approximate corrections for realistic noise sources. Correction procedures that account for changes in the sound field due to propagation differences when the source is in motion require an understanding of how the surrounding flow is modified by motion.

The present effort is concerned with the effects of a flow-field modification that takes place in the exhaust region. Internally generated engine exhaust noise that propagates through the propulsive jet must transit the jet shear layer on its way to an observer. As this sound crosses the shear layer, it can be refracted, reflected, and scattered. The degree to which the sound is

modified depends upon the shear layer strength and downstream development, which in turn depends upon the characteristics of the jet and ambient flows. When the jet is taken from static to flight conditions, changes in the shear layer affect how the sound is refracted, reflected, and scattered. The purpose of this effort is to define a simple correction procedure that accounts for the change in far-field noise levels that results from modifications to the jet shear layer due to ambient flow.

Before describing the theoretical basis and operation of the proposed correction procedure, it is first useful to briefly review the flyover noise prediction process for which flight-corrected engine noise data is required. This will assist in the formulation of an intelligible correction procedure and will demonstrate how the process can be integrated into flyover noise prediction programs such as ANOPP. It is also useful to briefly review shear layer corrections that have been developed for use with acoustic measurements in anechoic wind tunnels, since these results can be adapted for use in the present static-to-flight correction procedure.

3.1.2 Flyover Noise Prediction Process

One of the principal goals in aircraft noise prediction is to determine the noise level heard by an observer during a standard aircraft operation such as takeoff or landing. A metric that is widely used for evaluating the noise received by an observer is the Effective Perceived Noise Level (EPNL). The process of computing the EPNL requires that sound pressure level spectra at a stationary observer position be acquired at half-second intervals over a certain period during the aircraft operation. These half-second increments in reception time correspond to increments in source emission time of varying duration. The sound emitted by the source at time t_e is received by the observer at time t_r given by

$$t_r = t_e + \frac{r(t_e)}{c_0}$$

The distance $r(t_e)$ between the source and observer at the time the sound was emitted divided by the speed of sound c_0 (assumed constant over the propagation path) is simply the time it takes the sound to traverse the source-to-observer distance. In order to predict the noise received by the observer as a function of reception time, it is necessary to predict the sound that is radiated towards the observer as a function of emission time. Thus, it becomes necessary to compute the noise field that is produced by the engines, airframe, and other noise sources on the moving aircraft.

The noise field produced by an engine in motion is most frequently obtained by applying static-to-flight corrections to static engine noise measurements or predictions. It is important to distinguish the coordinates that are used to describe the pressure field in the static and flight cases, and a simple example is useful here. Consider a monopole source in a stationary medium. Sound wave fronts emitted by the source will propagate radially outward and form concentric circles as shown in Figure 30. The far-field pressure is conveniently described in terms of coordinates $(r_m, \bar{\theta}_m)$ relative to the stationary source position (the overbar will be used to denote angles measured relative to the inlet or the direction of motion).

If the source moves with constant velocity through the stationary medium, sound wave fronts will be emitted from different source positions at different times. The sound wave fronts will propagate radially outward from their point of emission, but the motion of the source will result in successive wave fronts being compressed in the direction of motion and dilated in the opposite direction. The sound amplitude along a wave front at an instant of time can be described in terms of coordinates $(r_s, \bar{\theta}_s)$ relative to the position of the source at that instant.

Alternatively, it can be described in terms of coordinates $(r_e, \bar{\theta}_e)$ relative to the position of the source at the time that the sound was emitted. The position of this so-called retarded source is different for each wavefront. A source moving uniformly through a medium can alternatively be viewed as a stationary source immersed in a uniformly moving stream. In this view, wavefronts are emitted from the same physical location but are convected downstream by the flow. It will be assumed that the aircraft is traveling at constant speed and direction with the engines operating at a constant power setting during the time at which the sound is observed.

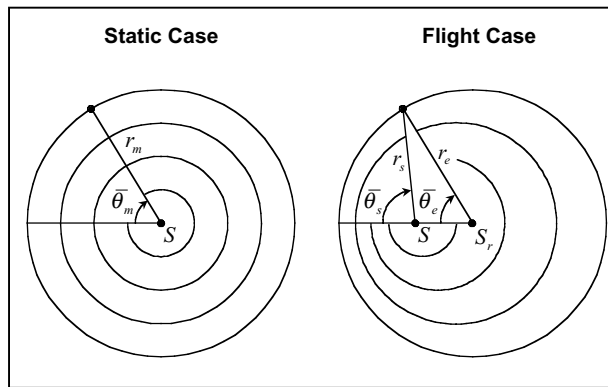


Figure 30. A Description of The In-Flight Sound Pressure Levels Requires a Clear Distinction of the Coordinates System Used.

Thus there are two convenient coordinate reference frames from which to describe the sound field of a moving source. One is a reference frame fixed to the moving source, in which case the sound field appears steady, in the sense that the mean-square pressure is independent of time. The other is a reference frame that is at rest with respect to the fluid or stationary observer, in which case the sound field appears unsteady. Either reference frame may be used to describe the noise field, and the two reference frames can be related using a Galilean transformation on the independent variables.

For the purpose of describing the entire flight-corrected noise field, a reference frame fixed with respect to the source is generally the most convenient due to the time independence. However, for fly-over noise computations, describing the pressure field in terms of retarded source coordinates $(r_e, \bar{\theta}_e)$ is generally more useful. In practice, only the sound amplitude at a single radial distance, i.e. along a single wave front, is required for sources that are steady and in uniform motion. The position of this wave front at a later time is easily determined since the wave front propagates radially outward from the retarded source position. Furthermore, the

amplitude along the wave front at the different position can be simply computed by applying a distance correction based on the inverse square law for acoustic energy and a correction for atmospheric attenuation. The sound received by a distant observer situated at an angle $\bar{\theta}_e$ and radius R_e from the retarded source position is then easily calculated.

3.1.3 Traditional Static-to-Flight Corrections

As a minimum, static-to-flight corrections must account for Doppler shifting of the observed frequency spectra and convective amplification of the sound field. The Doppler frequency shift, which occurs when the source and observer are in relative motion, is a function of the angle between the direction of source motion and the line connecting source and observer. The source frequency f_{source} and the observed frequency $f_{observed}$ are related via

$$f_{observed} = \frac{f_{source}}{1 - M \cos \bar{\theta}_e} \quad (1)$$

M is the Mach number of the source and the emission angle $\bar{\theta}_e$ is the angle between the direction of source motion and the line connecting the retarded source position and the observer.

Convective amplification is also a function of the Mach number M and emission angle $\bar{\theta}_e$, but exact corrections are available only for idealized sources. The intent of the correction is to obtain an estimate of the in-flight mean-square sound pressure $p_f^2(r_e, \bar{\theta}_e)$ given the statically measured or predicted mean-square sound pressure $p_s^2(r_m, \bar{\theta}_m)$. This correction is generally done by multiplying $p_s^2(r_m, \bar{\theta}_m)$ with an angle-dependent flight-correction factor to obtain $p_f^2(r_e, \bar{\theta}_e)$. Usually the measured and retarded distances are chosen to be equal to avoid the need to account for distance or atmospheric absorption corrections at this stage. The flight-corrected levels represent the mean-square sound pressure that would be measured along a wave front described by coordinates $(r_e, \bar{\theta}_e)$ relative to the retarded source position. The convective amplification factor is typically based upon analytical results derived for idealized moving point sources. For these simple sources, the form of the correction factor is dependent upon the source characteristics but is often of the form

$$p_f^2(r_e, \bar{\theta}_e) = \frac{p_s^2(r_e, \bar{\theta}_e)}{(1 - M \cos \bar{\theta}_e)^\alpha} \quad (2)$$

where the angle $\bar{\theta}_e$ is measured relative to the direction of source motion and α is a constant that depends on the source type. Note that $r_m = r_e$ and $\bar{\theta}_m = \bar{\theta}_e$ in this equation. It can be shown that this is the appropriate correction for a monopole source moving at constant speed, in which case

$\alpha=4$ [23] [32]. Because the convective amplification correction factor takes the form of a Doppler factor $(1 - M \cos \bar{\theta}_e)$ raised to some power, the correction is often called a Doppler amplification factor.

Convective amplification factors of this form are often used to correct the spectra of turbomachinery noise sources. However, engine noise is produced by a distribution of source types. To improve the approximation, the measured engine noise data is usually source-separated (or the noise predictions are performed on a component basis) and a correction factor appropriate to each of the contributing source types is used. Correction factors of this type are widely used in correcting static engine noise data to flight conditions. The assumptions made in the process and the appropriateness of these corrections has been investigated in recent articles [21] [22], though a final verdict on their suitability remains open. Although a correction of the form given by Equation (2) is not directly useable as a static-to-flight correction for the exhaust shear layer, significant similarities will be evident.

3.1.4 Shear Layer Corrections

The effects of the shear layer on modifying sound have been widely studied in conjunction with open-jet anechoic wind tunnels, and several correction procedures have been developed to correct data acquired in these facilities. In a typical test, a model noise source (e.g. landing gear, wing flap, scale nozzle, etc.) is immersed in a uniform jet flow to simulate the effects of motion on the radiated noise. Microphones are often placed outside of the jet stream to avoid contaminating the measurements with flow noise. However, sound that propagates from the source to the observer can be refracted, reflected, and scattered by the jet shear layer. In order to obtain an accurate portrayal of the noise field around the moving body, corrections must be applied to measurements made outside the stream to remove the effects of the shear layer. A thorough review of refraction and reflection corrections that have been developed for this purpose is given in reference [20]. Correction equations have been derived for both planar and cylindrical shear layers for the cases where the acoustic wavelength is either large or small compared to the shear layer thickness. The standard correction procedure involves applying an angle correction that accounts for the refraction of sound waves at the shear layer, and an amplitude correction that accounts for the effects of reflection and ray tube divergence. The effects of scattering are often neglected when the frequencies of interest are moderate and the sound is analyzed on a third-octave basis. Additional discussion of analytical and experimental investigations of the shear layer effects can be found in references [18], [19], [34], [36], [37], and [38]. Relevant details of these corrections will be provided in subsequent sections, but what is important for the present discussion is the interpretation of the corrected measurements.

The out-of-stream noise measurements, when corrected for the effects of the shear layer, are representative of the in-stream noise levels. That is, the corrected noise levels are those that would be measured if the jet flow extended past the measurement positions. They can be thought of as the noise levels produced by a stationary source in a moving stream. Equivalently, they can be thought of as the noise levels produced by a moving source in a stationary stream, since the pressure field is independent of the reference frame used. Because the sound is generated when the noise source and surrounding medium are in relative motion, the effects of

convective amplification are already present in the corrected data. Therefore, the corrected data can be used directly in a flyover noise prediction program. The only additional flight adjustment that is required is to Doppler-shift the frequency spectra to account for the relative motion between the moving source and a stationary observer.

In the wind-tunnel case, the tunnel stream is designed to represent motion of the model source through the atmosphere. The shear layer is an undesirable artifact of having to measure outside the flow to obtain data that is uncorrupted by flow noise. The intent of the corrections is to remove the effect of the shear layer altogether. The procedure to correct internally generated engine exhaust noise for static-to-flight shear layer effects entertains a slightly different perspective. In the static-to-flight exhaust noise problem, the shear layer is an integral part of the noise propagation process. Noise generated in the core or bypass flow of the engine must propagate through one or more shear layers as it enters the ambient medium. A shear layer is present whether the engine is in motion or not, except in the unrealistic case where the jet and ambient speeds are identical. In flight, the exhaust shear layer is still present but to a lesser degree than when the engine is static. The intent of a static-to-flight correction procedure in this case is then to account for the *difference in shear layer strength* between the static and flight cases. Note also that, unlike a model noise source in an open-jet wind tunnel, noise measurements on a statically tested engine do not contain any convective amplification effects. Thus, a general static-to-flight procedure for exhaust noise needs to account for the effects of both shear layer alteration and convective amplification. Doppler frequency shifting can be treated separately as is customarily done.

It is worth mentioning that most static-to-flight correction procedures for engine noise do not directly consider the effect of the internal engine flows. Rather, static engine noise sources are treated as if they were stationary point sources. Any effects of the internal flows and exhaust shear layer on the far field sound are concealed within the measurements or the semi-empirical prediction methods. The effect of engine motion is often accounted for by applying convective amplification corrections without consideration of any changes to the internal flows or exhaust shear layer. An enlightening discussion on the influence that these internal flows and jet shear layers have on static-to-flight corrections can be found in reference [21]. These effects can of course be modeled empirically by immersing an engine or nozzle in a tunnel flow. The tunnel stream speed can be varied to simulate flight, and the effects of shear layer changes can be studied directly. Noise levels can be measured outside the tunnel stream and the basic shear layer corrections applied to provide in-stream noise levels representative of an engine or nozzle in flight. An empirical study of this type can be found in reference [31]. Data acquired in such studies can be used to validate the static-to-flight correction procedure described in the next section.

3.2 Static-to-Flight Jet Shear Layer Correction Procedure for Internally Generated Engine Exhaust Noise

3.2.1 Overview

A static-to-flight correction procedure that does account for modifications to the jet shear layer can be developed from existing models. The approach chosen here is a hybrid of corrections developed by Amiet in references [19], [20], and [21] and corrections developed by

Morfey in references [29] and [30]. The procedure relates the in-flight, far field, mean-square sound pressure to the statically measured, far field, mean-square sound pressure as a function of flight speed. The correction process entails applying angle corrections to account for refraction at the shear layer and amplitude corrections to account for ray-tube divergence changes and forward flight effects. The effects of reflection of sound by the shear layer and scattering of sound by shear layer turbulence are ignored. These corrections are developed using a geometric acoustics approach for cylindrical shear layer geometry. The angle correction is based upon a vortex sheet model of the shear layer. The amplitude correction is based on the assumption of energy conservation across the shear layer.

The resulting correction equations are compact and can be conveniently integrated with flyover-noise prediction codes. In the following sections, the model geometry is described and the angle and amplitude corrections are discussed. Various angle relationships that are needed in the procedure are derived. The implementation of the individual corrections into a procedure is described, and sample aircraft flyover noise predictions are presented. The impact of assumptions made in the derivation of the correction equations is reviewed.

3.2.2 Problem Geometry

The model geometry for the correction procedure presented here is shown in Figure 31. An axially symmetric point source S is situated at the exhaust plane on the centerline of a cylindrical jet. A uniform flow of Mach number M_j exists in the jet, which has a constant density ρ_j and constant speed of sound c_j . A shear layer of constant radius h separates the jet from the ambient fluid, which maintains a constant density ρ_a and constant speed of sound c_a . The source S emits sound in all directions. Sound emitted in the wave normal direction ϕ_j is convected by the jet flow. The resulting ray path makes an angle θ_c with respect to the source and intersects the shear layer at the point C . In the static case, the sound is refracted by the shear layer to a wave normal angle ϕ_{as} . The sound propagates through the ambient medium in the wave normal direction ϕ_{as} at speed c_a . The sound arrives at the measurement position M , which lies a distance r_m and angle θ_m from the source. In the flight case, the sound is refracted by the shear layer to a different wavenormal angle ϕ_{af} . The sound propagates through the ambient medium in the wavenormal direction ϕ_{af} at speed c_a , and is also convected by the ambient flow at speed $M_a c_a$. Sound traveling in the upstream direction is considered to re-enter the nozzle and thus does not contribute to the far-field noise.

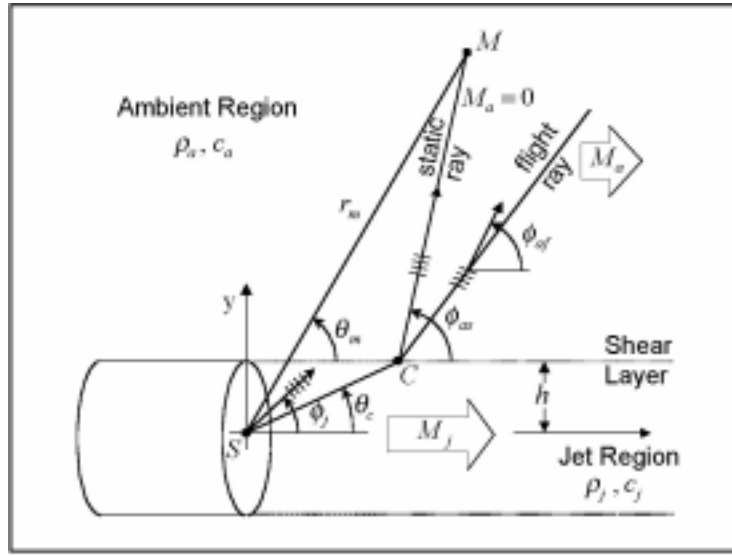


Figure 31. The Static-to-Flight Correction Procedure is Based Upon Cylindrical Model Geometry.

3.2.3 Static-to-Flight Angle Correction

The angle correction is derived by considering the interaction of a two-dimensional plane wave with a plane shear layer, as illustrated in Figure 32. A vortex-sheet model of the shear layer is assumed so that the refraction takes place abruptly at the interface. Sound that crosses a shear layer is refracted due to differences in the speed of sound c and in the flow velocity V on the two sides of the layer. For an infinitely thin shear layer, a relationship between the angle of incidence and the angle of refraction can be simply derived by equating axial phase speeds along the shear layer [32]. The incident wavenormal angle ϕ_j in the jet and refracted wavenormal angle ϕ_a in the ambient medium are related by

$$\frac{c_j}{\cos \phi_j} + V_j = \frac{c_a}{\cos \phi_a} + V_a \quad (3)$$

The wavenormal angle is the angle between the normal to the wavefront and the flow direction. The amount of refraction that takes place at the shear layer is seen to depend upon the conditions on either side of the shear layer.

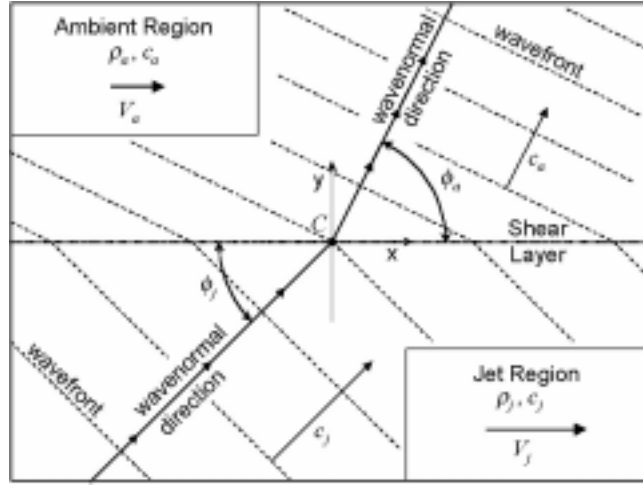


Figure 32. The Refraction Angle Correction is Derived by Considering Plane Wave Interaction With a Vortex Sheet.

Equation (3) can be used to describe how the ambient wavenormal angle is modified when the engine nozzle is taken from static to flight conditions. Using additional subscripts “*s*” and “*f*” to denote the static and flight conditions, and writing the refraction equation for each case yields

$$\text{Static case:} \quad \frac{c_{js}}{\cos \phi_{js}} + V_{js} = \frac{c_{as}}{\cos \phi_{as}} \quad (4)$$

$$\text{Flight case:} \quad \frac{c_{jf}}{\cos \phi_{jf}} + V_{jf} = \frac{c_{af}}{\cos \phi_{af}} + V_{af} \quad (5)$$

It is assumed that the jet velocity remains constant when moving from static to flight conditions, so that $V_{js} = V_{jf} \equiv V_j$. It is also assumed that the temperature in the jet and ambient regions do not change when moving from static to flight conditions, so that $c_{js} = c_{jf} \equiv c_j$ and $c_{as} = c_{af} \equiv c_a$. Finally, it is assumed that the external flow does not affect the generation and propagation of the noise inside the jet. Then the wavenormal angle within the jet is identical in the static and flight cases, so that $\phi_{js} = \phi_{jf}$. Under these assumptions, Equations (4) and (5) can then be combined to provide the following relationship between the ambient wavenormal angles in the static and flight cases:

$$\cos \phi_{af} = \frac{\cos \phi_{as}}{1 - M_a \cos \phi_{as}} \quad (6)$$

where $M_a \equiv M_{af} = V_{af}/c_a$. Equation (6) is the basic static-to-flight angle correction described by Morfey in reference [30]. It relates the ambient wavenormal angle ϕ_{af} in the flight case to the ambient wavenormal angle ϕ_{as} in the static case and the flight Mach number M_a .

3.2.4 Static-to-Flight Amplitude Correction

The amplitude correction is derived from geometric acoustics with the assumption that energy is conserved across the shear layer in a reference frame attached to the jet. The correction applies to high-frequency sound transmission, where the acoustic wavelength of the sound is smaller than the thickness of the shear layer so that reflections off the shear layer can be ignored. Morfey derived an amplitude correction in reference [29] that relates the far-field mean-square pressure outside of a cylindrical shear layer to the mean-square pressure incident upon the shear layer. The relationship between the far-field mean-square pressure $p_a^2(\phi_a)$ outside the shear layer, to the mean-square pressure $p_j^2(\phi_j)$ inside the shear layer is given by

$$r_a^2 p_a^2(\phi_a) = r_j^2 p_j^2(\phi_j) \frac{\rho_a (1 + M_j \cos \phi_j)^4}{\rho_j (1 + M_a \cos \phi_a)^4} \quad (7)$$

The distances r_j and r_a are the wavefront radii in the jet and ambient regions respectively. The angles ϕ_j and ϕ_a are the wavenormal angles in the jet and ambient regions, measured relative to the jet direction. Morfey used this result in reference [30] to derive a static-to-flight correction that relates the amplitudes of the far-field pressure in the static case to the far-field pressure in the flight case. This is done by writing Equation (7) for the static and flight cases and taking the ratio to obtain

$$r_{af}^2 p_{af}^2(\phi_{af}) = \frac{r_{as}^2 p_{as}^2(\phi_{as})}{(1 + M_{af} \cos \phi_{af})^4}$$

The derivation of this result assumes that the jet wavenormal angle and jet Mach number are not affected by the ambient flow. In addition, the density in the jet and ambient regions is assumed to be unchanged by flight. Under these assumptions, the amplitude correction is independent of the jet conditions. The influence of the jet is captured in the angle relationship given by Equation (6).

For the case when the wavefront radii are equal in the static and flight cases, the amplitude relation simplifies to

$$p_{af}^2(\phi_{af}) = \frac{p_{as}^2(\phi_{as})}{(1 + M_{af} \cos \phi_{af})^4} \quad (8)$$

Equation (8) is the amplitude correction that is used in the present correction procedure. It states that the far-field mean-square sound pressure at a flight wave normal angle ϕ_{af} can be calculated by dividing the mean-square sound pressure measured at a static wave normal angle ϕ_{as} by the Doppler factor $(1 + M_{af} \cos \phi_{af})^4$. This equation assumes that the measurements are made in the far field, which is generally the case for static engine noise testing.

Equation (8) has a form reminiscent of the convective amplification correction of Equation (2) when $\alpha = 4$. However, the two equations are not identical. Presuming that the direction of motion is directly opposite the jet flow direction, the two equations can be compared. Writing Equation (2) in terms of an angle $\theta_e = \pi - \bar{\theta}_e$ measured relative to the jet direction gives

$$p_f^2(r_e, \theta_e) = \frac{p_s^2(r_e, \theta_e)}{(1 + M \cos \theta_e)^4}$$

The difference between the correction equations is now apparent. In the traditional convective amplification correction, the flight sound amplitude at θ_e is related to the static sound amplitude at the same wave normal angle θ_e . In the shear layer correction, the flight sound amplitude at ϕ_{af} is related to the static sound amplitude at a different wave normal angle ϕ_{as} . The difference is a result of the ambient flow modifying the refraction through the shear layer.

It is assumed in the above comparison that the direction of motion is opposite to the direction of the exhaust flow. In reality, the engine centerline might not be aligned exactly with the direction of aircraft motion. In this case, the inclination of the engine relative to the direction of motion should be accounted for in the Doppler and convective amplification corrections. This can be done with an appropriate angle substitution, such as $\theta = \pi - \phi + \alpha$ where α is the inclination angle of the engine centerline relative to direction of motion.

3.2.5 Angle Relationships

An attractive feature of the angle and amplitude corrections is that they are straightforward and easily computed. To apply the corrections, the statically measured mean-square pressure must be provided as a function of the ambient wave normal angle ϕ_{as} , measured relative to the jet axis. Far-field static engine noise measurements are usually described in terms of a source-to-observer measurement angle θ_m (usually measured relative to the inlet, but the opposite convention is used here). Thus a relationship between θ_m and ϕ_{as} is needed. As described by Amiet in reference [19], a relationship between the two angles can be easily derived from geometrical considerations. The derivation is provided here since the current case allows for some generalization in that the speed of sound is allowed to differ in the jet and ambient regions.

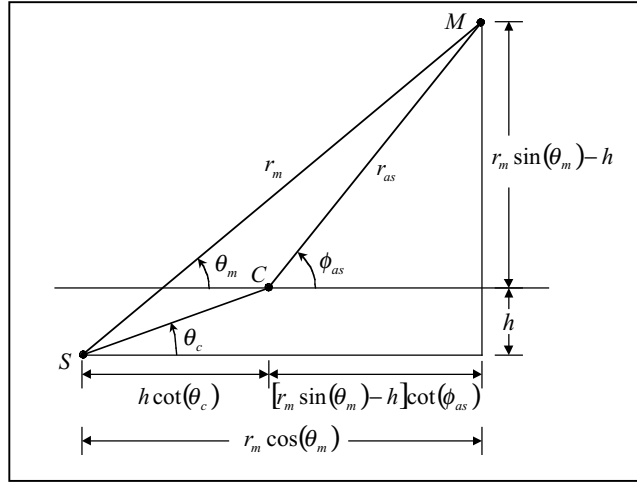


Figure 33. A Relationship Between the Measurement Angle θ_m and Wave Normal Angle ϕ_{as} Can Be Derived From Geometrical Considerations.

Referring to Figure 33, a relationship between the ambient wave normal angle ϕ_{as} , the source-to-observer angle θ_m , and the corrected angle θ_c can be derived from triangle relationships. Relating the length of the bases of the three right triangles in the Figure yields

$$r_m \cos(\theta_m) = h \cot(\theta_c) + [r_m \sin(\theta_m) - h] \cot(\phi_{as}) \quad (9)$$

The wavenormal distance r_{as} over which the sound travels in the ambient region can also be computed from triangle relationships, and is given by

$$r_{as} = \sqrt{(r_m \sin(\theta_m) - h)^2 + ((r_m \sin(\theta_m) - h) \cot(\phi_{as}))^2} \quad (10)$$

Note that the corrected angle θ_c appears in Equation (9) as a parameter. It can be expressed in terms of the ambient wave normal angle ϕ_{as} as follows. First, a relation between the ray path angle θ_c and the jet wave normal angle ϕ_{js} is derived.

Figure 34 shows how ray paths and wave normal angles can be related. A stationary point source S situated on the x-axis is immersed in a uniform flow of subsonic Mach number M . For purposes of illustration, S is a monopole source emitting sound at a single frequency. The constant phase surfaces or wavefronts form circles that are convected downstream by the flow. Sound emitted by the source at a wavenormal angle ϕ propagates radially outward from the source in this direction at the speed of sound c . The sound is also convected downstream by the flow at speed V . Figure 34 displays the wave fronts at successive increments in time. An open circle marks the portion of the wave front that was originally emitted in the ϕ direction by the

source. By definition, the position of the open circles makes an angle ϕ with respect to the retarded source position. Due to convection by the mean flow, these open circles trace out a straight-line path that makes an angle θ_c with respect to the x-axis.

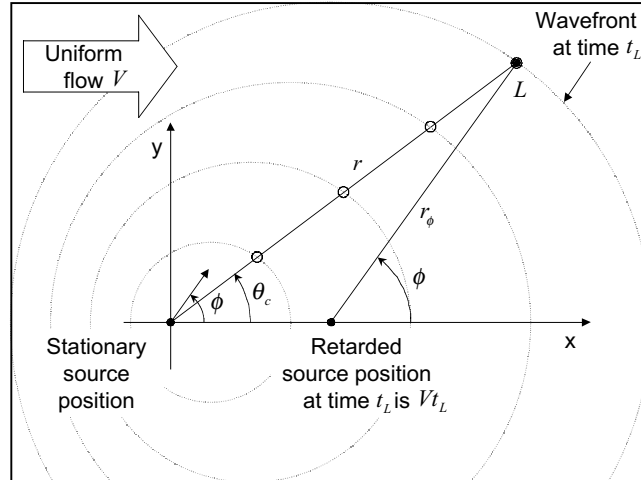


Figure 34. The Ray Path Angle θ_c and the Wavenormal Angle ϕ Are Geometrically Related.

The relationship between θ_c and ϕ is easily determined from geometrical considerations. Figure 35 displays the geometry for a particular time t_L .

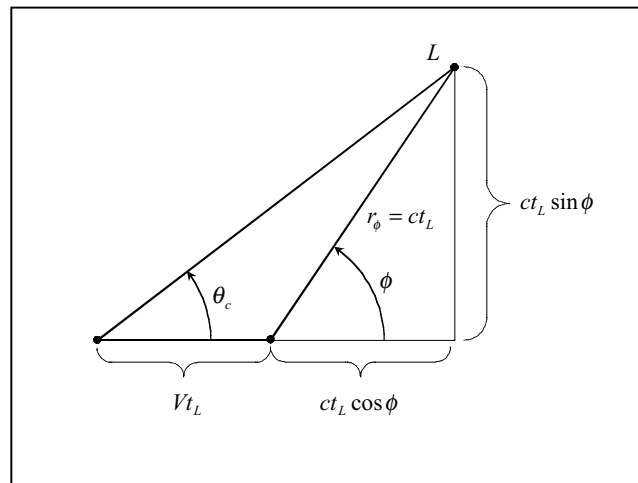


Figure 35. The Relationship Between θ_c and ϕ is Derived From Triangle Relationships.

Considering triangle relationships, θ_c and ϕ are related via:

$$\tan(\theta_c) = \frac{ct_L \sin \phi}{Vt_L + ct_L \cos \phi} = \frac{\sin \phi}{M + \cos \phi}$$

Returning now to the geometry of Figure 33, the relationship between θ_c and ϕ_{js} is

$$\tan(\theta_c) = \frac{\sin \phi_{js}}{M_{js} + \cos \phi_{js}} \quad (11)$$

This relationship can be expressed in terms of the ambient wave normal angle ϕ_{as} using the static angle refraction relation, Equation (4). First note that Equation (4) implies

$$\cos \phi_{js} = \frac{c_j \cos \phi_{as}}{c_a - V_j \cos \phi_{as}} = \frac{\cos \phi_{as}}{\frac{c_a}{c_j} - M_j \cos \phi_{as}}$$

and

$$\sin \phi_{js} = \frac{\sqrt{\left(\frac{c_a}{c_j} - M_j \cos \phi_{as}\right)^2 - \cos^2 \phi_{as}}}{\frac{c_a}{c_j} - M_j \cos \phi_{as}}$$

Substituting into Equation (11) produces the desired relationship between θ_c and ϕ_{as}

$$\tan(\theta_c) = \frac{\sqrt{\left(\frac{c_a}{c_j} - M_j \cos \phi_{as}\right)^2 - \cos^2 \phi_{as}}}{\frac{c_a}{c_j} M_j + (1 - M_j^2) \cos \phi_{as}} \quad (12)$$

This reduces to Equation (1) of Reference [20] when the temperatures of the jet and ambient regions are the identical. Thus, given θ_m , r_m , h and M_j , the static ambient wave normal angle ϕ_{as} can be determined using Equation (9) and (12).

3.2.6 Implementation of the Corrections

An exhaust shear layer static-to-flight correction procedure can now be described. Static engine noise measurements are obtained at far-field coordinates (θ_m, r_m) relative to the source position, with θ_m measured relative to the exhaust centerline. At a given measurement location,

Equations (9) and (12) are used to calculate the corresponding static ambient wave normal angle ϕ_{as} . The statically measured mean-square pressure $p_m^2(\theta_m, r_m)$ can then be re-identified as $p_{as}^2(\phi_{as}, r_{as})$, where the wave normal coordinates (ϕ_{as}, r_{as}) are measured relative to the shear layer intersection point C . Next, the flight ambient wave normal angle ϕ_{af} is computed using Equation (6). Finally, the flight-corrected mean-square pressure $p_{af}^2(\phi_{af}, r_{af})$ at an equal wave normal distance $r_{af} = r_{as}$ from the point C can be computed using Equation (8).

When used in a fly-over-noise prediction program, the flight-corrected mean-square pressure typically needs to be expressed in terms of coordinates relative to the retarded source position. Furthermore, flight-corrected data is usually desired at the same angular positions and same distance from the retarded source position as were used during static measurements. Therefore, an interpolation to coordinates relative to the retarded source position is required. It is here that the correction procedure runs into some difficulty, and a sample result serves to illustrate the problem.

Figure 36 displays results that are typical of this simplified model. A point source is located at the origin of a cylindrical jet of radius 1 and Mach number 0.5. Measurements are made at 10-degree increments about the source position at a radius equal to 10 (the measurement radius does not classify as a far-field distance but was chosen so that the ray paths in the jet were visible). Red solid lines connect the source with the measurement positions. The sound does not travel directly along the red lines however.

In the static case, the sound propagates to the measurement positions along the dashed blue lines. Inside the jet, the blue ray path makes an angle θ_c with respect to the jet centerline. Upon reaching the shear layer at point C , the sound is refracted to a wave normal angle ϕ_{as} . The sound propagates in this direction to the observer. To observers on the forward arc, the sound appears to emanate from a localized region on the shear layer just above the source. To observers along the aft measurement arc, the sound appears to emanate from a distributed source region along the shear layer surface.

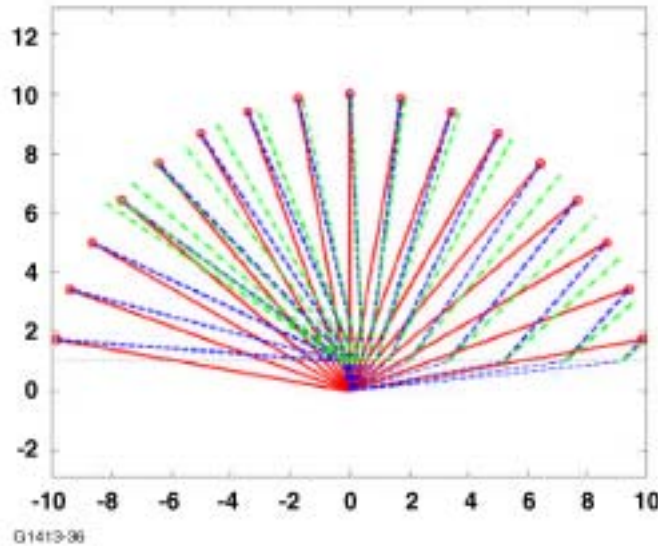


Figure 36. Sample Refraction Results From the Simplified Model for $M_j = 0.5$, $M_a = 0.2$, and $c_j = c_a$.

In the flight case, the propagation within the jet remains unchanged (by assumption). However, the mean flow alters the refraction at the shear layer interface. For an ambient Mach number of 0.2, the sound waves are refracted in the direction of the green dotted-dashed lines, which make an angle ϕ_{af} with respect to the downstream direction. The angular change is quite pronounced in the upstream direction, and relatively modest in the aft arc.

The set of shear layer intersection points $\{C_i\}$ can be thought of as a collection of retarded sources, each of which radiates sound in only one direction. If the jet is imagined to move to the left with the flight velocity, then the sound will propagate from each of these points along the green dotted-dashed lines to a distant observer. Note also that sound emitted when the source is at the origin will take a different amount of time to reach the shear layer, so the sound is not emitted from each of the intersection points simultaneously.

It must be noted that the propagation within the jet at these extreme angles is unrealistic, as no account has been made of the mixing of the jet with the ambient flow. Nevertheless, the difficulty with this simplified model is that the source is somewhat smeared out in space and time. This source non-compactness makes it difficult to implement a shear layer correction procedure in a rigorous way for the aft angles. Since many fly-over noise programs lack the capability to model distributed sources, some further simplification is needed. The approximation (commensurate with other approximations made within fly-over noise programs) introduced here is to consider that the effect of the shear layer is mainly to alter the direction of wave normal propagation of the sound. In this simplification, the points $\{C_i\}$ are all forced to be coincident with the retarded source position. Pictorially, this causes the blue lines to collapse onto the red lines. The green lines are simply offset from the merged blue-red lines by an amount equal to the difference between static and flight ambient wave normal angles, as shown in Figure 37.

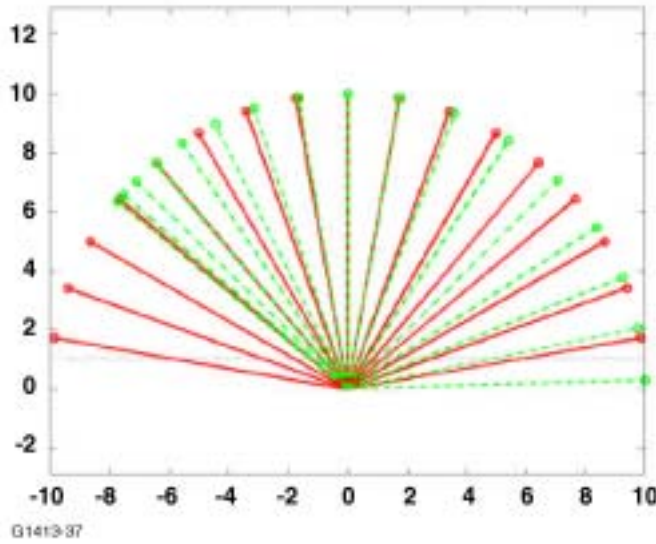


Figure 37. Collapsing the Shear Layer Intersection Points Onto the Origin Allows for Simplifications to the Correction Procedure.

With this simplification, the effect of refraction changes due to flight is to simply shift the directivity by an amount equal to the difference between the static and flight ambient wave normal angles. That is, in flight, sound will be emitted from the source in a direction Φ_f given by

$$\Phi_f = \theta_m - (\phi_{as} - \phi_{af}) \quad (13)$$

The mean-square pressure in this direction at a wave normal distance (i.e., distance from the retarded source position) equal to r_m is still provided by Equation (8) but written using the variable Φ_f ,

$$p_f^2(\Phi_f, r_m) = \frac{p_m^2(\theta_m, r_m)}{(1 + M_f \cos \Phi_f)^4} \quad (14)$$

The values of p_f^2 at the original angles θ_m can be obtained by interpolation. The accuracy of these approximations improves when $r_m \sin \theta_m \gg h$. Referring to Figure 38, as $h/(r_m \sin \theta_m) \rightarrow 0$ with $\overline{CF} = \overline{CM} = r_{as}$, then $\angle FSM \rightarrow \angle FCM = \phi_{af} - \phi_{as}$ and $r_f \rightarrow r_m$. So for distant sideline observers, as is the case in fly-over noise studies, the approximation becomes quite acceptable.

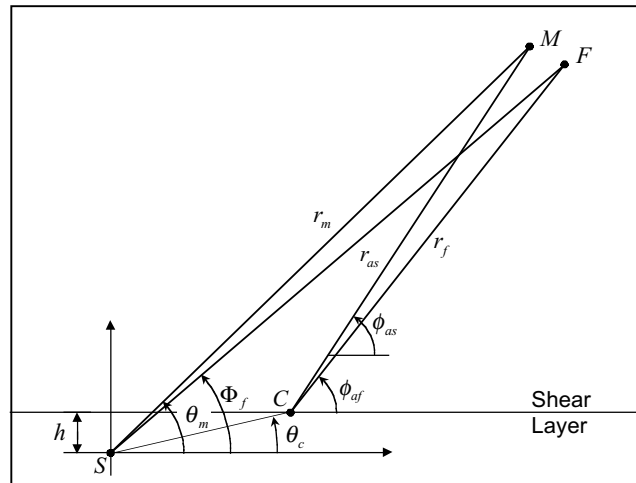


Figure 38. The Approximation Improves as the Sideline Distance From the Shear Layer Increases.

Some additional comments are worth mentioning regarding special treatment at the extreme angles. Consider the upstream direction of the current sample problem. In the static case, sound that propagates within the jet at wave normal angles greater than 131.8 degrees is internally reflected. In the flight case, sound that propagates at jet wave normal angles greater than 141.3 degrees is internally reflected. Thus, sound that propagates at wave normal angles in between 131.8 and 141.3 degrees will theoretically escape to the free stream in the flight case. The sound level corresponding to these jet wave normal angles is indeterminable from static measurements that are made outside the jet. Thus, some approximation must be made in the forward arc beyond this limiting angle. In the current model, sound is not expected to radiate from the nozzle at these upstream angles anyway, so this effect is unimportant.

Consider now the effects in the downstream direction. In the static case, no sound leaves the jet at wave normal angles less than 48.2 degrees. In the flight case, no sound leaves the jet at wave normal angles less than 39.7 degrees. These regions are the so-called zones of silence. However, it does not imply that sound cannot be measured at an observer angle less than the zone of silence angle, because the sound can propagate down the jet before escaping to the ambient region. It is worth mentioning that these shallow angles are typically not important in the open jet wind tunnel scenario, because the jet wave normal angles corresponding to these downstream angles are quite small. In the current example, for the measurement angle of 40 degrees, the jet wave normal angle in the jet is only 25 degrees, and noise radiated at such a shallow angle is not a contributor to fly-over noise levels.

3.2.7 Summary of the Static-to-Flight Correction Process

The simplified jet shear layer static-to-flight correction procedure for internally generated engine exhaust noise can be summarized in the following steps:

1. Measure or predict the static mean-square pressure $p_m^2(r_m, \theta_m)$ of the internally generated engine exhaust noise at a fixed radius r_m and at various angles θ_m from the source. Source-separation techniques may be required.
2. For a given measurement angle θ_m , compute the static ambient wave normal angle ϕ_{as} using Equations (4), (9), & (11). An iterative procedure must be used, since ϕ_{as} cannot be expressed explicitly in terms of θ_m .
3. Compute the flight ambient wave normal angle ϕ_{af} using Equation (6).
4. Compute the approximate flight emission angle Φ_f using Equation (13).
5. Compute the flight-corrected mean-square pressure $p_f^2(\Phi_f, r_m)$ using Equation (14).
6. Interpolate the flight-corrected mean-square pressure $p_f^2(\Phi_f, r_m)$ back to the original measurement angles θ_m , if desired.

3.2.8 Computer Program

A FORTRAN computer program to compute the jet shear layer static-to-flight corrections was developed. The program follows the sequence of steps described in the previous section. The first three steps are performed in subroutine REFRACT. The last three steps are performed in the component noise routines. Details of the implementation can be found in the comments within the code.

The subroutine REFRACT requires the inputs listed in Table 5. The inputs are usually available from engine and aircraft performance data. They include the measurement radius and measurement angles (relative to the jet centerline) and the conditions of the jet and ambient flow.

Table 5. The Following Inputs Are Supplied to Subroutine REFRACT.

Variable	Description	Units
NM	Number of measurement positions	
RM	Measurement radius	Ft
THETAM	Measurement angles relative to the jet axis (array)	Degrees
RJET	Jet radius	Ft
VJ	Jet velocity	ft/sec
TJ	Jet temperature	°F
VA	Ambient flight velocity	ft/sec
TA	Ambient temperature	°F

Table 6. The Following Outputs Are Returned by Subroutine REFRACT.

Variable	Description	Units
PHIAS	Ambient wavenormal angle for the static case	Degrees
PHIAF	Ambient wavenormal angle for the flight case	Degrees

3.2.9 Sample Application of the Procedure

The static-to-flight correction procedure described herein has been used to flyover noise predictions for a generic business jet. Static engine noise data, measured along a 100-ft arc in 10 degree increments, was source separated into narrowband, broadband, and jet noise components. Predictions of the aircraft flyover noise were made with and without the shear layer corrections applied to the internally generated engine exhaust noise. For the purposes of this example, the internally generated engine exhaust noise was considered to consist of narrowband and broadband noise measured at angles of 90 degrees and lower relative to the jet centerline. Noise at angles greater than 90 degrees from the jet centerline were assumed to radiate from the inlet.

Predictions were made for approach, cutback-takeoff, and sideline according to standard FAR 36 procedures [25][26]. The differences in Effective Perceived Noise Levels, displayed in Table 7, are seen to be quite modest. The differences would be more substantial for cases where the exhaust noise exhibits more pronounced directivity lobes.

Table 7. Differences in Effective Perceived Noise Levels Between Predictions Made With and Without Shear Layer Corrections Are Relatively Modest.

	Approach	Cutback-Takeoff	Sideline
Δ EPNL	0.0	0.1	0.3

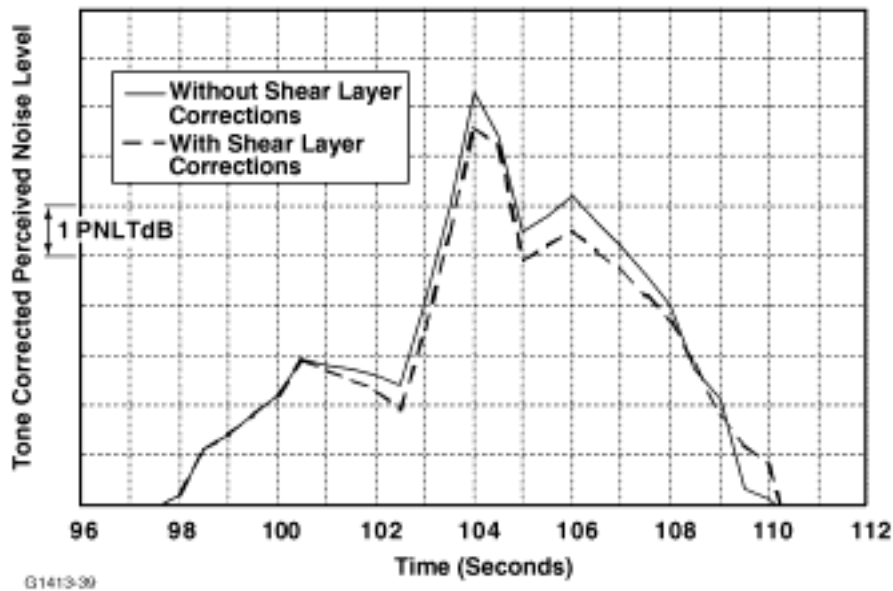


Figure 39. Small Changes Are Evident Flyover Noise Time History for the Cutback Takeoff Conditions.

3.2.10 Limitations of the Method

Numerous assumptions are associated with the correction procedure described here, many of which are tied to the geometric acoustic approach that is used. The angle correction assumes

the observer to be in the geometric far field of the source, so that the observed sound originates from only a single location. The angle correction also assumes an infinitely thin shear layer. This does not appear to be a substantial limitation, as numerical ray-tracing solutions using Lilley's equation [20] suggest that incorporation of thickness does not significantly affect the angle correction. The amplitude correction assumes that the observer is in the acoustic far field of the source, and is strictly applicable only to high frequency noise, since the shear layer was assumed to be non-reflective. The effects of reflection can be incorporated in an approximate way by using analytical results for low-frequency plane wave reflection. However, analytical investigations [20] have shown that the effects are only substantial at the extreme angles. If improved accuracy is needed, then the effects of multiple reflections must be addressed. Unfortunately, modeling multiple reflections requires detailed knowledge of the source characteristics, and this is usually unavailable.

The effects of scattering by shear layer turbulence have been ignored in this model. Scattering can modify the transmitted sound most notably in two ways. One effect is spectral broadening of discrete tones, and the other is reflection or absorption of the sound. Experimental investigations [37] suggest that while spectral broadening is important for narrowband analyses, sound analyzed on a third-octave basis is not significantly impacted. Scattering and absorption of sound does not have a significant impact on the third-octave noise levels except at extreme angles and high frequencies.

Many of the difficulties with the model are due to the model's simplicity. Closed form analytical solutions are obtained at the expense of unrealistic non-mixing mean flows. More sophisticated modeling of the jet flow and shear layer would be necessary to more accurately account for propagation paths. The shear layer and mixing region could be modeled with analytical approximations, but the ray paths would have to be solved for numerically and even this approach suffers from the same limitations of geometrical acoustics. More sophisticated modeling of the distribution and composition of the noise sources would be needed to account for reflections by the shear layer and for source non-compactness effects. This information is usually unavailable in engine testing. Despite its limitations, the present method does provide an expedient first-order indication of shear layer static-to-flight effects.

3.3 Implementation in the NASA Aircraft Noise Prediction Program (ANOPP)

The shear layer correction analysis has been implemented for ANOPP. Appendix II provides the Theoretical Manual Documentation and Appendix III provides the Users Manual Documentation. The code will be made available through ANOPP standard distribution procedures controlled by NASA Langley Research Center.

3.4 List of Symbols

$\theta_e, \bar{\theta}_e$ Angle between retarded source position and "measurement" position in the flight case
 $\theta_m, \bar{\theta}_m$ Angle between source position and the measurement observer in the static case
 θ_c Angle of acoustic ray propagation in the jet region
 $\phi_j, \phi_{js}, \phi_{jf}$ Wave normal angle in the jet region - general case, static case, flight case
 $\phi_a, \phi_{as}, \phi_{af}$ Wave normal angle in the ambient region - general case, static case, flight case

- h Distance between source and shear layer, assumed equal to nozzle radius
- r_{af} Wave normal radius in the ambient region for the flight case
- r_{as} Wave normal radius in the ambient region for the static case
- r_e Distance between retarded source position and “measurement” position in the flight case
- r_m Distance between source and measurement position in the static case
- V_j, V_{js}, V_{jf} Velocity of the uniform flow in the jet region - general case, static case, flight case
- V_a, V_{as}, V_{af} Velocity of the uniform flow in the ambient region - general case, static case, flight case
- M_j Mach number in the jet region
- M_a Mach number in the ambient region
- ρ_j Fluid density in the jet region
- ρ_a Fluid density in the ambient region
- c_j, c_{js}, c_{jf} Speed of sound in the jet region - general case, static case, flight case
- c_a, c_{as}, c_{af} Speed of sound in the ambient region - general case, static case, flight case

Note: Angles with overbars are measured relative to the inlet direction or direction of source motion. Angles without overbars are measured relative to the jet axis.

4. ENGINE SOURCE NOISE CHANGES WITH ALTITUDE STUDY

4.1 Modeling Approach

The initial approach for modeling engine source noise changes with altitude was to generate engine cycle data for the 1992 Baseline Technology Business Jet, at altitudes from sea level to 15,000 feet, at appropriate thrust and velocity conditions. For each of these cycle points, an engine source noise prediction would be performed, using the methods of the ANOPP program, as a level flyover at the altitude of the cycle point. The resulting noise prediction would then be included as an element in the Noise-Power-Distance (NPD) table of the Integrated Noise Model (INM) program, where “distance” was assumed to be altitude. Thus, the INM NPD table would be populated with essentially “Noise-Power-Altitude” data.

This modeling approach was not workable, however, due to the fact that for exposure-based noise level metrics (SEL, EPNL, etc.) INM treats the “distance” in the NPD table as a slant distance, rather than an altitude. INM calculates the EPNL at each observer point using the power associated with each flight segment and the distance from the observer to the flight segment (the slant range). The problem arises when the calculated slant range is e.g., 16,000 ft., but the flight segment has an altitude of only 500 ft. (i.e., the observer point is far from the flight segment). The EPNL value that INM will extract from the NPD table will be based on the correct power level, but an altitude of 16,000 ft. rather than 500 ft.

To “force” the INM program to access the proper predicted noise levels from the NPD table (i.e. the EPNL representing the correct altitude effects on engine source noise), the thrust levels in the INM flight profiles were modified slightly. This modification ensured that a unique thrust

level is associated with each altitude. Cycle sheets for each altitude/thrust level combination were generated, and noise predictions were obtained for level fly over altitudes which will represent the slant range “distances” in the INM NPD table. This technique ensured that the correct altitude is accessed (via a unique thrust level), no matter what slant range is appropriate at a particular observer point in the INM analysis. Therefore, the altitude effects for the source noise were modeled properly.

4.2 Differences Between INM Versions 5.2a and 6.0.

Differences between calculated computer contours between INM v5.2a and v6.0 were discovered. The same INM input that was used for the 1992 Baseline study using INM v5.2a was used in INM v6.0 and generated a 70 EPNL contour that was about 2 square miles smaller than the v5.2a 70 EPNL contour. It was decided that v5.2a will be used to fulfil the requirements of this study and be consistent with the 1992 baseline business aircraft study. Performance calculations were made at each of the flight profile altitude, thrust, and velocity settings. Corresponding input decks have been developed for the level flyover EPNL computations. The noise-power-distance curves were generated based on these EPNL level flyover values and used in INM v5.2a for comparison.

4.3 Analysis Results

Engine performance parameters required to predict engine noise from sea level to 15,000 feet altitude were obtained based on a takeoff and landing flight profile consistent with the 1992 technology baseline business jet. Using this engine performance data, altitude-related changes in engine source noise and airframe noise were predicted for a number of level flyover conditions, using the internally developed General Aviation Synthesis Program (GASP). The resulting new source noise characteristics with altitude were then input into the Federal Aviation Administration (FAA) Integrated Noise Model (INM) program to compute changes in the Sound Exposure Level contours due to the new source noise characteristics. To ensure a consistent comparison, the 1992 Baseline INM Results were re-defined to incorporate the new (longer) flight profile of the present study.

The results from this study are summarized in Table 8 corresponding to the EPNL contour data contained in Figure 40 and Figure 41. These results illustrate significant differences in the lower EPNL contours.

Table 8. Summary of Altitude Effects on EPNL Contours.

Square Miles	65 EPNL	70 EPNL	75 EPNL	80 EPNL	85 EPNL	90 EPNL
1992 Baseline	113.71	45.39	15.38	6.63	2.86	1.22
Task 33	143.63	56.70	17.27	7.30	3.16	1.32

“Case Echo Reports” from INM version 5.2a are provided in Appendix IV and Appendix V for the baseline and the new altitude effects, respectively. These reports summarize the input (aircraft type, airport information, runways, flight profiles, npd curves, etc.) that went into the computation of the EPNL contours illustrated in Figure 40 and Figure 41. The approach and departure flight segments tabulated in these case echo reports can be seen in Figure 42 and

Figure 43, respectively. These segments made up the flight profile utilized in the present study consisting of approach from 15,000 ft. and departure to 15,000 ft.

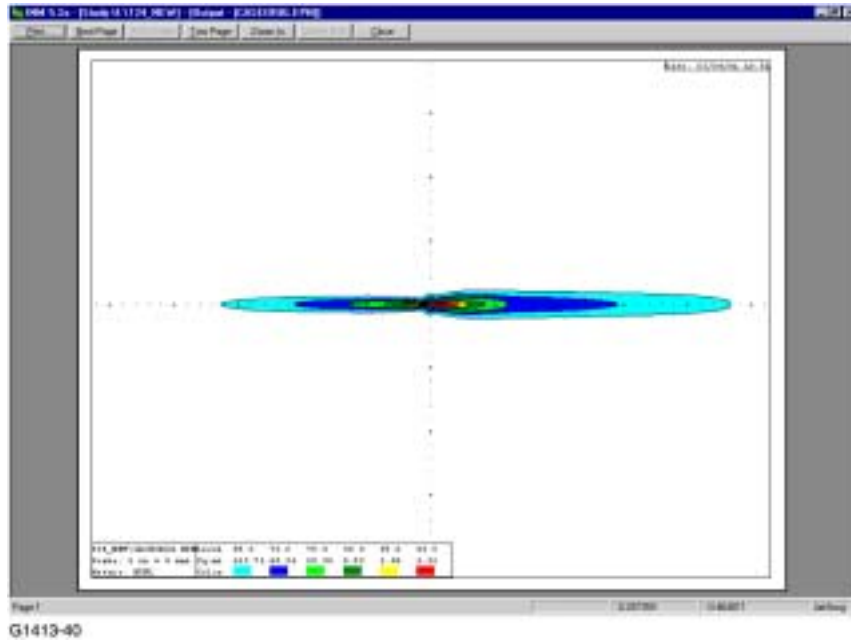


Figure 40. EPNL Contour of Baseline 1992 Results With New Flight Profile.

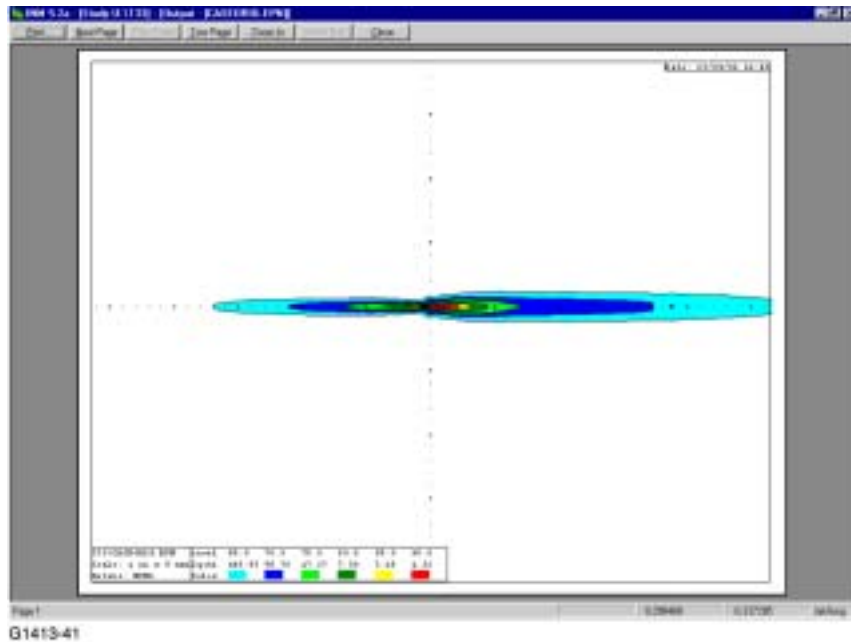


Figure 41. EPNL Contour of New Noise/Altitude Results.

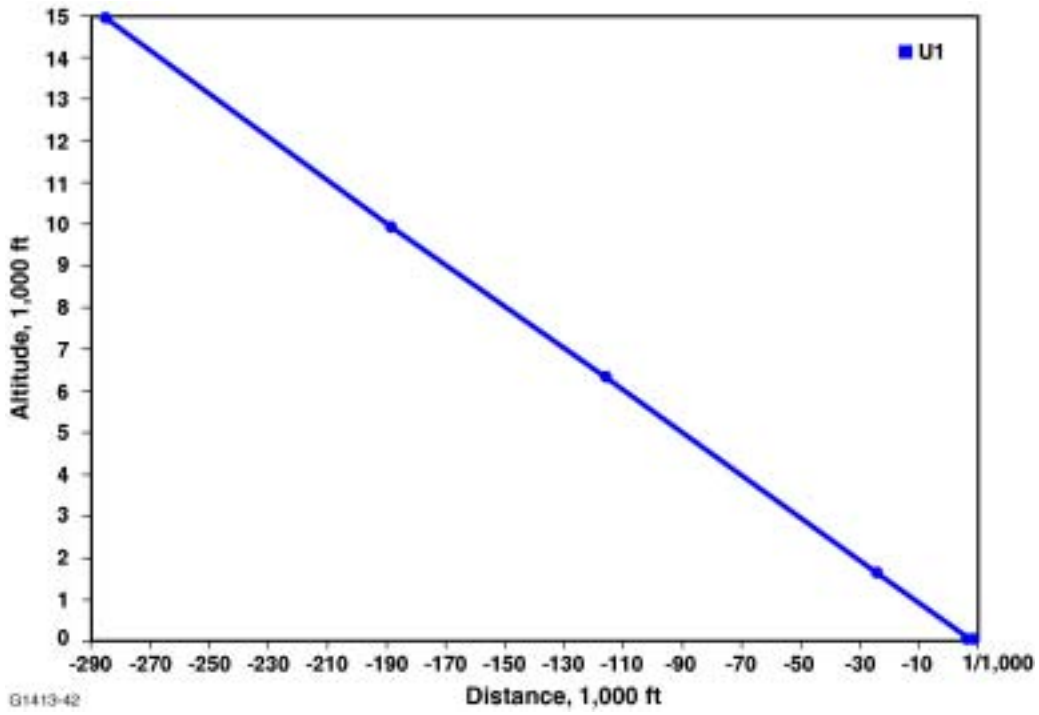


Figure 42. Approach Flight Segment.

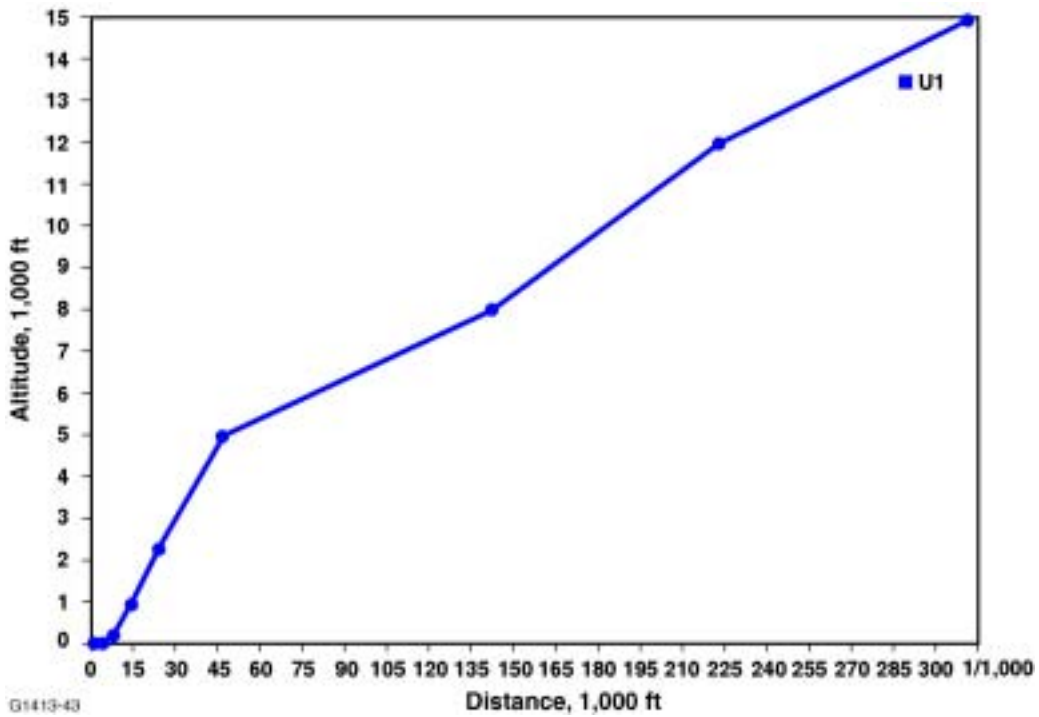


Figure 43. Departure Flight Segment.

The noise (EPNL) power (lbs. thrust) distance (ft.) curves from the 1992-baseline result and the present noise/altitude study are illustrated in Figure 44 and Figure 45, respectively. These figures are also tabulated in Appendix IV and Appendix V respectively. A reasonably good example of where the differences in the contour results might be attributed is illustrated by comparing the NPD results shown in Figure 44 and Figure 45 at the 15000-ft distance for the 2166 lbs. and 2194 lbs. thrust curves, respectively. The EPNL levels differ by about 5 dB. This 5 dB EPNL difference would primarily influence the observer location directly below this flight segment, which is one part of the overall flight path that contributes to the total EPNL at that observer location. It is assumed that this sited EPNL difference can be attributed to the velocity and altitude differences in engine performance that are indirectly contained in the NPD tables.

It should be noted that the NPD data in Figure 44 and Appendix IV slightly differs from that reported in the 1992-baseline study. The following modifications were made to generate the new baseline data contained in this report:

- (a) As mentioned, GASP was modified to include significantly more 1/2 second intervals.
- (b) The referred mass flow entering the fan was used vice the physical (per the new GASP modifications).
- (c) All EPNL output from GASP is referenced to 160 knots to appropriately accommodate the airspeed adjustment routine in INM.

Combined these modifications only slightly changed the baseline results compared to the data present in the May 31, 1995 Final Report 21-8867 titled, "Definition Of 1992 Technology Noise Levels For Business Jet Aircraft And The Methodology For Assessing Airplane Noise Impact Of Component Noise Reduction Concepts".

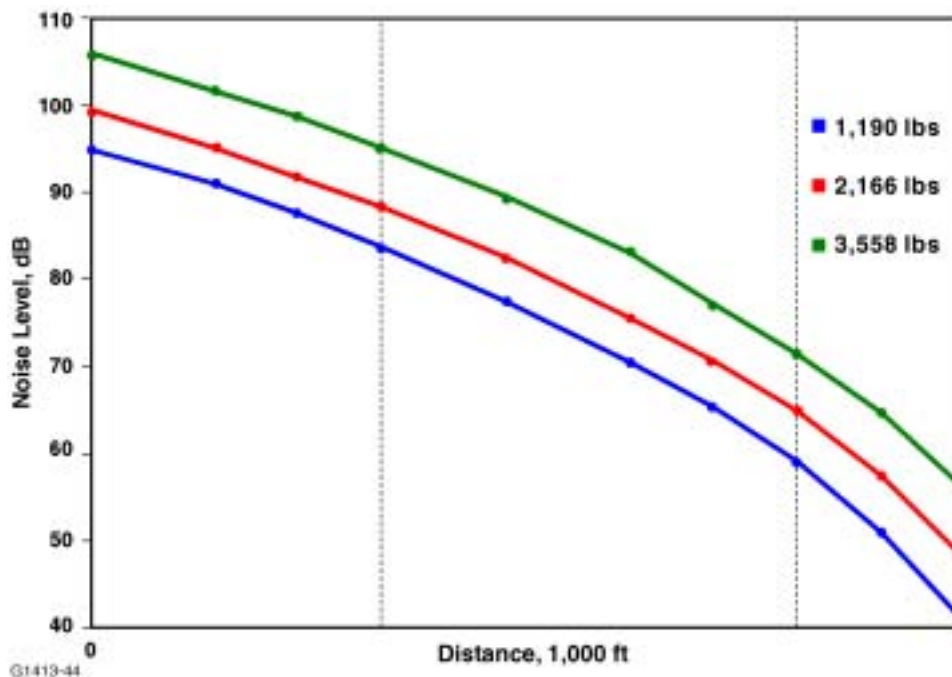


Figure 44. Noise Power Distance Curves From 1992 Baseline.

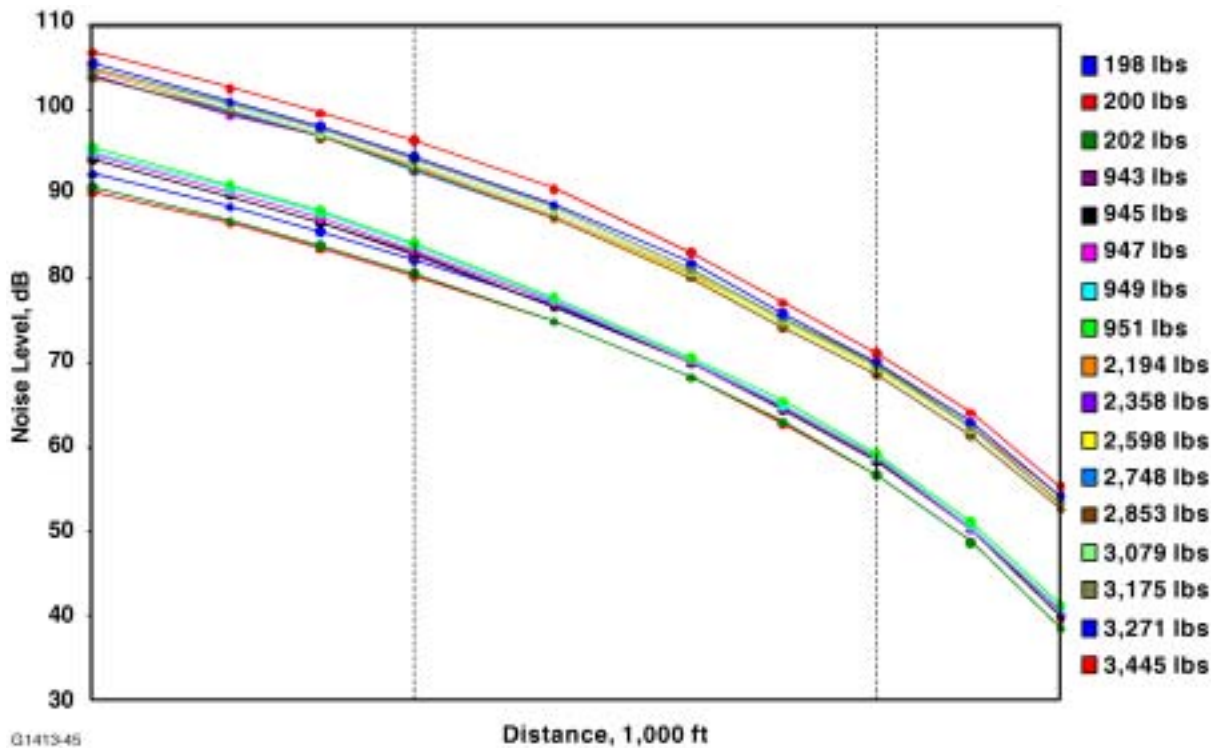


Figure 45. Noise Power Distance Curves for Noise/Altitude Study.

5. LATERAL ATTENUATION EXPERIMENTS

5.1 Introduction

Noise predictions in the FAA Integrated Noise Model for aircraft at elevation angles less than 60 degrees currently use an empirical algorithm which combines all known lateral attenuation effects (ground attenuation, atmospheric effects, installation effects). The objective is to replace this single empirical algorithm with component, scientifically defensible models. The approach is to conduct a controlled flight test to isolate installation effects.

This objective was accomplished by flying a variety of aircraft with different engine and installation configurations over an array of microphones. The flybys simulated aircraft departures and approaches. The microphone array consisted of one line of microphones on thirty foot, guyed poles spaced across the runway and two lines of microphones suspended vertically as high as 200 ft. from cranes located at a distance of 425 ft. to each side of the runway. The acoustic signals recorded from these aircraft flybys of the microphone array were correlated with aircraft position, aircraft engine and aircraft state parameters, and locally measured weather parameters. The resulting database of correlated acoustics information was analyzed to isolate and quantify the lateral attenuation patterns of the different engine and installation configurations.

Level flights at 200-600 feet above ground level with 20 microphones, position data, and weather data were conducted. A schematic diagram of the microphone layout is shown in Figure 46.

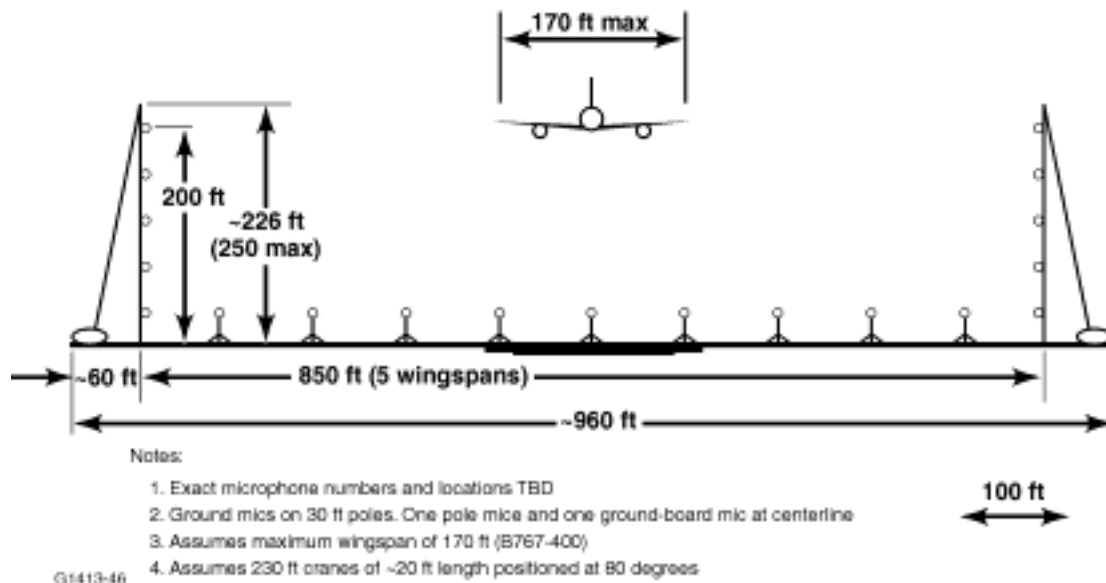


Figure 46. Diagram of Microphone Layout for the Lateral Attenuation Experiments at Wallops Island, VA.

The Volpe Center’s video system was the method for position data collection for some of the aircraft included in the study. The video camera tracking system consists of two Canon Optura digital video cameras and four reference optical targets, all deployed at known, fixed locations within the site’s local coordinate system. Traditional surveying equipment was used to determine the relative heights of the digital video cameras and targets used for aircraft tracking. Post-processing of the digital video data using classic triangulation techniques determined accurate time and position information for each aircraft event.

Two types of meteorological data were collected during the measurement study: (1) ground-based meteorological data and (2) meteorological data aloft. For the ground-based meteorological data, Qualimetrics Transportable Automated Meteorological Stations (TAMS) was set up at two locations. The TAMS recorded temperature, relative humidity, wind speed and direction, and ambient atmospheric pressure at one-second intervals.

In addition to ground-based data, meteorological data aloft was measured and recorded using a LaRC tethered weather balloon system. The balloon was deployed to a maximum height of 700 ft. for readings each day prior to beginning test flight runs, after completion of test flight runs, and at approximately two hour intervals during the test flight runs. The balloon was located approximately 700 ft. from the runway centerline. The tethered weather balloon system consisted of an electric winch-controlled, tethered, helium-filled balloon, an instrument/telemetry pod, a ground-based receiver/data-controller, and a ground-based support computer.

Additional balloon weather data was obtained from the Wallops MET OPS group. Normally, MET OPS launches a meteorological balloon at 0700 and 1900 daily. These launches were augmented with a third launch at approximately noon, at the end of the measurements for each day. As with the ground-based sensors, the balloon-based sensors were setup to measure and record temperature, relative humidity, wind speed and direction, and ambient atmospheric pressure.

5.2 Honeywell Participation

Honeywell identified two aircraft to participate in the Lateral Attenuation Experiments at Wallops Island VA.

The Falcon 900EX is a 3 aft-mounted engine aircraft powered by TFE731-60 engines (BPR = 4.3 at take-off). The aircraft has an 18.4 EPNdB cumulative margin to Stage 3. The TFE731-60 is the engine used in all of the Honeywell engine validation work for AST Noise Reduction. The aircraft arrived at Wallops Island on September 26, 2000. A picture of the aircraft is shown in Figure 47. Unfortunately, weather conditions prohibited data collection, and there was no day available for a rescheduled test.



Figure 47. The Honeywell Falcon 900EX, Waiting for the Winds to Calm and the Ceiling to Rise.

The Falcon 2000 is a 2 aft-mounted engine aircraft powered by CFE738-1 engines (BPR = 6.2 at take-off). The aircraft has a 22.1 EPNdB cumulative margin to Stage 3. Honeywell and GE jointly produce the CFE738-1 engine. The aircraft arrived on the morning of September 27, 2000 to excellent weather. All elements of the test matrix were completed. Figure 48 shows the Falcon 2000 at Wallops and Figure 49 shows the Falcon 2000 flying over (and through) the microphone array.

Static data and engine information exists for the CFE738 engine that can be used to aid in interpreting the results of the measurements.



G1413-48

Figure 48. The Honeywell Falcon 2000 Arrived to an Almost Perfect Sky and No Winds on the Next Day.



G1413-49

Figure 49. The Falcon 2000 Flying Through the Microphone Cranes at Wallops Island.

5.3 Data Analysis

Performance data for the Falcon 2000 flight conditions was obtained. The calculated net thrust for an average CFE738 engine, installed, at the following conditions (relative hum = 60%) is:

N1C	IAS	Tamb	Pamb	Net Thrust
80.5%	190 kt	60 F	1019 mb	4204 lb
60.0%	200 kt	60 F	1019 mb	1637 lb
48.0%	198 kt	60 F	1019 mb	824 lb
38.0%	195 kt	60 F	1019 mb	374 lb

The parameters are based on the average conditions for each of the four power settings used in the test.

The Falcon 2000 acoustic data received from NASA Langley was reformatted into Honeywell acoustic database files. Static engine noise data was identified for the CFE738 that correspond to three of the conditions tested at Wallops Island. A component separation of the static data was performed to project the data to the flight conditions. Figure 50 shows a comparison of the measured fly-over data for the 82% N1 cases at the 400-ft fly-over condition for the flush mounted overhead microphone. It can be seen that the fly-over results agree well with the measured data.

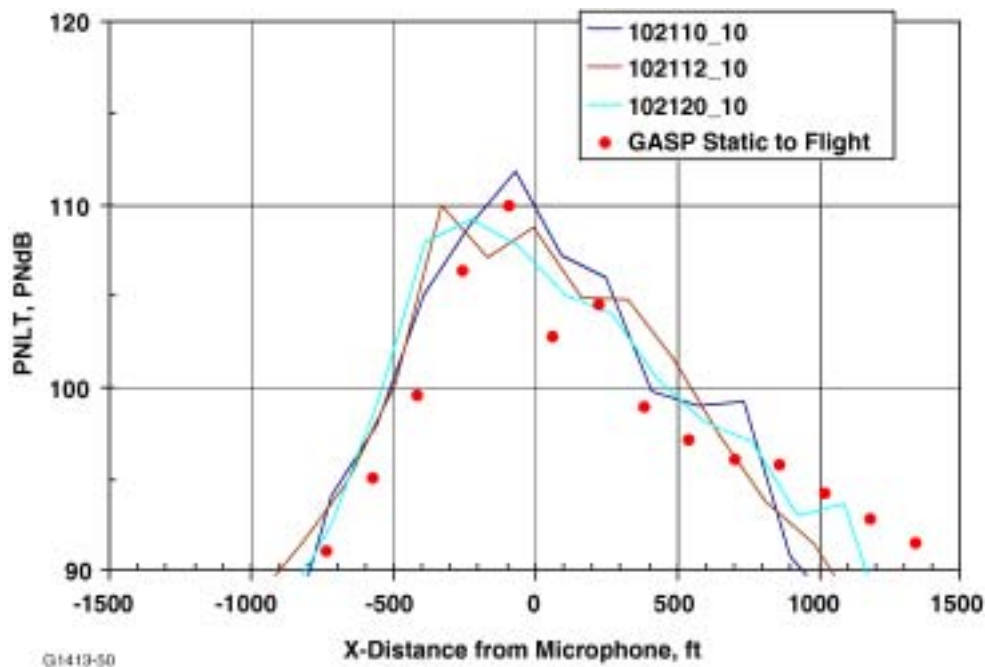


Figure 50. The Measured and Projected Tone-Corrected Perceived Noise Level Time Histories Agree Well for the Falcon 2000 at the Takeoff Power Condition (82% N1) at Overhead.

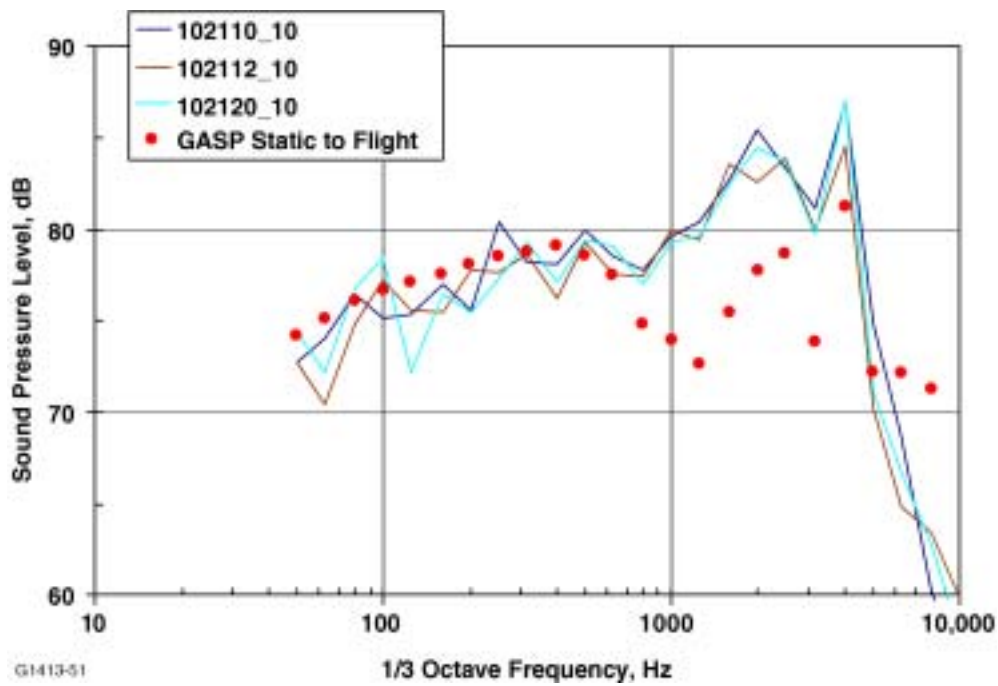


Figure 51. The Comparison of the Measured and Projected Spectra Before Overhead ($x=-252.0$ ft) Agree Well for the Low Frequency Jet Noise and the Blade Passage Tone at Take-off Power (82% N1).

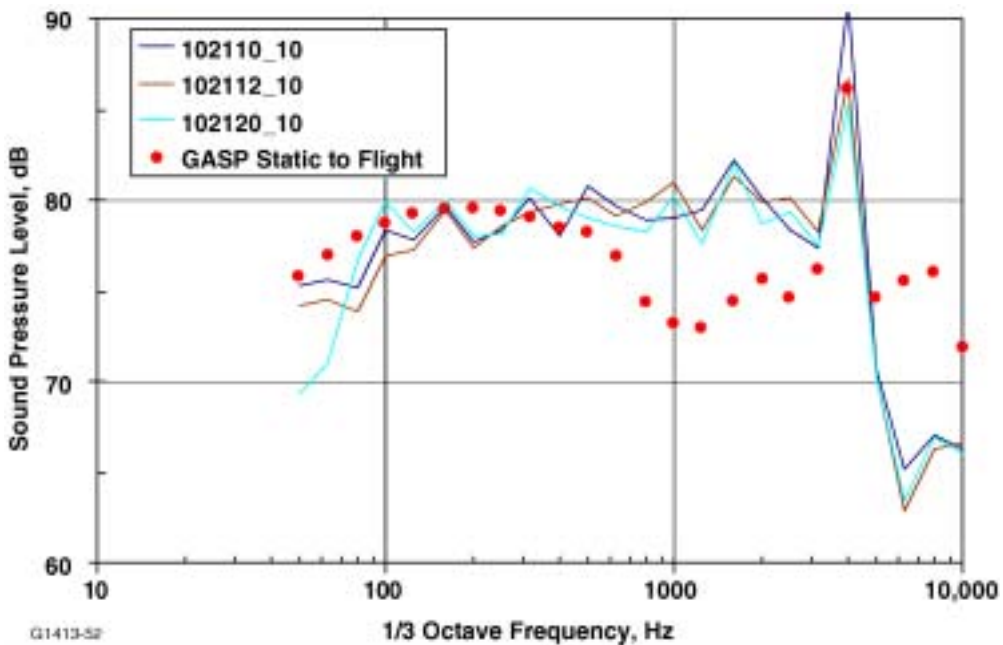


Figure 52. The Comparison of the Measured and Projected Spectra Near Overhead ($x=-92.6$ ft) Agree Well for the Low Frequency Jet Noise and the Blade Passage Tone at Take-off Power (82% N1).

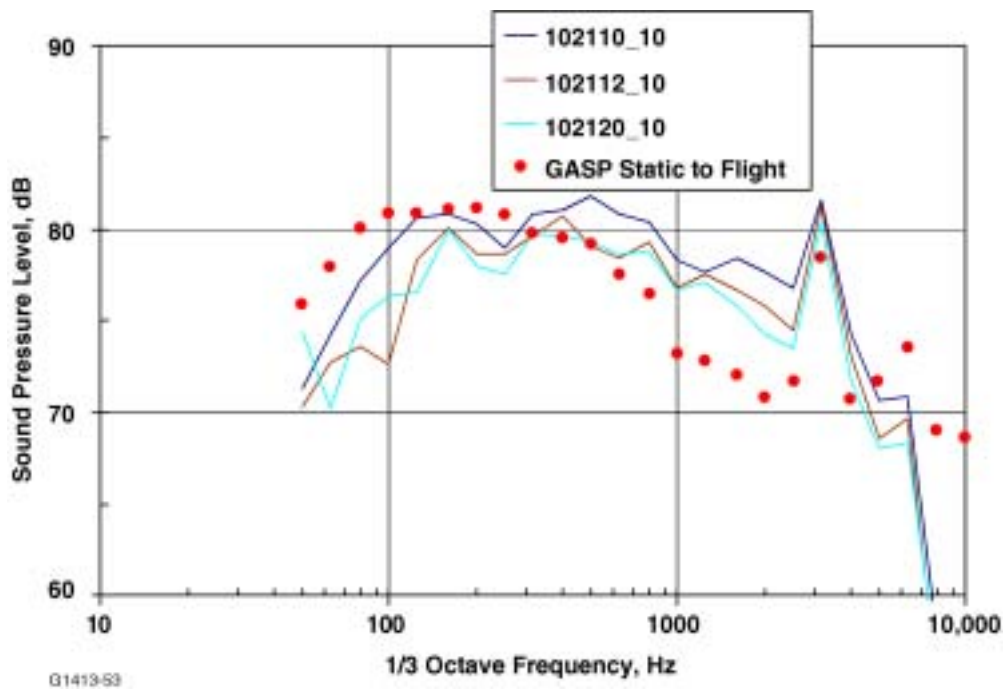


Figure 53. The Comparison of the Measured and Projected Spectra Past Overhead ($x=226.1$ ft) Agree Well for the Low Frequency Jet Noise and the Blade Passage Tone at Take-off Power (82% N1).

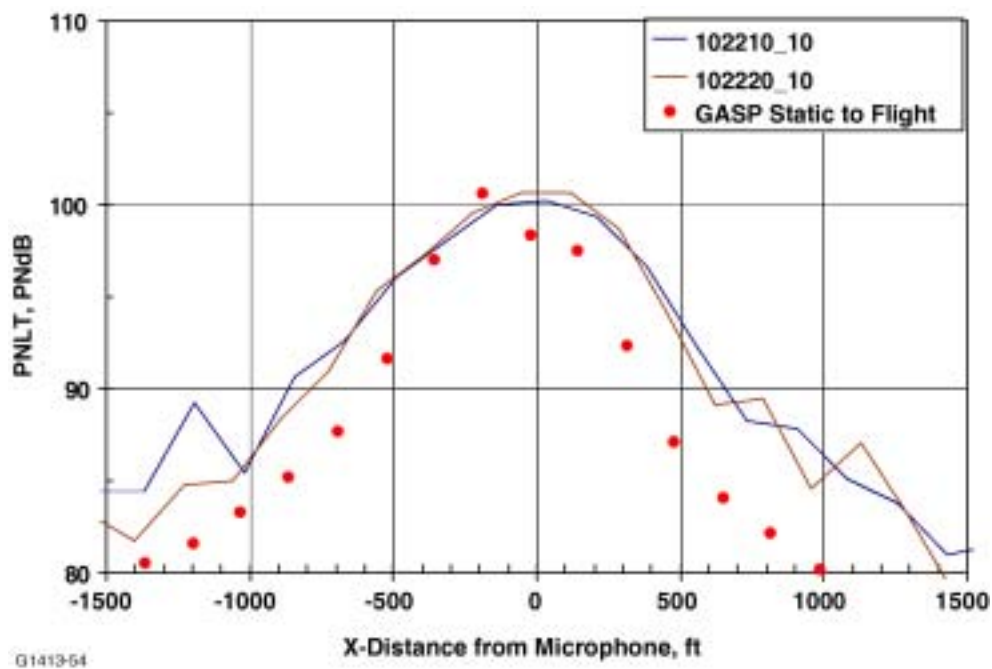


Figure 54. The Measured and Projected Tone-Corrected Perceived Noise Level Time Histories Agree Well for the Falcon 2000 at the High Power Approach Condition (60% N1).

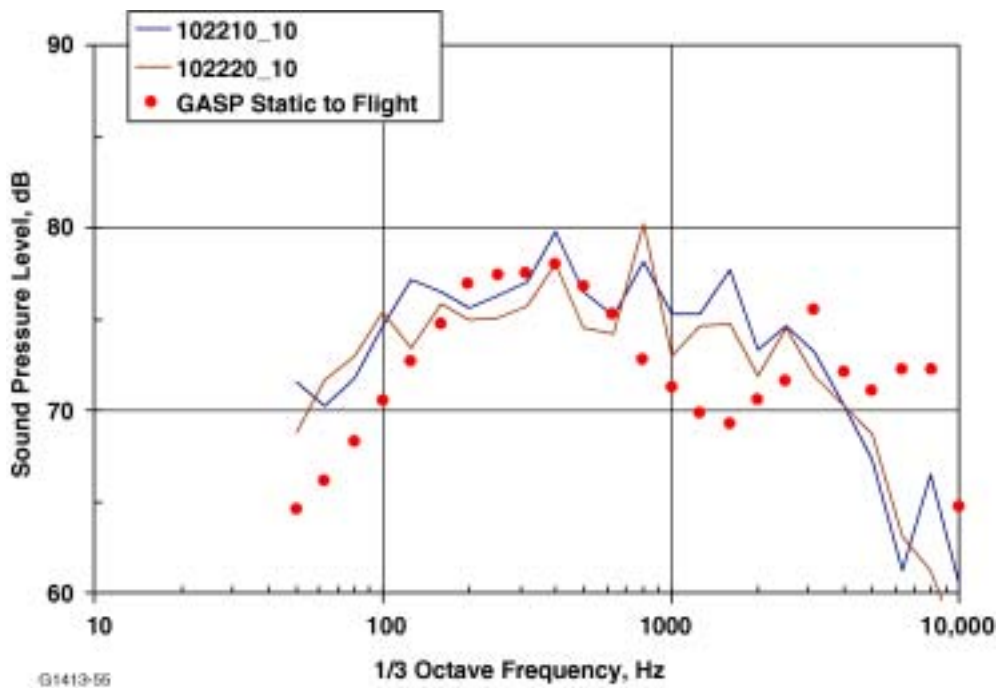


Figure 55. The Comparison of the Measured and Projected Spectra Before Overhead ($x=-189.2$ ft) Agree Well at High-Power Approach (60% N1).

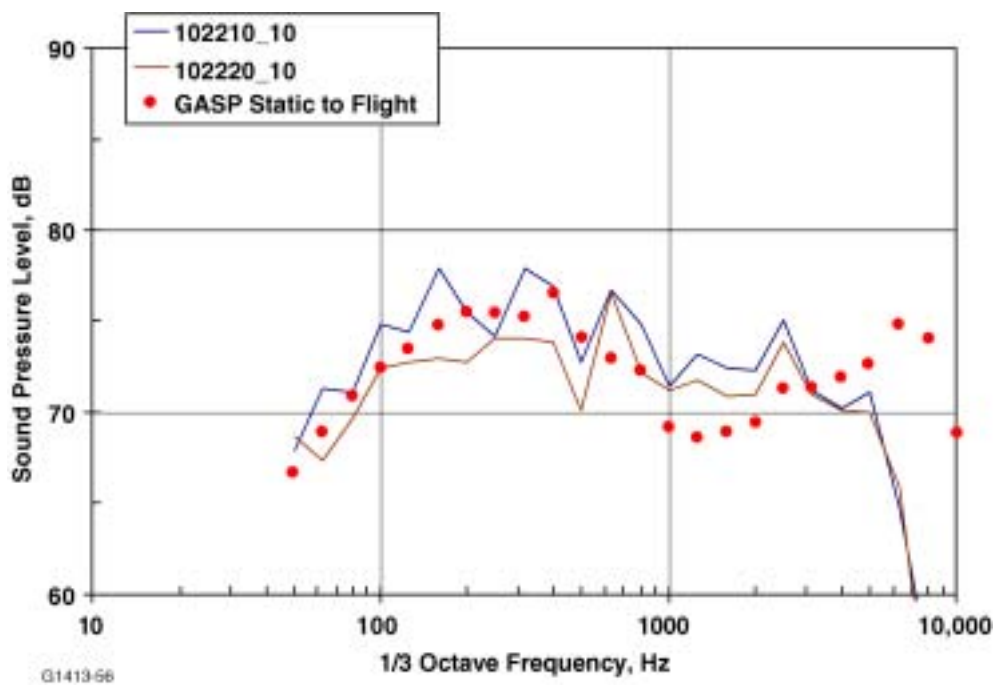


Figure 56. The Comparison of the Measured and Projected Spectra Near Overhead ($x=-21.1$ ft) Agree Well at High-Power Approach (60% N1).

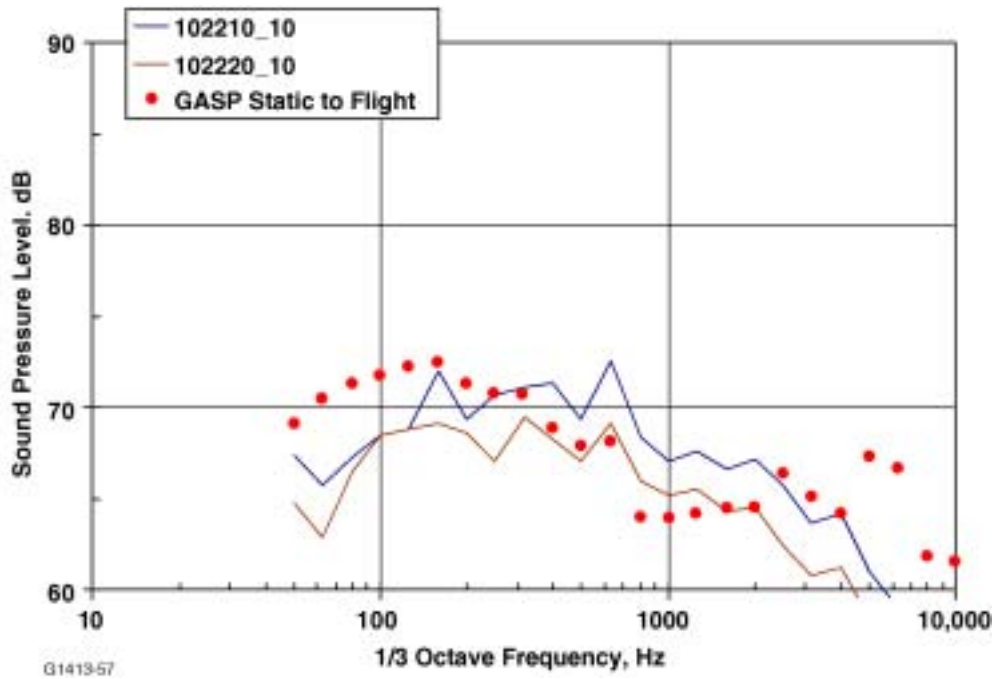


Figure 57. The Comparison of the Measured and Projected Spectra Past Overhead (x=315.0 ft) Agree Well at High-Power Approach (60% N1).

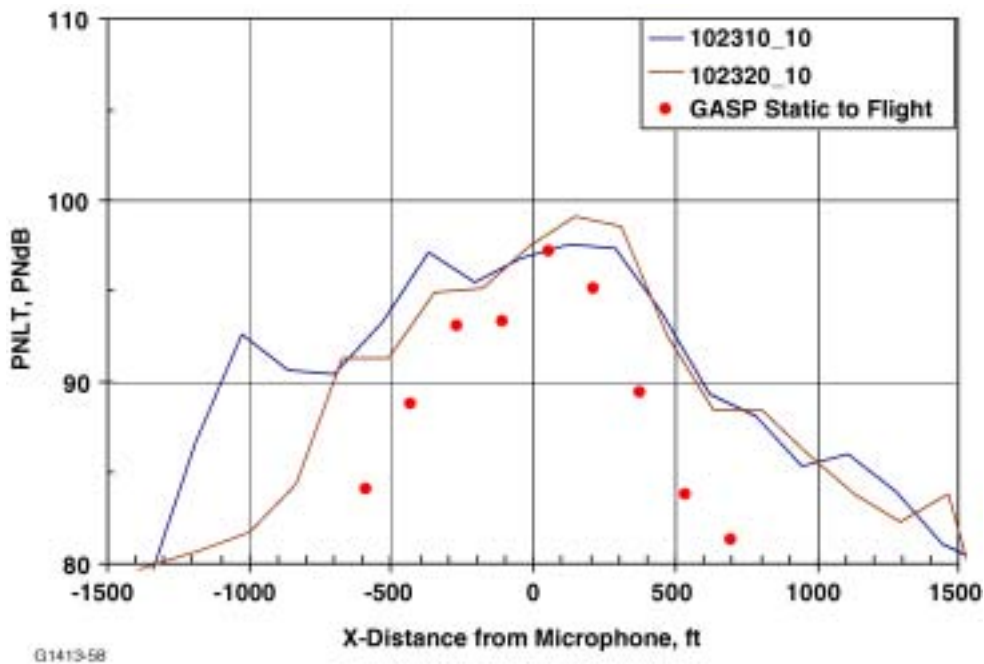


Figure 58. The Measured and Projected Tone-Corrected Perceived Noise Level Time Histories Agree Well for the Falcon 2000 at the Low Power Approach Condition (48% N1).

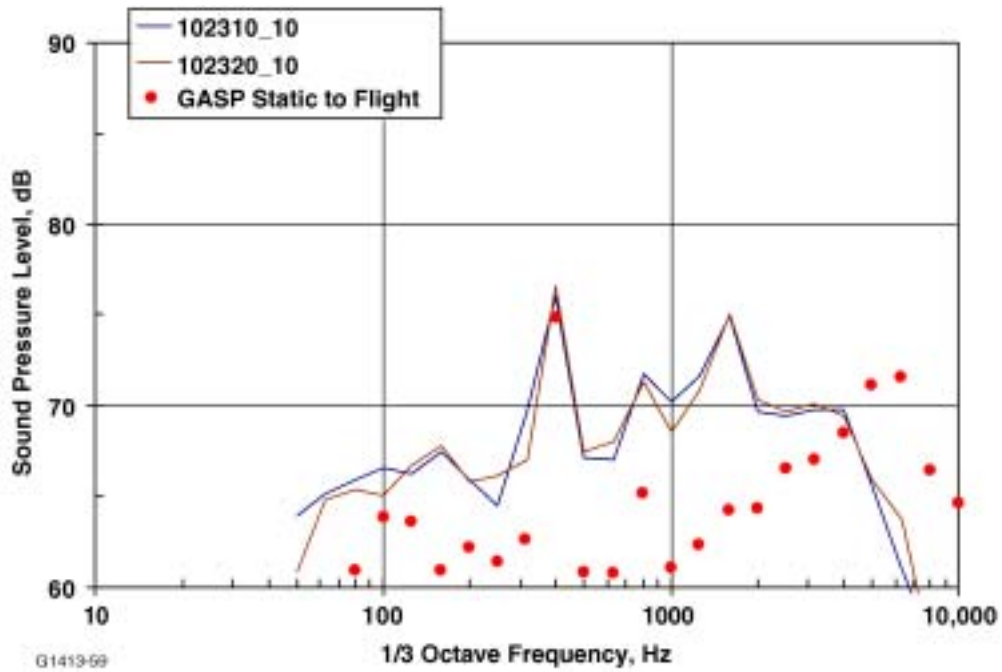


Figure 59. The Comparison of the Measured and Projected Spectra Before Overhead ($x=-108.8$ ft) at the Low-Power Approach (48% N1).

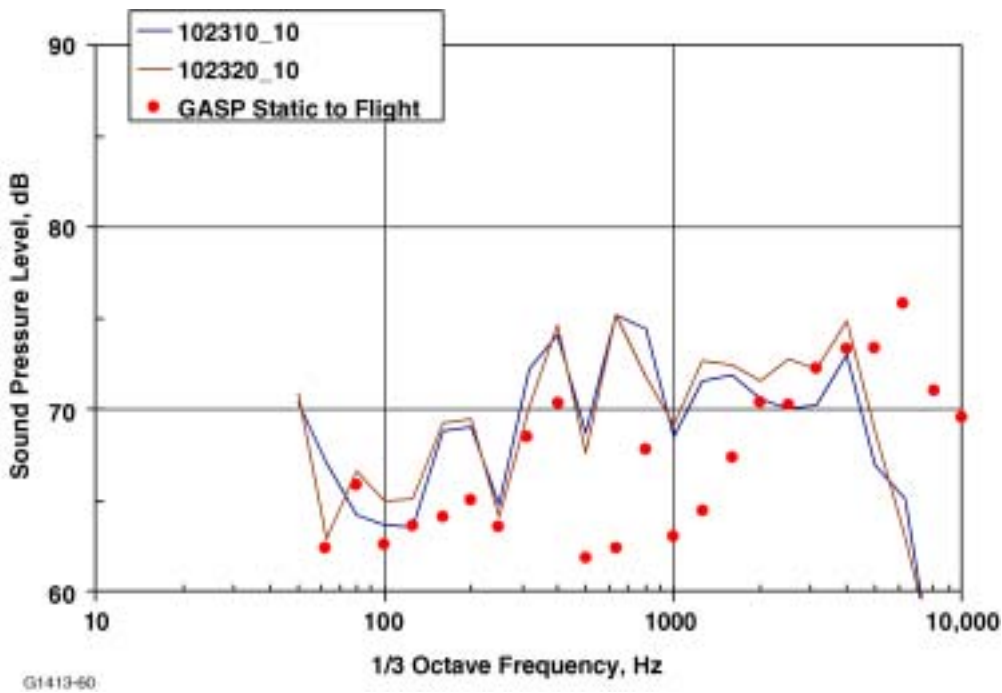


Figure 60. The Comparison of the Measured and Projected Spectra Near Overhead ($x=+51.9$ ft) at the Low-Power Approach (48% N1).

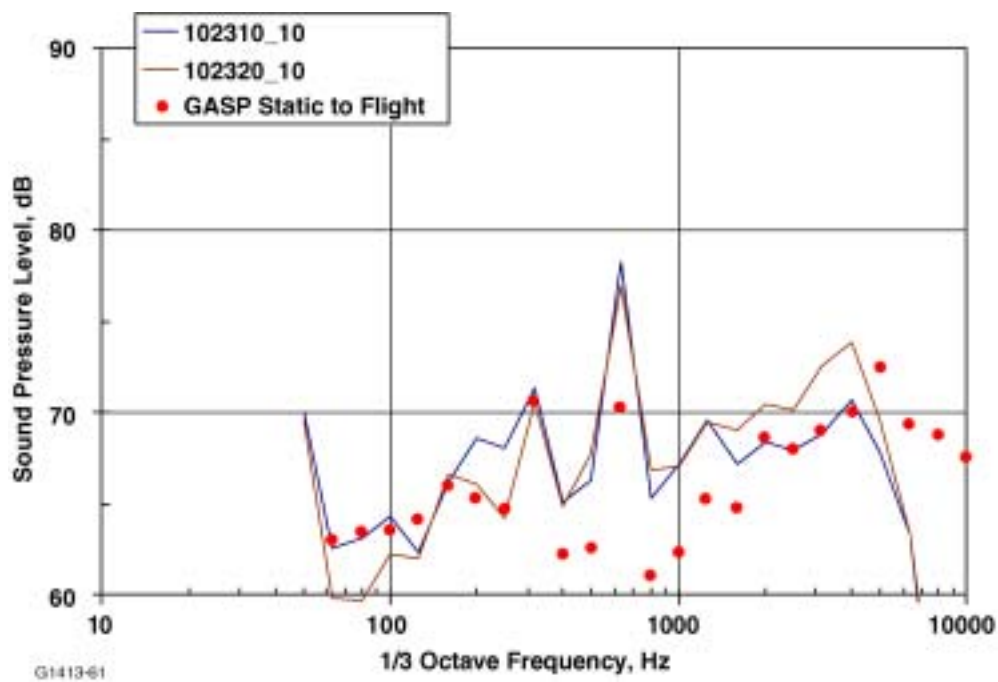


Figure 61. The Comparison of the Measured and Projected Spectra Past Overhead ($x=+212.6$ ft) at the Low-Power Approach (48% N1).

6. REFERENCES

- [1] Reed, D., Unpublished Presentation by Boeing, 2001.
- [2] Thomas, F.O., Nelson, R.C., and Lui, X., “Experimental Investigation of the Confluent Boundary Layer of a High-Lift System”, *AIAA Journal*, Volume 38, Number 6, pp. 978-988, June, 2000.
- [3] Hayes, J.A., Horne, C.W., Soderman, P.T., and Bent, P.H., “Airframe Noise Characteristics of a 4.7% Scale DC-10 Model ”, *AIAA Paper 97-1594-CP*, 3rd *AIAA/CEAS Aeroacoustics Conference and Exhibit*, Atlanta, GA, May, 1997.
- [4] Guo, Y.P., “A Model for Slat Noise Generation ”, *AIAA Paper 97-1647*, 3rd *AIAA/CEAS Aeroacoustics Conference and Exhibit*, Atlanta, GA, May, 1997.
- [5] Guo, Y.P., Hardy, B., Bent, P., Yamamoto, K., and Joshi, M., “Surface Pressure Fluctuations on DC-10 High Lift System and their Correlation with Far Field Noise”, NASI-20103, Task 2, NASA CRAD-9310-4872, 1998.
- [6] Guo, Y.P., Hardy, B., Bent, P., Yamamoto, K., and Joshi, M., “Noise Characteristics of DC-10 Aircraft High Lift Systems”, NASI-20103, Task 2, NASA CRAD-9310-4893, 1998.
- [7] Dobrzynski, W., Nagakura, K., Gehlhar, B., and Buschbaum, A., “Airframe Noise Studies on Wings with Deployed High-Lift Devices ”, *AIAA Paper 99-1805*, 5th *AIAA/CEAS Aeroacoustics Conference and Exhibit*, Bellevue, WA, May, 1999.
- [8] Storms, B.L., Hayes, J.A., Moriarty, P.J., and James, R.C., “Aeroacoustic Measurements of Slat Noise on a Three-Dimensional High-Lift System”, *AIAA Paper 99-1957*, 5th *AIAA/CEAS Aeroacoustics Conference and Exhibit*, Bellevue, WA, May, 1999.
- [9] Moriarty, P.J., and Heineck, J.T., “PIV Measurements Near a Leading Edge Slat” *Proceedings of the 3rd International Workshop on PIV*, 1999.
- [10] Khorrami, M.R., Berkman, M.E., Choudhari, M., Singer, B.A., Lockard, D.P., and Brentner, K.S., “Unsteady Flow Computations of a Slat with a Blunt Trailing Edge ”, *AIAA Paper 99-1805*, 5th *AIAA/CEAS Aeroacoustics Conference and Exhibit*, Bellevue, WA, May, 1999.
- [11] Singer, B.A., Lockard, D.P., Brentner, K.S., Khorrami, M.R., Berkman, M.E., and Choudhari, M., “Computational Aeroacoustic Analysis of Slat Trailing Edge Flow”, *AIAA Paper 99-1802*, 5th *AIAA/CEAS Aeroacoustics Conference and Exhibit*, Bellevue, WA, May, 1999.

- [12] Khorrami, M.R., Singer, B.A., Berkman, M.E., “Time Accurate Simulations and Acoustic Analysis of Slat Free-Shear Layer”, *AIAA Paper 01-2155*, 7th *AIAA/CEAS Aeroacoustics Conference and Exhibit*, Maastricht, Netherlands, May, 2001.
- [13] Meadows, K.R., Brooks, T.F., Humphreys, W.M., Hunter, W.W., and Gerhold, C.H., “Aeroacoustic Measurements of a Wing-Flap Configuration”, *AIAA Paper 97-1595*, 3rd *AIAA/CEAS Aeroacoustics Conference*, Atlanta, GA, May, 1997.
- [14] Brooks, T.F., Marcolini, M.A., Pope, D.S., “Airfoil Trailing-Edge Flow Measurements”, *AIAA Journal*, Volume 24, Number 8, pp. 1245-1251, 1986.
- [15] Brooks, T.F., Marcolini, M.A., and Pope, D.S., “A Directional Array Approach for the Measurement of Rotor Noise Source Distributions with Controlled Spatial Resolution”, *Journal of Sound and Vibration*, Volume 112, Number 1, pp. 192-197, 1987.
- [16] Marcolini, M.A., and Brooks, T.F., “Rotor Noise Measurement Using a Directional Microphone Array”, *Journal of the American Helicopter Society*, pp. 11-22, 1992.
- [17] Brooks, T.F., Pope, D.S., Marcolini, M.A., “Airfoil Self-Noise and Prediction”, *NASA Reference Publication 1218*, July, 1989.
- [18] Ahuja, K. K., Tanna, H. K., and Tester, B. J., “An experimental study of transmission, reflection, and scattering of sound in a free jet flight simulation facility and comparison with theory”, *Journal of Sound and Vibration* **75**, 51-85 (1981).
- [19] Amiet, R. K., “Correction of open jet wind tunnel measurements for shear layer refraction”, *American Institute of Aeronautics and Astronautics Paper 75-532* (1975).
- [20] Amiet, R. K., “Refraction of sound by a shear layer”, *Journal of Sound and Vibration* **58**, 467-482 (1978).
- [21] Amiet, R. K., “Correction of fan noise for the effects of forward flight”, *Journal of Sound and Vibration* **89**, 243-259 (1983).
- [22] Dowling, A. P., “Convective amplification of real simple sources”, *Journal of Fluid Mechanics* **74**, 529-546 (1976).
- [23] Dowling, A. P. and Ffowcs Williams, J. E., Sound and Sources of Sound, Ellis Horwood Limited (1893).
- [24] Graham E. W. and Graham, B. B., “Effect of a shear layer on plane waves of sound in a fluid”, *Journal of the Acoustical Society of America* **46**, 169-175 (1969).

- [25] International Civil Aviation Organization Committee on Aviation Environmental Protection, Environmental Technical Manual on the Use of Procedures in the Noise Certification of Aircraft, Steering Group Approved Revision 7, January 2000.
- [26] International Civil Aviation Organization, Environmental Protection, Annex 16. Third Edition, 1993.
- [27] Larson, R. S. “Convective amplification of gas turbine engine internal noise sources”, *Journal of Sound and Vibration* **74**, 123-137 (1981).
- [28] Miles, J. W., “On the reflection of sound at an interface of relative motion”, *Journal of the Acoustical Society of America* **29**, 226-228 (1957).
- [29] Morfey, C. L., “Acoustic energy”, AGARD Special Course on Acoustic Wave Propagation, AGARD-R-686, (1979).
- [30] Morfey, C. L., “Propagation from moving sources in flows”, AGARD Special Course on Acoustic Wave Propagation, AGARD-R-686, (1979).
- [31] Morfey, C. L. and Tester, B. J., “Noise measurements in a free-jet, flight simulation facility: shear layer effects and facility-to-flight corrections”, *American Institute of Aeronautics and Astronautics Paper* 76-531 (1976).
- [32] Morse, P. K. and Ingard, K., Theoretical Acoustics, Princeton University Press, 1968.
- [33] Nallasamy, M., “Computation of noise radiation from fan inlet and aft ducts”, *Journal of Aircraft*, **34**, 387-393 (1997).
- [34] Ribner, H. S., “Reflection, transmission, and amplification of sound by a moving medium”, *Journal of the Acoustical Society of America* **29**, 435-441 (1957).
- [35] Rice, E. J., “Broadband noise radiation models for aircraft engines”, in “Aeroacoustic prediction codes”, NASA CR 2000-210244 (2000).
- [36] Ross, R., Allen, R. M. and van Ditshuizen J. C. A., “Acoustic wave propagation through the shear layer of the DNW large open jet wind tunnel” *American Institute of Aeronautics and Astronautics Paper* 83-0699 (1983).
- [37] Ross, R., “Shear layer effects on pure tone propagation in open jet wind tunnels using 1/3 octave analysis”, *American Institute of Aeronautics and Astronautics Paper* 80-0984 (1980).
- [38] Schlinker, R. H., and Amiet, R. K., “Refraction of sound by a shear layer - experimental assessment”, *American Institute of Aeronautics and Astronautics Paper* 79-0628 (1979).

- [39] Society of Automotive Engineers, “Gas turbine jet exhaust noise prediction”, SAE Aerospace Recommended Practice 876, 1978.

- [40] Tester, B. J. and Morfey, C. L., “ Developments in jet noise modeling - theoretical predictions and comparisons with measured data, *Journal of Sound and Vibration* **46**, 79-103 (1976).

- [41] Zorumski, William E., Aircraft Noise Prediction Program Theoretical Manual, NASA Technical Memorandum 83199, 1982.

APPENDIX I

1/3-OCTAVE BAND SPL TIME HISTORIES OF ESTIMATED AIRFRAME NOISE

(3 pages)

1992 BASELINE TECHNOLOGY BUSINESS JET AIRFRAME NOISE

27.6 DEGREES		34.9 DEGREES		47.6 DEGREES	
BAND	AIRFRM	BAND	AIRFRM	BAND	AIRFRM
17	58.0	17	60.3	17	63.6
18	57.4	18	59.3	18	61.8
19	56.4	19	57.5	19	58.8
20	54.9	20	55.1	20	57.2
21	52.6	21	53.3	21	61.4
22	51.0	22	57.5	22	65.9
23	55.4	23	62.2	23	67.6
24	60.1	24	64.4	24	64.9
25	62.2	25	62.6	25	63.9
26	59.8	26	60.0	26	68.5
27	57.6	27	65.5	27	65.2
28	62.3	28	61.4	28	66.8
29	60.0	29	63.5	29	66.8
30	61.0	30	63.8	30	66.7
31	61.4	31	63.8	31	66.9
32	59.8	32	62.7	32	65.5
33	57.7	33	60.5	33	63.7
34	56.1	34	59.6	34	62.9
35	55.1	35	58.5	35	62.3
36	53.9	36	57.8	36	61.8
37	53.6	37	57.9	37	62.0
38	52.0	38	56.6	38	61.1
39	48.9	39	54.3	39	59.5
40	44.0	40	50.6	40	56.8

30.8 DEGREES		40.3 DEGREES		57.6 DEGREES	
BAND	AIRFRM	BAND	AIRFRM	BAND	AIRFRM
17	59.0	17	61.7	17	65.5
18	58.3	18	60.4	18	63.0
19	56.9	19	58.0	19	59.8
20	55.1	20	55.3	20	61.9
21	52.5	21	56.3	21	66.4
22	53.6	22	61.8	22	69.3
23	58.8	23	65.2	23	68.5
24	62.5	24	65.5	24	63.4
25	63.0	25	60.5	25	69.8
26	58.0	26	65.8	26	67.0
27	62.5	27	65.1	27	70.1
28	62.2	28	65.8	28	68.6
29	62.1	29	64.8	29	68.4
30	62.1	30	65.3	30	68.1
31	62.6	31	65.4	31	68.0
32	61.3	32	64.0	32	66.6
33	58.9	33	62.2	33	65.3
34	57.8	34	61.2	34	64.5
35	56.8	35	60.5	35	63.9
36	55.8	36	59.9	36	63.5
37	55.7	37	60.0	37	63.7
38	54.3	38	58.9	38	62.9
39	51.5	39	57.0	39	61.6
40	47.3	40	53.8	40	59.4

70.9 DEGREES

BAND	AIRFRM
17	66.5
18	63.3
19	62.0
20	66.2
21	69.9
22	71.0
23	67.4
24	68.0
25	71.5
26	69.4
27	69.8
28	70.0
29	69.8
30	69.5
31	68.7
32	67.2
33	66.3
34	65.5
35	65.0
36	64.6
37	64.7
38	64.1
39	62.8
40	60.8

105.0 DEGREES

BAND	AIRFRM
17	68.1
18	64.7
19	64.2
20	68.5
21	71.6
22	72.1
23	67.4
24	69.9
25	71.4
26	70.4
27	69.2
28	69.5
29	69.2
30	67.9
31	67.0
32	65.7
33	64.7
34	63.9
35	63.2
36	62.7
37	62.5
38	61.6
39	60.4
40	58.5

133.3 DEGREES

BAND	AIRFRM
17	70.9
18	68.6
19	65.2
20	63.7
21	67.4
22	71.1
23	71.3
24	67.1
25	66.3
26	68.9
27	65.7
28	66.1
29	66.2
30	65.3
31	63.7
32	61.9
33	60.7
34	59.7
35	58.6
36	57.2
37	56.3
38	54.8
39	52.8
40	50.5

87.4 DEGREES

BAND	AIRFRM
17	66.6
18	63.3
19	63.7
20	68.0
21	71.2
22	71.3
23	66.2
24	70.7
25	71.0
26	71.5
27	70.0
28	70.5
29	70.1
30	69.2
31	68.4
32	66.9
33	66.1
34	65.4
35	64.8
36	64.5
37	64.4
38	63.7
39	62.5
40	60.7

120.8 DEGREES

BAND	AIRFRM
17	69.8
18	66.8
19	63.9
20	66.5
21	70.5
22	72.4
23	70.2
24	65.5
25	71.2
26	66.6
27	69.6
28	68.4
29	67.6
30	66.7
31	65.5
32	64.0
33	62.9
34	62.1
35	61.0
36	60.1
37	59.5
38	58.4
39	56.8
40	54.8

142.4 DEGREES

BAND	AIRFRM
17	71.2
18	69.4
19	66.8
20	63.4
21	63.3
22	67.8
23	69.8
24	68.9
25	62.8
26	65.9
27	65.2
28	65.2
29	64.4
30	63.4
31	61.2
32	59.4
33	58.3
34	57.1
35	55.7
36	54.2
37	53.0
38	51.2
39	48.7
40	46.0

149.2 DEGREES

BAND	AIRFRM
17	69.7
18	68.4
19	66.4
20	63.6
21	60.6
22	62.4
23	65.8
24	67.2
25	65.1
26	58.7
27	64.3
28	61.4
29	63.2
30	61.5
31	58.7
32	56.8
33	55.7
34	54.2
35	52.8
36	50.9
37	49.7
38	47.6
39	44.7
40	41.4

APPENDIX II

**ANOPP THEORETICAL MANUAL CHAPTER FOR THE SHEAR LAYER
CORRECTION MODULE**

(14 pages)

INTRODUCTION

A static-to-flight correction procedure that does account for modifications to the jet shear layer is developed from existing models. The approach chosen here is a hybrid of corrections developed by Amiet in references [1], [2], and [3] and corrections developed by Morfey in references [4] and [5]. The procedure relates the in-flight, far-field, mean-square sound pressure to the statically measured, far-field, mean-square sound pressure as a function of flight speed. The correction process entails applying angle corrections to account for refraction at the shear layer and amplitude corrections to account for ray-tube divergence changes and forward flight effects. The effects of reflection of sound by the shear layer and scattering of sound by shear layer turbulence are ignored. These corrections are developed using a geometric acoustics approach for cylindrical shear layer geometry. The angle correction is based upon a vortex sheet model of the shear layer. The amplitude correction is based on the assumption of energy conservation across the shear layer.

SYMBOLS

A_e	engine reference area, m ² (ft ²)
A_j^*	area of jet, m ² (ft ²)
$\theta_e, \bar{\theta}_e$	Angle between retarded source position and “measurement” position in the flight case, deg
$\theta_m, \bar{\theta}_m$	Angle between source position and the measurement observer in the static case, deg
θ_c	Angle of acoustic ray propagation in the jet region, deg
$\phi_j, \phi_{js}, \phi_{jf}$	Wave normal angle in the jet region - general case, static case, flight case, deg
$\phi_a, \phi_{as}, \phi_{af}$	Wave normal angle in the ambient region - general case, static case, flight case, deg
h	Distance between source and shear layer, assumed equal to nozzle radius, m (ft)
r_{af}	Wave normal radius in the ambient region for the flight case, m (ft)
r_{as}	Wave normal radius in the ambient region for the static case, m (ft)
r_e	Distance between retarded source position and “measurement” position in the flight case, m (ft)
r_m, r_s	Distance between source and measurement position in the static case, m (ft)
V_j, V_{js}, V_{jf}	Velocity of the uniform flow in the jet region - general case, static case, flight case, m/s (ft/s)
V_a, V_{as}, V_{af}	Velocity of the uniform flow in the ambient region - general case, static case, flight case
M_j	Mach number in the jet region
M_a, M_∞	Mach number in the ambient region
T_j	jet total temperature, K (°R)
ρ_j	Fluid density in the jet region
ρ_a	Fluid density in the ambient region
c_j, c_{js}, c_{jf}	Speed of sound in the jet region - general case, static case, flight case
c_a, c_{as}, c_{af}	Speed of sound in the ambient region - general case, static case, flight case

INPUT

The values of the aircraft Mach number and jet noise parameters are provided by user. The one-third octave band source noise levels are provided by the appropriate source noise module. The independent variable values for the output table are obtained from the input table.

A_e	engine reference area, m^2 (ft^2)
A_j^*	area of jet, re A_e
M_∞	aircraft Mach number
r_s	distance from source to polar observer array, m (ft)
T_j^*	jet total temperature, re T_∞
V_j^*	jet velocity, re c_∞

Source Noise Data Table (for static engine conditions)

f	frequency, Hz
θ	polar directivity angle, deg
ϕ	azimuthal directivity angle, deg
$\langle p^2(f,\theta,\phi) \rangle^*$	mean square acoustic pressure, re $\rho_\infty^2 c_\infty^4$

OUTPUT

The output of this module is a table of the mean-square acoustic pressure as a function of frequency, polar directivity angle, and azimuthal directivity angle corrected for jet shear layer effects.

Shear Layer Corrected Source Noise Data Table

f	frequency, Hz
θ	polar directivity angle, deg
ϕ	azimuthal directivity angle, deg
$\langle p^2(f, \theta, \phi) \rangle^*$	mean square acoustic pressure, re $\rho_\infty^2 c_\infty^4$

METHOD

Problem Geometry

The model geometry for the correction procedure is shown in Figure II-1. An axially symmetric point source S is situated at the exhaust plane on the centerline of a cylindrical jet. A uniform flow of Mach number M_j exists in the jet, which has a constant density ρ_j and constant speed of sound c_j . A shear layer of constant radius h separates the jet from the ambient fluid, which maintains a constant density ρ_a and constant speed of sound c_a . The source S emits sound in all directions. Sound emitted in the wave normal direction ϕ_j is convected by the jet flow. The resulting ray path makes an angle θ_c with respect to the source and intersects the shear layer at the point C . In the static case, the sound is refracted by the shear layer to a wave normal angle ϕ_{as} . The sound propagates through the ambient medium in the wave normal direction ϕ_{as} at speed c_a . The sound arrives at the measurement position M , which lies a distance r_m and angle θ_m from the source. In the flight case, the sound is refracted by the shear layer to a different wave normal angle ϕ_{af} . The sound propagates through the ambient medium in the wave normal direction ϕ_{af} at speed c_a , and is also convected by the ambient flow at speed $M_a c_a$. Sound traveling in the upstream direction is considered to re-enter the nozzle and thus does not contribute to the far-field noise.

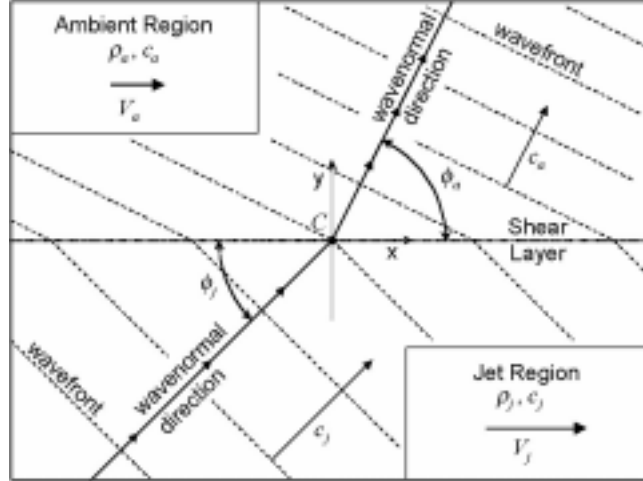


Figure II-2. The Refraction Angle Correction is Derived by Considering Plane Wave Interaction With a Vortex Sheet.

Equation (1) can be used to describe how the ambient wave normal angle is modified when the engine nozzle is taken from static to flight conditions. Using additional subscripts “ s ” and “ f ” to denote the static and flight conditions, and writing the refraction equation for each case yields

Static case:
$$\frac{c_{js}}{\cos \phi_{js}} + V_{js} = \frac{c_{as}}{\cos \phi_{as}} \quad (2)$$

Flight case:
$$\frac{c_{jf}}{\cos \phi_{jf}} + V_{jf} = \frac{c_{af}}{\cos \phi_{af}} + V_{af} \quad (3)$$

It is assumed that the jet velocity remains constant when moving from static to flight conditions, so that $V_{js} = V_{jf} \equiv V_j$. It is also assumed that the temperature in the jet and ambient regions do not change when moving from static to flight conditions, so that $c_{js} = c_{jf} \equiv c_j$ and $c_{as} = c_{af} \equiv c_a$. Finally, it is assumed that the external flow does not affect the generation and propagation of the noise inside the jet. Then the wavenormal angle within the jet is identical in the static and flight cases, so that $\phi_{js} = \phi_{jf}$. Under these assumptions, Equations (2) and (3) can then be combined to provide the following relationship between the ambient wavenormal angles in the static and flight cases:

$$\cos \phi_{af} = \frac{\cos \phi_{as}}{1 - M_a \cos \phi_{as}} \quad (4)$$

where $M_a \equiv M_{af} = V_{af}/c_a$. Equation (4) is the basic static-to-flight angle correction described by Morfey in reference [30]. It relates the ambient wavenormal angle ϕ_{af} in the flight case to the ambient wavenormal angle ϕ_{as} in the static case and the flight Mach number M_a .

Static-to-Flight Amplitude Correction

The amplitude correction is derived from geometric acoustics with the assumption that energy is conserved across the shear layer in a reference frame attached to the jet. The correction applies to high-frequency sound transmission, where the acoustic wavelength of the sound is smaller than the thickness of the shear layer so that reflections off the shear layer can be ignored. Morfey derived an amplitude correction in reference [4] that relates the far-field mean-square pressure outside of a cylindrical shear layer to the mean-square pressure incident upon the shear layer. The relationship between the far-field mean-square pressure $p_a^2(\phi_a)$ outside the shear layer, to the mean-square pressure $p_j^2(\phi_j)$ inside the shear layer is given by

$$r_a^2 p_a^2(\phi_a) = r_j^2 p_j^2(\phi_j) \frac{\rho_a (1 + M_j \cos \phi_j)^4}{\rho_j (1 + M_a \cos \phi_a)^4} \quad (5)$$

The distances r_j and r_a are the wave front radii in the jet and ambient regions respectively. The angles ϕ_j and ϕ_a are the wave normal angles in the jet and ambient regions, measured relative to the jet direction. Morfey used this result in reference [5] to derive a static-to-flight correction that relates the amplitudes of the far-field pressure in the static case to the far-field pressure in the flight case. This is done by writing Equation (5) for the static and flight cases and taking the ratio to obtain

$$r_{af}^2 p_{af}^2(\phi_{af}) = \frac{r_{as}^2 p_{as}^2(\phi_{as})}{(1 + M_{af} \cos \phi_{af})^4}$$

The derivation of this result assumes that the jet wave normal angle and jet Mach number are not affected by the ambient flow. In addition, the density in the jet and ambient regions is assumed to be unchanged by flight. Under these assumptions, the amplitude correction is independent of the jet conditions. The influence of the jet is captured in the angle relationship given by Equation (4).

For the case when the wave front radii are equal in the static and flight cases, the amplitude relation simplifies to

$$p_{af}^2(\phi_{af}) = \frac{p_{as}^2(\phi_{as})}{(1 + M_{af} \cos \phi_{af})^4} \quad (6)$$

Equation (6) is the amplitude correction that is used in the procedure. It states that the far-field mean-square sound pressure at a flight wave normal angle ϕ_{af} can be calculated by dividing the mean-square sound pressure measured at a static wave normal angle ϕ_{as} by the Doppler factor $(1 + M_{af} \cos \phi_{af})^4$. This equation assumes that the measurements are made in the far-field, which is generally the case for static engine noise testing.

Equation (6) has a form reminiscent of the traditional convective amplification correction:

$$p_f^2(r_e, \bar{\theta}_e) = \frac{p_s^2(r_e, \bar{\theta}_e)}{(1 - M \cos \bar{\theta}_e)^\alpha} \quad (7)$$

However, the two equations are not identical. Presuming that the direction of motion is directly opposite the jet flow direction, the two equations can be compared. Writing Equation (7) in terms of an angle $\theta_e = \pi - \bar{\theta}_e$ measured relative to the jet direction gives

$$p_f^2(r_e, \theta_e) = \frac{p_s^2(r_e, \theta_e)}{(1 + M \cos \theta_e)^4}$$

The difference between the correction equations is now apparent. In the traditional convective amplification correction, the flight sound amplitude at θ_e is related to the static sound amplitude at the same wave normal angle θ_e . In the shear layer correction, the flight sound amplitude at ϕ_{af} is related to the static sound amplitude at a different wave normal angle ϕ_{as} . The difference is a result of the ambient flow modifying the refraction through the shear layer.

Angle Relationships

An attractive feature of the angle and amplitude corrections is that they are straightforward and easily computed. To apply the corrections, the statically measured mean-square pressure must be provided as a function of the ambient wave normal angle ϕ_{as} , measured relative to the jet axis. Far-field static engine noise measurements are usually described in terms of a source-to-observer measurement angle θ_m (usually measured relative to the inlet, but the opposite convention is used here). Thus a relationship between θ_m and ϕ_{as} is needed. As described by Amiet in reference [2], a relationship between the two angles can be easily derived from geometrical considerations.

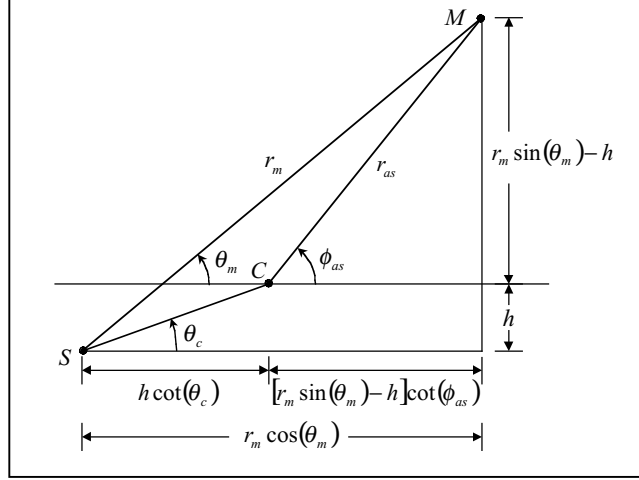


Figure II-3. A Relationship Between the Measurement Angle θ_m and Wave Normal Angle ϕ_{as} Can Be Derived From Geometrical Considerations.

Referring to Figure II-3, a relationship between the ambient wave normal angle ϕ_{as} , the source-to-observer angle θ_m , and the corrected angle θ_c can be derived from triangle relationships. Relating the length of the bases of the three right triangles in the Figure yields

$$r_m \cos(\theta_m) = h \cot(\theta_c) + [r_m \sin(\theta_m) - h] \cot(\phi_{as}) \quad (8)$$

The wave normal distance r_{as} over which the sound travels in the ambient region can also be computed from triangle relationships, and is given by

$$r_{as} = \sqrt{(r_m \sin(\theta_m) - h)^2 + ((r_m \sin(\theta_m) - h) \cot(\phi_{as}))^2} \quad (9)$$

Note that the corrected angle θ_c appears in Equation (8) as a parameter. It can be expressed in terms of the ambient wave normal angle ϕ_{as} as follows. First, a relation between the ray path angle θ_c and the jet wave normal angle ϕ_{js} is derived.

Figure II-4 shows how ray paths and wave normal angles can be related. A stationary point source S situated on the x-axis is immersed in a uniform flow of subsonic Mach number M . For purposes of illustration, S is a monopole source emitting sound at a single frequency. The constant phase surfaces or wavefronts form circles that are convected downstream by the flow. Sound emitted by the source at a wave normal angle ϕ propagates radially outward from the source in this direction at the speed of sound c . The sound is also convected downstream by the flow at speed V . Figure II-4 displays the wave fronts at successive increments in time. An open circle marks the portion of the wave front that was originally emitted in the ϕ direction by the source. By definition, the position of the open circles makes an angle ϕ with respect to the

retarded source position. Due to convection by the mean flow, these open circles trace out a straight-line path that makes an angle θ_c with respect to the x-axis.

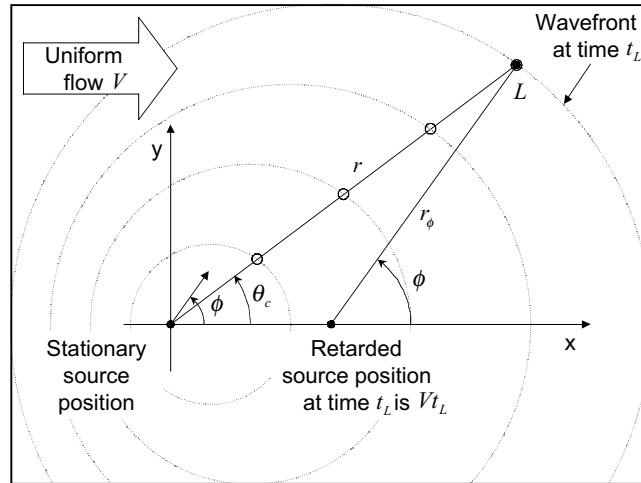


Figure II-4. The ray path angle θ_c and the wavenormal angle ϕ are geometrically related.

The relationship between θ_c and ϕ is easily determined from geometrical considerations. Figure II-5 displays the geometry for a particular time t_L .

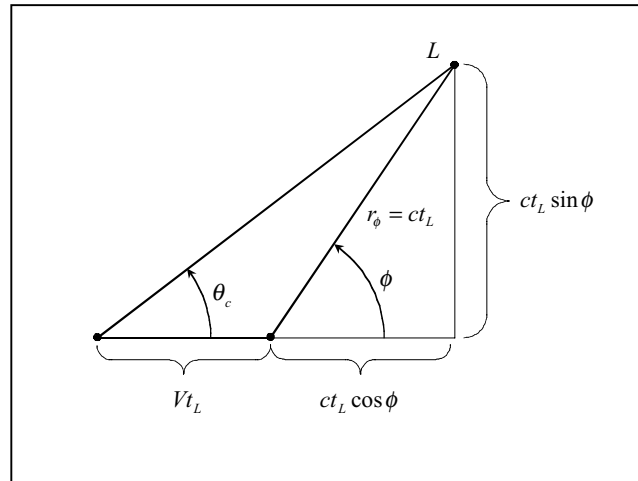


Figure II-5. The Relationship Between θ_c and ϕ is Derived From Triangle Relationships.

Considering triangle relationships, θ_c and ϕ are related via:

$$\tan(\theta_c) = \frac{ct_L \sin \phi}{Vt_L + ct_L \cos \phi} = \frac{\sin \phi}{M + \cos \phi}$$

Returning now to the geometry of Figure II-3, the relationship between θ_c and ϕ_{js} is

$$\tan(\theta_c) = \frac{\sin \phi_{js}}{M_{js} + \cos \phi_{js}} \quad (10)$$

This relationship can be expressed in terms of the ambient wave normal angle ϕ_{as} using the static angle refraction relation, Equation (2). First note that Equation (2) implies

$$\cos \phi_{js} = \frac{c_j \cos \phi_{as}}{c_a - V_j \cos \phi_{as}} = \frac{\cos \phi_{as}}{\frac{c_a}{c_j} - M_j \cos \phi_{as}}$$

and

$$\sin \phi_{js} = \frac{\sqrt{\left(\frac{c_a}{c_j} - M_j \cos \phi_{as}\right)^2 - \cos^2 \phi_{as}}}{\frac{c_a}{c_j} - M_j \cos \phi_{as}}$$

Substituting into Equation (10) produces the desired relationship between θ_c and ϕ_{as}

$$\tan(\theta_c) = \frac{\sqrt{\left(\frac{c_a}{c_j} - M_j \cos \phi_{as}\right)^2 - \cos^2 \phi_{as}}}{\frac{c_a}{c_j} M_j + (1 - M_j^2) \cos \phi_{as}} \quad (11)$$

This reduces to Equation (1) of Reference [3] when the temperatures of the jet and ambient regions are identical. Thus, given θ_m , r_m , h and M_j , the static ambient wave normal angle ϕ_{as} can be determined using Equation (8) and (11).

Implementation of the Corrections

Static engine noise measurements are obtained at far-field coordinates (θ_m, r_m) relative to the source position, with θ_m measured relative to the exhaust centerline. At a given measurement location, Equations (8) and (11) are used to calculate the corresponding static ambient wave normal angle ϕ_{as} . The statically measured mean-square pressure $p_m^2(\theta_m, r_m)$ can then be re-identified as $p_{as}^2(\phi_{as}, r_{as})$, where the wave normal coordinates (ϕ_{as}, r_{as}) are measured relative to the shear layer intersection point C . Next, the flight ambient wave normal angle ϕ_{af} is computed using Equation (4). Finally, the flight-corrected mean-square pressure $p_{af}^2(\phi_{af}, r_{af})$ at an equal wave normal distance $r_{af} = r_{as}$ from the point C is computed using Equation (6).

Continuing the assumption of a point source, the effect of refraction changes due to flight is to simply shift the directivity by an amount equal to the difference between the static and flight ambient wave normal angles. That is, in flight, sound will be emitted from the source in a direction Φ_f given by

$$\Phi_f = \theta_m - (\phi_{as} - \phi_{af}) \quad (12)$$

The mean-square pressure in this direction at a wave normal distance (i.e., distance from the retarded source position) equal to r_m is still provided by Equation (6) but written using the variable Φ_f ,

$$p_f^2(\Phi_f, r_m) = \frac{p_m^2(\theta_m, r_m)}{(1 + M_f \cos \Phi_f)^4} \quad (13)$$

The values of p_f^2 at the original angles θ_m can be obtained by interpolation. The accuracy of these approximations improves when $r_m \sin \theta_m \gg h$. Referring to Figure II-6, as $h/(r_m \sin \theta_m) \rightarrow 0$ with $\overline{CF} = \overline{CM} = r_{as}$, then $\angle FSM \rightarrow \angle FCM = \phi_{af} - \phi_{as}$ and $r_f \rightarrow r_m$. So for distant sideline observers, as is the case in fly-over noise studies, the approximation becomes quite acceptable.

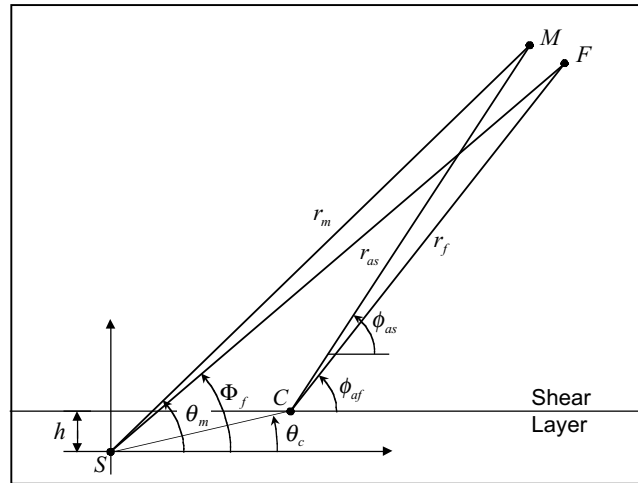


Figure II-6. The approximation improves as the sideline distance from the shear layer increases.

Noise Prediction

The simplified jet shear layer static-to-flight correction procedure for internally generated engine exhaust noise can be summarized in the following steps:

1. Measure or predict the static mean-square pressure $p_m^2(r_m, \theta_m)$ of the internally generated engine exhaust noise at a fixed radius r_m and at various angles θ_m from the source taken from the input table $\langle p^2(f, \theta, \phi) \rangle^*$. Source-separation techniques may be required.
2. For a given measurement angle θ_m , compute the static ambient wave normal angle ϕ_{as} using Equations (2), (8), and (10). An iterative procedure must be used, since ϕ_{as} cannot be expressed explicitly in terms of θ_m .
3. Compute the flight ambient wave normal angle ϕ_{af} using Equation (4).
4. Compute the approximate flight emission angle Φ_f using Equation (12).
5. Compute the flight-corrected mean-square pressure $p_f^2(\Phi_f, r_m)$ using Equation (13).
6. Interpolate the flight-corrected mean-square pressure $p_f^2(\Phi_f, r_m)$ back to the original measurement angles θ_m .

REFERENCES

- [1] Ahuja, K. K., Tanna, H. K., and Tester, B. J, “An experimental study of transmission, reflection, and scattering of sound in a free jet flight simulation facility and comparison with theory”, *Journal of Sound and Vibration* **75**, 51-85 (1981).
- [2] Amiet, R. K., “Correction of open jet wind tunnel measurements for shear layer refraction”, *American Institute of Aeronautics and Astronautics Paper* 75-532 (1975).
- [3] Amiet, R. K., “Refraction of sound by a shear layer”, *Journal of Sound and Vibration* **58**, 467-482 (1978).
- [4] Morfey, C. L., “Acoustic energy”, AGARD Special Course on Acoustic Wave Propagation, AGARD-R-686, (1979).
- [5] Morfey, C. L., “Propagation from moving sources in flows”, AGARD Special Course on Acoustic Wave Propagation, AGARD-R-686, (1979).
- [6] Morse, P. K. and Ingard, K., Theoretical Acoustics, Princeton University Press, 1968.

APPENDIX III

**ANOPP USER MANUAL CHAPTER FOR THE SHEAR LAYER CORRECTION
MODULE**

(3 pages)

*

*

*

*

*

*

*

*

*

*

*

*

*

*

*

*

*

*

*

*

*

*

*

*

*

*

*

*

*

*

*

*

*

*

*

*

*

*

*

*

*

*

*

*

*

*

*

*

*

*

*

*

*

*

*

*

*

PURPOSE - TO COMPUTE THE IN-FLIGHT, FAR-FIELD, MEAN-SQUARE SOUND
PRESSURE TO STATIC FAR-FIELD, MEAN SQUARE SOUND
PRESSURE AS A FUNCTION OF FLIGHT SPEED

AUTHOR - DSW(L03/02/XX)

INPUT

USER PARAMETERS	DEFAULT
AE - ENGINE REFERENCE AREA (RS), M**2 (FT**2)	PI/4
RS - DISTANCE FROM SOURCE TO OBSERVER (RS)	SQRT(AE)
AJ - AREA OF FULLY EXPANDED PRIMARY JET, RE ENGINE REFERENCE AREA (RS)	1.0
TJ - ABSOLUTE TOTAL TEMPERATURE OF THE PRIMARY JET, RE AMBIENT TEMPERATURE (RS)	1.0
VJ - VELOCITY OF PRIMARY JET RELATIVE TO NOZZLE EXIT, RE AMBIENT SPEED OF SOUND (RS)	1.0
MA - AIRCRAFT MACH NUMBER (RS)	0.
SCRXXX - THREE LETTER CODE, XXX, USED TO FORM INPUT TABLE NAME NOISE (XXXNNN) AND OUTPUT TABLE NAME, NOISES (XXXNNN)	3HXXX
SCRNNN - INTEGER VALUE, NNN, .GT. 0 USED TO FORM INPUT TABLE NAME NOISE (XXXNNN) AND OUTPUT TABLE NAME, NOISES (XXXNNN)	001
IPRINT - PRINT FLAG (I) =0, NO PRINT DESIRED =1, INPUT PRINT ONLY =2, OUTPUT PRINT ONLY =3, BOTH INPUT AND OUTPUT PRINT	3
RHOA - AMBIENT DENSITY (RS), KG/M**3 (SLUG/FT**3)	1.225
CA - AMBIENT SPEED OF SOUND (RS), M/S (FT/SEC)	340.294
IOUT - OUTPUT CODE (FOR TABLE AND/OR PRINTED OUTPUT) 0 NO PRINT, BUT GENERATE TABLE NOISES (XXXNNN) -1 PRINT OUTPUT IN DB UNITS, BUT DO NOT GENERATE TABLE NOISES (XXXNNN) -2 PRINT OUTPUT IN DIMENSIONLESS UNITS, BUT DO NOT GENERATE TABLE NOISES (XXXNNN) -3 BOTH OPTIONS -1 AND -2 1 PRINT OUTPUT IN DB UNITS AND GENERATE TABLE NOISES (XXXNNN) 2 PRINT OUTPUT IN DIMENSIONLESS UNITS AND GENERATE TABLE NOISES (XXXNNN) 3 BOTH OPTIONS 1 AND 2	3
IUNITS - INPUT UNITS FLAG 2HSI, SI UNITS 7HENGLISH, ENGLISH UNITS	SI

DATA BASE UNIT MEMBERS

(DESCRIBED UNDER DATA BASE STRUCTURES)

NOISE (XXXNNN) NOTE MEMBER NAME XXXNNN IS FORMED FROM
USER PARAMETERS SCRXXX AND SCRNNN.

```

*
* OUTPUT
*
*   SYSTEM PARAMETERS
*     NERR    - ERROR FLAG
*               .TRUE.,  IMPLIES AN ERROR WAS ENCOUNTERED
*                   DURING MODULE EXECUTION
*               .FALSE., NO ERROR ENCOUNTERED
*
*   DATA BASE UNIT MEMBERS
*     NOISES (XXXNNN) SEE FORMAT UNDER DATA BASE STRUCTURES.
*                   NOTE MEMBER NAME XXXNNN IS FORMED FROM
*                   USER PARAMETERS SCRXXX AND SCRNNN.
*
*   DATA BASE STRUCTURES
*     NOISE    (XXXNNN) TYPE 1 TABLE CONTAINING MEAN SQUARE
*                   ACOUSTIC PRESSURE AS A FUNCTION OF
*                   (1) FREQUENCY, (2) DIRECTIVITY ANGLE
*                   AND (3) AZIMUTHAL ANGLE.  SEE INFORMATION
*                   ON OVERRIDING THIS UNIT NAME UNDER
*                   DESCRIPTION OF NOISES (XXXNNN).
*     NOISES   (XXXNNN) TYPE 1 TABLE CONTAINING SHEAR-LAYER CORRECTED
*                   MEAN SQUARE ACOUSTIC PRESSURE AS A FUNCTION
*                   OF (1) FREQUENCY, (2) DIRECTIVITY ANGLE,
*                   AND (3) AZIMUTH ANGLE.  WHEN OVERRIDING
*                   THIS UNIT NAME, THE NAME OF THE UNIT MUST
*                   BE THE SAME AS THE NAME OF THE UNIT CONTAIN
*                   ING THE INPUT NOISE TABLE WITH AN 'S' ON
*                   THE END.  EXAMPLE (1) : SUPPOSE THE UNIT
*                   CONTAINING THE INPUT NOISE TABLE IS 'DATE'.
*                   THE NAME OF THE UNIT CONTAINING THE OUTPUT
*                   NOISE TABLE WILL BECOME 'DATES'.  EXAMPLE
*                   (2) : SUPPOSE THE UNIT CONTAINING THE OUTPUT
*                   NOISE TABLE IS OVERRIDEN TO BECOME 'STORES'
*                   THEN THE UNIT CONTAINING THE INPUT NOISE
*                   TABLE MUST BE OVERRIDEN TO BE 'STORE'.
*                   EXAMPLE (3) : IF THE INPUT UNIT IS TO BE
*                   'TABLE', THEN TO OVERRIDE THIS OUTPUT UNIT
*                   TO BE SOMETHING OTHER THAN 'TABLES', THE
*                   FOLLOWING MUST BE DONE.  FOR EXAMPLE, THE
*                   INPUT UNIT IS 'TABLE'; THE OUTPUT UNIT IS
*                   TO BE 'STORE'.  OVERRIDE 'NOISE' TO BE
*                   'TABLE' AND OVERRIDE 'TABLES' TO BE 'STORE'
*
*   ERRORS
*     NON-FATAL
*       1.  INSUFFICIENT DYNAMIC STORAGE.
*       2.  INTERPOLATION ERROR ON INPUT NOISE TABLE.
*       3.  INVALID VALUE FOR INPUT USER PARAMETER.  DEFAULT
*           VALUE WILL BE USED.
*       4.  ERROR IN BUILDING OUTPUT TABLE OF SUPPRESSED NOISE.
*     FATAL - NONE
*
*   LDS REQUIREMENTS
*     LENGTH = ( 2 * NFREQ ) + NTHETA + NPHI +
*              ( NTHETA * NPHI ) * ( 1 + NFREQ )
*     WHERE :
*     NFREQ  = NUMBER OF FREQUENCY VALUES ON INPUT AND OUTPUT

```

```
*
*           NOISE TABLES
*           NTHETA = NUMBER OF DIRECTIVITY ANGLE VALUES ON INPUT
*           AND OUTPUT NOISE TABLES
*           NPHI   = NUMBER OF AZIMUTH ANGLE VALUES ON INPUT AND
*           OUTPUT NOISE TABLES
*
* GDS REQUIREMENTS
* SUFFICIENT ALLOCATION FOR THE FOLLOWING TABLES
*   1. NOISE   (XXXNNN)
*   2. NOISES  (XXXNNN)
*
***
```

APPENDIX IV

INM CASE SUMMARY OF 1992 BASELINE RESULTS

(4 pages)

INM 5.2a ECHO REPORT 09-Mar-01 10:52

STUDY: U:\T24_NEW\

Created : 10-Dec-99 08:13

Units : English

Airport : EW1

Description :

NASA SET Task 24: System Studies

New INM V5.2A Study of 1992 Baseline Bizjet and Configurations 1-5

EPNL and SEL Takeoff and Approach Contours

CASE: CASEORIG

Created date: 19-Jan-00 16:15

Description : New Original 1992 Baseline Case

STUDY AIRPORT

Lat : 0.000000 deg

Long : 0.000000 deg

Elev : 0.00 ft

Temp : 59.00 F

Press : 29.92 in-Hg

Wind : 8.00 knt

STUDY RUNWAYS

09

Lat : 0.000000 deg

Long : 0.000000 deg

X : 0.0000 nmi

Y : 0.0000 nmi

Elevation: 0.0 ft

OtherEnd : 27

Length : 10000 ft

Gradient : 0.00%

Wind : 8.0 knt

TkoThrsh : 0 ft

AppThrsh : 0 ft

27

Lat : 0.000000 deg

Long : 0.027381 deg

X : 1.6458 nmi

Y : 0.0000 nmi

Elevation: 0.0 ft

OtherEnd : 09

Length : 10000 ft

Gradient : 0.00%

Wind : 8.0 knt

TkoThrsh : 0 ft

AppThrsh : 0 ft

STUDY TRACKS

RwyId-OpType-TrkId

Sub	PctSub	TrkType	Delta (ft)
-----	--------	---------	------------

09	-APP-TR2		
----	----------	--	--

0	100.00	Vectors	0.0
---	--------	---------	-----

09	-DEP-TR1		
----	----------	--	--

0	100.00	Vectors	0.0
---	--------	---------	-----

STUDY TRACK DETAIL

RwyId	OpType	TrkId	SubTrk	SegType	Param1	Param2 (nmi)
09	-APP	TR2	-0	1	Straight	10.0000 nmi
09	-DEP	TR1	-0	1	Straight	20.0000 nmi

STUDY AIRCRAFT

BIZJET User-defined

Descrip	: 1992 Technology Baseline Bizjet (Orig)
UserID	: GA
WgtCat	: Small
OwnerCat	: GenAviation
EngType	: Jet
NoiseCat	: 1
Type	: Jet
NumEng	: 1
NoiseId	: BIZBAS
ATRS	: No
TkoWgt	: 27399 lb
LndWgt	: 18887 lb
LndDist	: 3000 ft
StaticThr	: 3558 lb

STUDY SUBSTITUTION AIRCRAFT

USER-DEFINED NOISE

Type	Thrust	Crv	200	400	630	1000	2000	4000	6300	10000	16000	25000
BIZBAS ThrustType:pounds ModelType:INM												
EPNL	1190.0	N	95.3	91.0	87.8	84.0	77.7	70.7	65.4	59.2	51.1	41.2
EPNL	2166.0	N	99.6	95.4	92.2	88.6	82.7	75.9	70.8	65.0	57.5	48.2
EPNL	3558.0	N	106.1	102.0	98.9	95.5	89.7	83.1	77.3	71.7	64.7	56.2

USER-DEFINED PROFILES

OpType	Prof	Weight (lb)
BIZJET		
APP	U1	18887
DEP	U1	27398

USER-DEFINED PROFILE POINTS

	Distance (ft)	Altitude (ft)	Speed (knt)	Thrust	Curve
BIZJET-APP-U1					
1	-286217.1	15000.0	126.0	951.1 lb	N
2	-190811.4	10000.0	126.0	949.1 lb	N
3	-119916.0	6336.0	126.0	947.1 lb	N
4	-30139.0	1631.0	126.0	945.1 lb	N
5	0.0	50.0	126.0	943.1 lb	N
6	960.0	0.0	126.0	202.2 lb	N
7	1500.0	0.0	70.0	200.2 lb	N
8	3000.0	0.0	1.0	198.2 lb	N
BIZJET-DEP-U1					
1	0.0	0.0	30.0	3444.7 lb	N

2	3431.0	0.0	134.0	3270.5	lb	N
3	7754.0	200.0	164.0	3174.5	lb	N
4	14035.0	1035.0	190.0	3079.3	lb	N
5	24161.0	2396.0	212.0	2853.3	lb	N
6	45899.0	5000.0	250.0	2747.9	lb	N
7	139506.4	8000.0	250.0	2598.3	lb	N
8	219178.1	12000.0	261.0	2357.5	lb	N
9	305166.8	15000.0	275.0	2194.3	lb	N

USER-DEFINED PROCEDURES

StepType	Flap	ThrType	Param1	Param2 (knt)	Param3
----------	------	---------	--------	--------------	--------

FLIGHT OPERATIONS

AcftId	Op	Prof	Rwy	Track	Group	Day	Eve	Night
BIZJET	APP	U1	09	TR2	0 GA	1.0000	0.0000	0.0000
BIZJET	DEP	U1	09	TR1	0 GA	1.0000	0.0000	0.0000

RUNUP OPERATIONS

ID	X(nmi)	Y(nmi)	Head	Thrust	Time(sec)	Day	Eve	Night
----	--------	--------	------	--------	-----------	-----	-----	-------

USER-DEFINED METRICS

Type	Family	Day	Eve	Night	Time (dB)
------	--------	-----	-----	-------	-----------

USER-DEFINED FLAP COEFFICIENTS

Flap	Op	Coeff R	Coeff C_D	Coeff B
------	----	---------	-----------	---------

USER-DEFINED JET THRUST COEFFICIENTS

ThrType	CoeffE	Coeff F	CoeffGA	CoeffGB	CoeffH
---------	--------	---------	---------	---------	--------

USER-DEFINED PROP THRUST COEFFICIENTS

ThrType	Efficiency	Power
---------	------------	-------

GRIDS

X(nmi)	Y(nmi)	Ang(deg)	DistI(nmi)	DistJ(nmi)	NI
CNR Contour	-40.0000	-4.0000	0.0	80.0000	8.0000 2 2

RUN OPTIONS

```

Run Type      : SingleMetric
NoiseMetric   : EPNL
TA Threshold  : 85.0 dB
Do Terrain    : No
Do Contour    : Yes
Refinement    : 8
Tolerance     : 0.50
Do Population : No
Do Locations  : No
Do Stand.Grid : No
Do Detail.Grid: No
Low Cutoff    : 50.0
High Cutoff   : 110.0
Compute System Metrics:
  DNL         : No
  CNEL        : No
  LAEQ        : No

```

LAEQD : No
LAEQN : No
SEL : No
LAMAX : No
TALA : No
NEF : No
WECPNL : No
EPNL : Yes
PNLTM : No
TAPNL : No

APPENDIX V

INM CASE SUMMARY FOR NEW NOISE/ALTITUDE RESULTS

(4 pages)

INM 5.2a ECHO REPORT 09-Mar-01 11:31

STUDY: U:\T33SHRT\

Created : 10-Dec-99 08:13

Units : English

Airport : EW1

Description :

NASA SET Task 24: System Studies

New INM V5.2A Study of 1992 Baseline Bizjet and Configurations 1-5

EPNL and SEL Takeoff and Approach Contours

CASE: CASEORIG

Created date: 19-Jan-00 16:15

Description : New Original 1992 Baseline Case

STUDY AIRPORT

Lat : 0.000000 deg

Long : 0.000000 deg

Elev : 0.00 ft

Temp : 59.00 F

Press : 29.92 in-Hg

Wind : 8.00 knt

STUDY RUNWAYS

09

Lat : 0.000000 deg

Long : 0.000000 deg

X : 0.0000 nmi

Y : 0.0000 nmi

Elevation: 0.0 ft

OtherEnd : 27

Length : 10000 ft

Gradient : 0.00%

Wind : 8.0 knt

TkoThrsh : 0 ft

AppThrsh : 0 ft

27

Lat : 0.000000 deg

Long : 0.027381 deg

X : 1.6458 nmi

Y : 0.0000 nmi

Elevation: 0.0 ft

OtherEnd : 09

Length : 10000 ft

Gradient : 0.00%

Wind : 8.0 knt

TkoThrsh : 0 ft

AppThrsh : 0 ft

STUDY TRACKS

RwyId-OpType-TrkId

Sub PctSub TrkType Delta (ft)

09 -APP-TR2

0 100.00 Vectors 0.0

09 -DEP-TR1

0 100.00 Vectors 0.0

STUDY TRACK DETAIL

RwyId-OpType-TrkId-SubTrk	SegType	Param1	Param2(nmi)
09 -APP-TR2 -0	1 Straight	10.0000 nmi	
09 -DEP-TR1 -0	1 Straight	20.0000 nmi	

STUDY AIRCRAFT

BIZJET User-defined

Descrip : 1992 Technology Baseline Bizjet (Orig)
 UserID : GA
 WgtCat : Small
 OwnerCat : GenAviation
 EngType : Jet
 NoiseCat : 1
 Type : Jet
 NumEng : 1
 NoiseId : BIZBAS
 ATRS : No
 TkoWgt : 27399 lb
 LndWgt : 18887 lb
 LndDist : 3000 ft
 StaticThr : 3558 lb

STUDY SUBSTITUTION AIRCRAFT

USER-DEFINED NOISE

Type	Thrust	Crw	200	400	630	1000	2000	4000	6300	10000	16000
25000											
BIZBAS	ThrustType:pounds	ModelType:INM									
EPNL	198.0	N	92.4	88.4	85.5	82.3	76.8	70.0	64.9	58.7	50.6
40.5											
EPNL	200.0	N	90.5	86.5	83.6	80.4	74.9	68.1	63.0	56.8	48.7
38.6											
EPNL	202.0	N	90.9	86.8	84.0	80.7	75.0	68.2	63.1	56.8	48.7
38.5											
EPNL	943.0	N	94.0	89.7	86.6	82.9	76.7	69.8	64.5	58.1	50.1
39.8											
EPNL	945.0	N	94.1	89.8	86.7	83.0	76.7	69.8	64.5	58.2	50.1
40.0											
EPNL	947.0	N	94.5	90.4	87.1	83.4	77.0	70.0	64.7	58.4	50.3
40.4											
EPNL	949.0	N	95.0	90.7	87.6	83.8	77.4	70.3	65.0	58.7	50.6
40.8											
EPNL	951.0	N	95.6	91.2	87.9	84.1	77.8	70.7	65.5	59.2	51.2
41.5											
EPNL	2194.0	N	104.6	100.0	96.7	93.3	87.3	80.6	75.2	69.7	62.7
54.3											
EPNL	2358.0	N	104.0	99.4	96.7	93.1	87.2	80.3	74.8	69.2	62.2
53.6											
EPNL	2598.0	N	103.8	100.0	96.6	93.1	87.2	80.3	74.8	69.2	62.2
53.6											
EPNL	2748.0	N	103.9	100.0	96.6	92.9	87.1	80.0	74.3	68.6	61.5
52.8											
EPNL	2853.0	N	103.7	99.8	96.7	93.0	87.2	80.0	74.3	68.6	61.5
52.8											

EPNL	3079.0	N	105.0	100.5	97.1	93.6	87.9	80.9	75.0	69.3	62.2
53.5											
EPNL	3175.0	N	104.9	100.7	97.5	94.0	88.3	81.3	75.3	69.6	62.6
53.5											
EPNL	3271.0	N	105.4	101.1	97.9	94.4	88.6	81.9	75.8	70.1	63.1
54.3											
EPNL	3445.0	N	106.7	102.6	99.6	96.3	90.8	83.1	77.0	71.3	64.1
55.3											

USER-DEFINED PROFILES

OpType	Prof	Weight (lb)
BIZJET		
APP	U1	18887
DEP	U1	27398

USER-DEFINED PROFILE POINTS

	Distance (ft)	Altitude (ft)	Speed (knt)	Thrust	Curve
BIZJET-APP-U1					
1	-286217.1	15000.0	126.0	951.1 lb	N
2	-190811.4	10000.0	126.0	949.1 lb	N
3	-119916.0	6336.0	126.0	947.1 lb	N
4	-30139.0	1631.0	126.0	945.1 lb	N
5	0.0	50.0	126.0	943.1 lb	N
6	960.0	0.0	126.0	202.2 lb	N
7	1500.0	0.0	70.0	200.2 lb	N
8	3000.0	0.0	1.0	198.2 lb	N
BIZJET-DEP-U1					
1	0.0	0.0	30.0	3444.7 lb	N
2	3431.0	0.0	134.0	3270.5 lb	N
3	7754.0	200.0	164.0	3174.5 lb	N
4	14035.0	1035.0	190.0	3079.3 lb	N
5	24161.0	2396.0	212.0	2853.3 lb	N
6	45899.0	5000.0	250.0	2747.9 lb	N
7	139506.4	8000.0	250.0	2598.3 lb	N
8	219178.1	12000.0	261.0	2357.5 lb	N
9	305166.8	15000.0	275.0	2194.3 lb	N

USER-DEFINED PROCEDURES

StepType	Flap	ThrType	Param1	Param2 (knt)	Param3
----------	------	---------	--------	--------------	--------

FLIGHT OPERATIONS

AcftId	Op	Prof	Rwy	Track	Group	Day	Eve	Night
BIZJET	APP	U1	09	TR2	0 GA	1.0000	0.0000	0.0000
BIZJET	DEP	U1	09	TR1	0 GA	1.0000	0.0000	0.0000

RUNUP OPERATIONS

ID	X (nmi)	Y (nmi)	Head	Thrust	Time (sec)	Day	Eve	Night
----	---------	---------	------	--------	------------	-----	-----	-------

USER-DEFINED METRICS

Type	Family	Day	Eve	Night	Time (dB)
------	--------	-----	-----	-------	-----------

USER-DEFINED FLAP COEFFICIENTS

Flap	Op	Coeff R	Coeff C_D	Coeff B
------	----	---------	-----------	---------

USER-DEFINED JET THRUST COEFFICIENTS

ThrType	CoeffE	Coeff F	CoeffGA	CoeffGB	CoeffH
---------	--------	---------	---------	---------	--------

USER-DEFINED PROP THRUST COEFFICIENTS
ThrType Efficiency Power

GRIDS

	X(nmi)	Y(nmi)	Ang(deg)	DistI(nmi)	DistJ(nmi)	NI
NJ						
CNR Contour	-40.0000	-4.0000	0.0	80.0000	8.0000	2 2

RUN OPTIONS

Run Type : SingleMetric
NoiseMetric : EPNL
TA Threshold : 85.0 dB
Do Terrain : No
Do Contour : Yes
Refinement : 8
Tolerance : 0.50
Do Population : No
Do Locations : No
Do Stand.Grid : No
Do Detail.Grid : No
Low Cutoff : 50.0
High Cutoff : 110.0
Compute System Metrics:

DNL : No
CNEL : No
LAEQ : No
LAEQD : No
LAEQN : No
SEL : No
LAMAX : No
TALA : No
NEF : No
WECPNL : No
EPNL : Yes
PNLTM : No
TAPNL : No

REPORT DOCUMENTATION PAGE			Form Approved
Public reporting burden for this collection of information is estimated to average 1 hour per response, including the time for reviewing instructions, searching existing data sources, gathering and maintaining the data needed, and completing and reviewing the collection of information. Send comments regarding this burden estimate or any other aspect of this collection of information, including suggestions for reducing this burden, to Washington Headquarters Services, Directorate for Information Operations and Reports, 1215 Jefferson Davis Highway, Suite 1204, Arlington, VA 22202-4302, and to the Office of Management and Budget, Paperwork Reduction Project (0704-0188), Washington, DC 20503.			
1. AGENCY USE ONLY (Leave blank)	2. REPORT DATE October 2002	3. REPORT TYPE AND DATES COVERED Contractor Report	
4. TITLE AND SUBTITLE Small Engine Technology (SET) Task 33 - Final Report Airframe, Integration, and Community Noise Study		5. FUNDING NUMBERS NAS3-27483, Task 33	
6. AUTHOR(S) Lys S. Lieber and Daniel Elkins		781-20-12-01	
7. PERFORMING ORGANIZATION NAME(S) AND ADDRESS(ES) Honeywell Engines, Sysytems, and Services 111 South 34th Street Phoenix, AZ 85034		8. PERFORMING ORGANIZATION REPORT NUMBER	
9. SPONSORING/MONITORING AGENCY NAME(S) AND ADDRESS(ES) National Aeronautics and Space Administration Langley Research Center Hampton, VA 23681-2199		10. SPONSORING/MONITORING AGENCY REPORT NUMBER NASA/CR-2002-211670	
11. SUPPLEMENTARY NOTES Lieber and Elkins, Honeywell Engines and Systems NASA Technical Monitor: Robert A. Golub			
12a. DISTRIBUTION/AVAILABILITY STATEMENT Unclassified-Unlimited Subject Category 71 Distribution: Nonstandard Availability: NASA CASI (301) 621-0390		12b. DISTRIBUTION CODE	
13. ABSTRACT (Maximum 200 words) Task Order 33 had four primary objectives as follows: (1) Identify and prioritize the airframe noise reduction technologies needed to accomplish the NASA Pillar goals for business and regional aircraft. (2) Develop a model to estimate the effect of jet shear layer refraction and attenuation of internally generated source noise of a turbofan engine on the aircraft system noise. (3) Determine the effect on community noise of source noise changes of a generic turbofan engine operating from sea level to 15,000 feet. (4) Support lateral attenuation experiments conducted by NASA Langley at Wallops Island, VA, by coordinating opportunities for Contractor Aircraft to participate as a noise source during the noise measurements. Noise data and noise prediction tools, including airframe noise codes, from the NASA Advanced Subsonic Technology (AST) program were applied to assess the current status of noise reduction technologies relative to the NASA pillar goals for regional and small business jet aircraft. In addition, the noise prediction tools were applied to evaluate the effectiveness of airframe-related noise reduction concepts developed in the AST program on reducing the aircraft system noise. The AST noise data and acoustic prediction tools used in this study were furnished by NASA.			
14. SUBJECT TERMS Airframe Noise, Engine Noise, Noise reduction, Final report, Jet Shear Layer, Noise Prediction code, lateral Attenuation, Aircraft Systems Noise		15. NUMBER OF PAGES 120	
		16. PRICE CODE	
17. SECURITY CLASSIFICATION OF REPORT Unclassified	18. SECURITY CLASSIFICATION OF THIS PAGE Unclassified	19. SECURITY CLASSIFICATION OF ABSTRACT Unclassified	20. LIMITATION OF ABSTRACT UL